UC-34D
LBL-18341
c.1

Lawrence Berkeley Laboratory

UNIVERSITY OF CALIFORNIA

RECEIVED
LAWRENCE
BERKELEY LABORATORY
DEC 19 1984
LIBRARY AND
DOCUMENTS SECTION

Physics Division

A SEARCH FOR FRACTIONALLY CHARGED PARTICLES
IN e^+e^- ANNIHILATIONS

J.E. Huth
(Ph.D. Thesis)

September 1984

For Reference
Not to be taken from this room

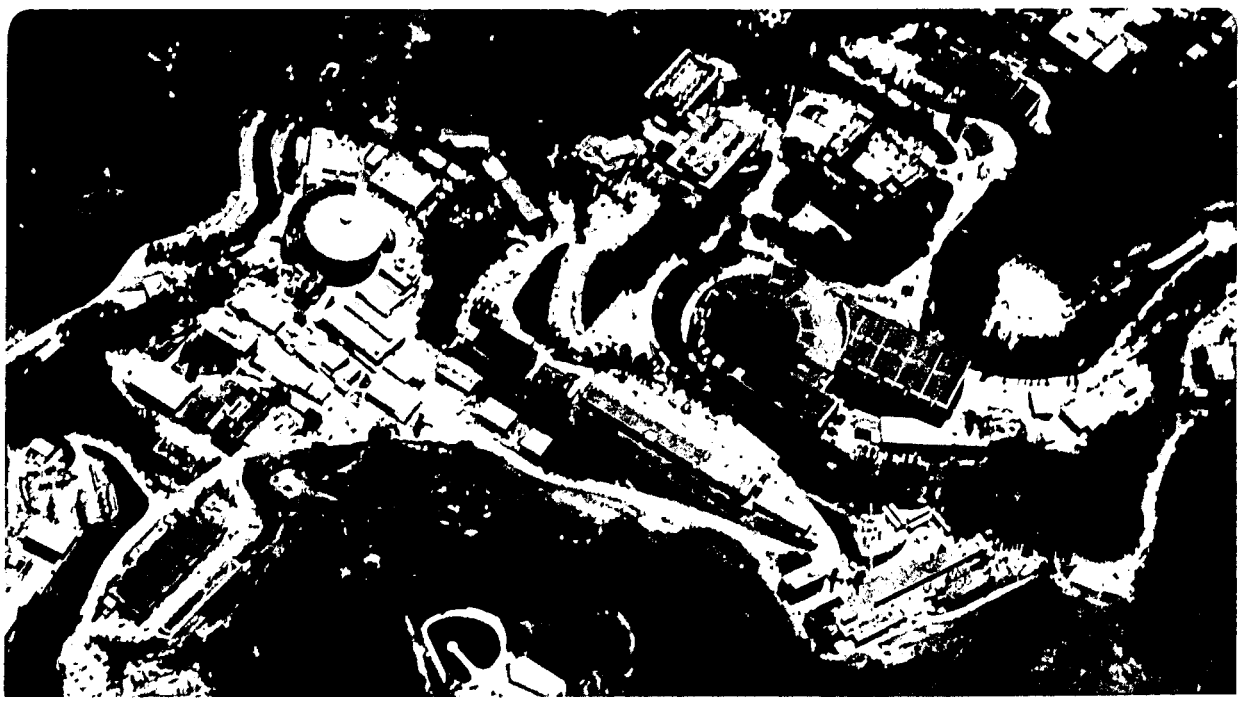

LBL-18341
c.1

Prepared for the U.S. Department of Energy under Contract DE-AC03-76SF00098

DISCLAIMER

This document was prepared as an account of work sponsored by the United States Government. While this document is believed to contain correct information, neither the United States Government nor any agency thereof, nor the Regents of the University of California, nor any of their employees, makes any warranty, express or implied, or assumes any legal responsibility for the accuracy, completeness, or usefulness of any information, apparatus, product, or process disclosed, or represents that its use would not infringe privately owned rights. Reference herein to any specific commercial product, process, or service by its trade name, trademark, manufacturer, or otherwise, does not necessarily constitute or imply its endorsement, recommendation, or favoring by the United States Government or any agency thereof, or the Regents of the University of California. The views and opinions of authors expressed herein do not necessarily state or reflect those of the United States Government or any agency thereof or the Regents of the University of California.

A Search for Fractionally Charged Particles in e^+e^- Annihilations

John Edward Huth

Ph.D. Thesis

Lawrence Berkeley Laboratory
University of California
Berkeley, CA 94720

This work was supported by the U.S. Department of Energy under Contract No. DE-ACO3-76SF00098.

A Search for Fractionally Charged Particles

in e^+e^- Annihilations

John Edward Huth

ABSTRACT

We have searched for the production of free $Q = \pm\frac{1}{3}e$, $Q = \pm\frac{2}{3}e$ and $Q = \pm\frac{4}{3}e$ particles produced in e^+e^- collisions at a center-of-mass energy of 29 GeV in 77 pb^{-1} of data collected by the time projection chamber at PEP. No evidence has been found for the production of these particles. Upper limits are established on the inclusive cross section for the production of $Q = \pm\frac{1}{3}e$, $Q = \pm\frac{2}{3}e$, and $Q = \pm\frac{4}{3}e$ particles in the mass range 1.0 $-$ 13 GeV/c^2, improving upon previously established limits.

CONTENTS

1. Introduction **1**

2. Models with free quarks and diquarks **6**

2.1. Models with free quarks 7

2.2. Models with free diquarks. 13

2.2.1. Mass splittings of diquarks 15

2.3. Production of Free Quarks 21

3. Apparatus **28**

3.1. PEP 28

3.2. The PEP-4 detector 29

3.3. The TPC 33

3.3.1. Principle of Operation 33

3.3.2. Field cages 36

3.3.3. Sectors 36

3.3.4. Electronics 39

3.3.5. Track reconstruction 43

3.4. Triggering 49

3.5. Luminosity Monitoring 53

4. Energy loss measurement in the TPC **54**

4.1. $< dE/dx >$ scaling with β and Q 56

4.2. The energy loss distribution 63

4.2.1. Practical considerations 69

5. Data analysis **76**

5.1. Overview 76

5.2. The Search regions 79

5.2.1. $< dE/dx >$ resolution 79

5.2.2. Boundaries imposed by electronics 84

5.2.3. Low Momentum Boundary 86

5.3. Multihadron Event Selection 88

5.4. Candidate selection at low dE/dx 89

5.5. Search region at high dE/dx and momenta 91

5.5.1. Pad restrictions 91

5.5.2. Wire restrictions 99

5.5.3. The remaining candidate. 108

5.6. Background Estimates 110

5.6.1. Tails of charge-1e population 110

5.6.2. Deuterons 110

5.6.3. Overlapping track pairs 113

5.6.3.1. Track pair resolution function 114

5.6.4. Summary of background studies 117

6. Results and Conclusions **119**

6.1. Efficiency Calculation 120

A. Errors in apparent momentum **130**

B. Variations in the Boundaries of the Search Regions **135**

FIGURES

Figure 2.1. A charge inside an antiscreening dielectric 9

Figure 2.2. A dipole inside an antiscreening dielectric. 11

Figure 2.3. Decay of (ud) into a pion and (uu) diquark. 21

Figure 2.4. Production in hadron-hadron collisions 23

Figure 2.5. $e^+e^- \rightarrow q\bar{q}$ to first order 23

Figure 2.6. Predictions for R_{excl} 26

Figure 3.1. Longitudinal cross section of the PEP-4 detector 30

Figure 3.2. Transverse cross section of the PEP-4 detector 31

Figure 3.3. Schematic view of the TPC 34

Figure 3.4. TPC sector 37

Figure 3.5. Sector cell geometry 38

Figure 3.6. TPC electronics chain 40

Figure 3.7. Gain curve 42

Figure 3.8. Electronics test pulser 43

Figure 3.9. Cluster finding 45

Figure 3.10. z cluster distribution 46

Figure 3.11. Pad cluster reconstruction 48

Figure 3.12. Trigger units 51

Figure 4.1. Features of the energy loss curve 55

Figure 4.2. $< dE/dx >$ curves for charge-1e particles 55

Figure 4.3. Argon photoabsorption levels 62

Figure 4.4. $< dE/dx >$ vs apparent momentum 63

Figure 4.5. Energy loss distribution in the TPC. 67

Figure 4.6. Prediction of model for $< dE/dx >$ 69

Figure 4.7. Gain shifts 73

Figure 4.8. $< dE/dx >$ for Bhabha electrons 74

Figure 4.9. $< dE/dx >$ vs momentum for data 75

Figure 5.1. Search regions 78

Figure 5.2. Distribution of wire hits 81

Figure 5.3. Gaussian fit to $< dE/dx >$ resolution 82

Figure 5.4. Two-Gaussian fit to $< dE/dx >$ resolution 82

Figure 5.5. Wire saturation values 84

Figure 5.6. Low gain cluster distributions 85

Figure 5.7. Low gain pulse height spectrum 86

Figure 5.8. Momentum error distribution 87

Figure 5.9. $< dE/dx >$ vs. $< \eta_{edge} >$ 90

Figure 5.10. Candidates after preliminary cuts 92

Figure 5.11. Overlapping track pair 93

Figure 5.12. Monte Carlo overlapping track pair 94

Figure 5.13. Distribution of close pad hits 95

Figure 5.14. Edge track 96

Figure 5.15. Pad width distribution 97

Figure 5.16. Pad width likelihood distribution 98

Figure 5.17. Likelihood distribution from detector simulation 99

Figure 5.18. Track rejected by likelihood restriction 100

Figure 5.19. Pad width vs. pad row 100

Figure 5.20. Wire cluster widths 102

Figure 5.21. Wide wire hits 102

Figure 5.22. Track rejected by wire width cut 104

Figure 5.23. Track rejected by width cut 105

Figure 5.24. $< dE/dx >$ resolution before cuts 106

Figure 5.25. $< dE/dx >$ for Bhabha electrons (with restrictions) 107

Figure 5.26. Remaining candidate 109

Figure 5.27. Wire hits on candidate 109

Figure 5.28. Secondary interactions in beam pipe 111

Figure 5.29. Impact parameter distribution 112

Figure 5.30. Deuteron candidates 112

Figure 5.31. Impact parameters for deuteron candidates 113

Figure 5.32. Angular separation of overlapping tracks 115

Figure 5.33. Shift of $\Delta\phi$ with momentum 116

Figure 5.34. $\Delta\phi$ distribution for multihadron tracks 118

Figure 6.1. $< dE/dx >$ scatter plot with free quarks 123

Figure 6.2. Upper limits for $Q = \frac{1}{3}e$ particles 126

Figure 6.3. Upper limits for $Q = \frac{2}{3}e$ particles 127

Figure 6.4. Upper limits for $Q = \frac{4}{3}e$ particles 129

Figure A.1. Momentum errors 134

TABLES

Table 2.1. SU(3) quadratic Casimir operators. 18

Table 2.2. Expectation values for color hyperfine splitting. 18

Table 2.3. SO(3) quadratic Casimir operators. 19

Table 2.4. Expectation values for glow hyperfine splitting. 20

Table 3.1. Radial dimensions of barrel part of PEP-4 detector. 32

Table 4.1. Parameters for $< dE/dx >$ curves 62

Table 5.1. Multihadron background sources 89

Table 6.1. $Q = \frac{1}{3}e$ efficiencies 124

Table 6.2. $Q = \frac{2}{3}e$ efficiencies 125

Table 6.3. $Q = \frac{2}{3}e$ efficiencies 125

ACKNOWLEDGEMENTS

This is to acknowledge not only the help I received in performing this work, but also the people who put together the experiment and kept it running. By this I mean the PEP-4 collaboration and the engineers, programmers and technicians without whose efforts there would be no data tapes to analyze. There are too many people in this category to mention by name, but they were indespendible. I feel that in doing this work I have received excellent guidance from a number of people, Peter Nemethy and Dick Kofler for advice during the data analysis, Owen Chamberlain for philosophical advice, and, of course, Jay Marx who kept me moving through this whole thing. After 20 years of school, I feel it is appropriate to acknowledge two teachers who have strongly influenced my views on both science and learning, Blaise Zuccaro, and James Nelson. Most importantly I want to thank Karen, who has been by my side from the Spring I started working on this project.

Chapter 1.

Introduction

The success of the quark-parton model has motivated many searches for free fractionally charged particles at accelerators. To date, no free quarks have been seen in these searches, leading to the widespread belief that quarks may be permanently confined inside color singlet hadrons. As will be seen in the next chapter, free quarks may be quite massive, and thus impossible to produce at low center of mass energies. Free quarks may also have form factors which lead to a production suppression in most channels. These possibilities could not only explain the null results of previous searches, but they also provide the incentive to perform searches at higher center of mass energies and with greater sensitivity.

The earliest accelerator searches were conducted in fixed target experiments. With the advent of colliding beam facilities, the available center of mass energy has increased substantially, allowing searches for heavy free quarks. In recent years, searches in colliding beams have been conducted using pp, $p\bar{p}$, and e^-e^- collisions. To date, no free quarks have been reported in any of these searches. A review of these experiments and associated production limits up to 1977 can be found in reference [1]; a review of more recent searches can be found in reference [2].

The only recent search (excepting the work presented here) not discussed in these review articles was performed by the UA2 collaboration at the CERN-SPS $p\bar{p}$ facility. Fractionally charged particles could be detected in their apparatus from low amounts of ionization deposited by tracks in a scintillator telescope array. With no candidates observed, they report an upper limit on the flux of $Q = \pm\frac{1}{3}e$ and $\pm\frac{2}{3}e$ particles with mass less than $2\,GeV/c^2$ at $\sim 10^{-3}$ that of the normal hadronic flux [3].

that a $Q = \frac{4}{3}e$ diquark may be the lightest and only stable free fractionally charged particle. These possibilities are compelling enough to continue the search for fractionally charged particles with greater sensitivity.

The work presented here is based on data collected by the PEP-4 detector at the PEP e^+e^- storage ring at SLAC. The central tracking chamber of the PEP-4 detector, the time projection chamber (TPC) is uniquely suited to a fractional charge search at high sensitivity. Charged particle species in the TPC are identified through a simultaneous measurement of track curvature in a magnetic field, and a highly accurate measurement of $< dE/dx >$. The fractional charge search was performed in regions of $< dE/dx >$ and apparent momentum (inferred from track curvature) not populated by stable charge-1e particles (K,π,μ,e,p).

The TPC, described in detail in chapter 3, samples the ionization deposited by charged particles up to 182 times over the track length. In addition, the TPC provides intrinsically three dimensional tracking information. Because of this high density of information, the TPC is able to achieve the best $< dE/dx >$ resolution (~ 3.5 %) of any detector yet constructed for storage ring experiments. This resolution allows for highly sensitive searches for fractionally charged particles with little or no contamination from the tails of the charge-1e population. The TPC also has the unique capability to observe relativistic $Q = \frac{4}{3}e$ particles. As will be discussed in chapter 5, track pairs with very small angular separations are often reconstructed as a single track. In this case, the reconstructed track will have an anomalously high $< dE/dx >$ and can mimic the characteristics of a relativistic charge-$\frac{4}{3}e$ particle. Because of the TPC's fine spatial segmentation, it is possible to reduce this background substantially. Other detectors with coarser segmentation are not sensitive to relativistic charge-$\frac{4}{3}e$ particles.

Here we will present results of a search for $Q = \pm\frac{1}{3}e, \pm\frac{2}{3}e$, and $\pm\frac{4}{3}e$ particles produced in the inclusive reaction: $e^+e^- \rightarrow QX$. No evidence was found for the production of these particles. The organization of this dissertation is as follows. First theoretical models will be discussed which allow for the production of free quarks and diquarks, along with the ramifications for e^+e^- searches. Next the PEP-4 detector system will be described, with particular attention

to the aspects of the TPC which allow for accurate $< dE/dx >$ measurement. The details of $< dE/dx >$ measurement will be examined in chapter 4, including a discussion of systematic effects which must be controlled to achieve the requisite $< dE/dx >$ resolution. In chapter 5, the data analysis is presented, along with background estimates. Finally, the details of acceptance calculations will be shown in chapter 6, followed by a presentation of the derived upper limits on R_{incl} for $Q = \pm\frac{1}{3}e$, $\pm\frac{2}{3}e$, and $\pm\frac{4}{3}e$ particles.

Chapter 2.

Models with free quarks and diquarks

In light of the null results of many free quark searches it is quite plausible that quarks are permanently confined to the interior of color singlet hadrons. It is also conceivable that somehow nature has put free quark production and detection out of the reach of these investigations. A number of theoretical possibilities are discussed in this chapter which suggest that free quarks (or diquarks) could be produced, but that because of insufficient center of mass energy or insufficient statistics, or a restriction to the charges $\frac{2}{3}$ and $\frac{1}{3}e$, these searches might not have been sensitive.

We know of the confined variety of quarks mainly from spectroscopic evidence, and through scattering experiments. As far as these experiments are concerned, quarks are the nearly massless, pointlike entities of which hadrons are composed. In contrast, according to some theoretical expectations, free quarks could be extremely massive objects with extended form factors, behaving in many ways like massive hadrons. These models are based on quantum chromodynamics (QCD) and possess one or more tunable parameters such as the gluon mass which allow for permanent confinement as a limit in which the free quark mass becomes infinite. The heavy mass would make free quark production in accelerator searches impossible at low energies. In addition, the extended form factors imply a production suppression that would make low statistics searches insensitive to their detection.

Models which consider interquark potentials [8] , [9] raise the possibility that free diquarks could be the only observable fractionally charged objects. Given certain conditions and mass splittings, it is also possible that a $Q = \frac{4}{3}e$ diquark might be the lightest and perhaps only stable fractionally charged particle. Most of the previous accelerator searches have been insensitive to

$Q = \frac{4}{3}e$ particles, and would have missed the detection of such an object.

Using QCD as a starting point, the models allowing for very massive free quarks will be discussed. This will be followed by a description of the models with free diquarks, but not free quarks, along with a consideration of the mass splittings which give rise to a free $Q = \frac{4}{3}e$ particle as the only detectable fractionally charged particle. Finally the possibility of producing free quarks in colliding beam experiments will be examined in light of these models.

2.1. Models with free quarks

At the present time, Quantum Chromodynamics (QCD) appears to be a viable theory of the strong interactions. In QCD, the interaction between quarks is mediated by 8 massless vector gluons. These correspond to the 8 generators of the gauge group $SU(3)_{color}$. The theory is modeled after QED, but possesses one important difference: the gluon field, A^μ_a, has an effective color charge associated with it, unlike the photon field, A^μ. The index a runs from 1 to 8, corresponding to the 8 gluons in the theory. The difference between the two theories is reflected in the structure of their respective field strength tensors. For the electromagnetic field, the tensor is:

$$F^{\mu\nu} = \partial^\mu A^\nu - \partial^\nu A^\mu \tag{2.1}$$

For the color field, the tensor is:

$$F^{\mu\nu}_a = \partial^\mu A^\mu_a - \partial^\nu A^\mu_a + ig \sum_{b,c} f_{abc} A^\mu_b A^\nu_c \tag{2.2}$$

where f_{abc} are the antisymmetric $SU(3)$ structure constants [10], and g determines the strength of the gluon-gluon interaction. The indices a,b, and c range from 1 to 8.

If it were not for the last term in 2.2, the behavior of QCD would be quite similar to QED. The effective coupling constant in both of these theories is a function of q^2, the momentum transfer squared. The last term in (2.2) allows for a QCD coupling constant, $g(q^2)$, which gets smaller at larger values of q^2, in contrast to QED, where the effective coupling gets larger as one goes to larger q^2. This is because at large distances the gluon field tends to antiscreen (ie. make

the effective charge larger), rather than screen color charges. At low q^2 (less than 50 GeV^2) the QCD coupling constant becomes so large that the first few terms in a perturbation expansion fail to give accurate predictions. On this size scale, one must resort to semiempirical models, such as the bag model [11] or the string model [12] to describe hadronic structure.

No one has demonstrated analytically the confinement of quarks, starting from the QCD Lagrangian. In order to gain a qualitative understanding of confinement , one must resort to computer simulations of fields on large lattices representing space-time coordinates, or to semiempirical models. I will describe below two variants of the bag model which allow for the production of very massive free quarks with absolute confinement as a limiting case. In the first variant, due to T. D. Lee [13], really an exercise in electrostatics, the QCD vacuum acts like a dielectric with a dielectric constant, ϵ, less than 1. In contrast to the properties of normal matter, the vacuum would tend to anti-screen quark color charges. It is likely that the antiscreening nature of the gluon field in QCD is responsible for this behavior. In reality the differences between electrodynamics and chromodynamics may make a strict analogy between the two impossible, nonetheless the following model illustrates some features the ultimate model of confinement may possess.

As a concete example, consider a charge $+Q$ at the center of a spherical cavity of radius R_o. This cavity is surrounded by an antiscreening medium (figure 2.1). We shall later identify a free quark with this cavity. Because it is antiscreening, the dielectric will have positive charges on the inner surface of the cavity (a normal dielectric would have negative charges). If R_o were allowed to vary it is clear that because of Coulombic repulsion $R_o = \infty$ would be stable. For a normal dielectric, $R_o = 0$ will be stable.

For an electrostatic field with a point charge at the origin, Gauss's law gives:

$$\vec{\nabla} \cdot \vec{D} = 4\pi\rho = \frac{Q\delta(r)}{r^2} \tag{2.3}$$

Here it is appropriate to use the "displacement" field, $\vec{D}$, in the presence of a dielectric (*cf.* ref [14]). Because of spherical symmetry, we need only consider the constraints on the components

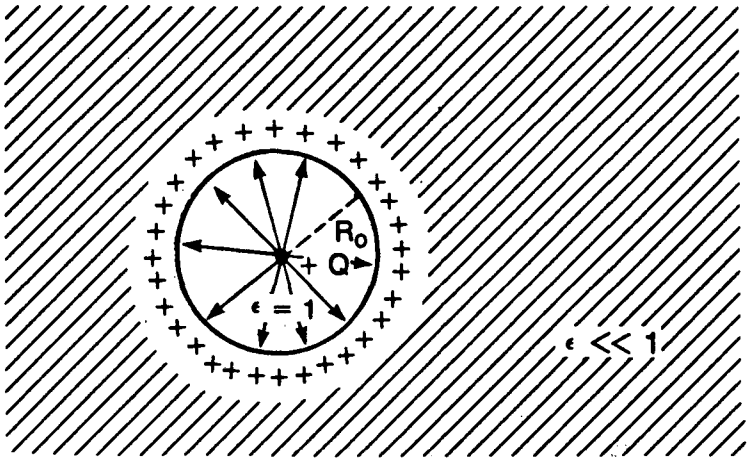

Figure 2.1: A charge at the center of a cavity of radius R_o inside an antiscreening dielectric.

of $\vec{D}$ and $\vec{E}$ normal to the surface of the cavity. $\vec{D}$ must be continuous across the boundary:

$$\vec{D}(r = R_o^+) = \vec{E}(r = R_o^-) = \epsilon \vec{E}(r = R_o^+) \tag{2.4}$$

where

R_o^+ is R_o plus an infinitesimal distance (outside the cavity)

R_o^- is R_o minus an infinitesimal distance (inside the cavity)

The fields $\vec{E}$ and $\vec{D}$ outside the cavity will then be:

$$\vec{E}(r > R_o) = \frac{Q}{\epsilon r^2} \tag{2.5}$$

$$\vec{D}(r > R_o) = \frac{Q}{r^2} \tag{2.6}$$

We are interested in finding the energy stored in the dielectric due to the charge in the cavity, and thus the effective "mass" of the cavity. The field energy in the presence of a dielectric is given by:

$$U_{cav} = \frac{1}{8\pi} \int_V \vec{E} \cdot \vec{D} dV \tag{2.7}$$

We must subtract off the contribution of the charge itself to the field energy, then

$$U_{cav} = \frac{1}{8\pi} \int_V \left(\frac{Q^2}{\epsilon r^4} - \frac{Q^2}{r^4} \right) dV \tag{2.8}$$

Evaluating the angular integral gives:

$$U_{cav} = \frac{1}{2}\int_{R_o}^{\infty} \frac{Q^2}{r^2}\left(\frac{1}{\epsilon}-1\right) dr \tag{2.9}$$

or

$$U_{cav} = \frac{Q^2}{2R_o}\left(\frac{1}{\epsilon}-1\right) \tag{2.10}$$

Here is the expected result, namely $R_o = \infty$ is a stable solution. In order to obtain a cavity (or bag) of a finite radius, an ad-hoc pressure term is introduced to the overall energy. The physical origin of this term is not speculated on here, however, it can be related to g [15]. For a pressure p which counters the tendency of the bag to expand, the total energy becomes:

$$U_{tot} = \frac{Q^2}{2R_o}\left(\frac{1}{\epsilon}-1\right) + \frac{4\pi}{3}R_o^3 p \tag{2.11}$$

In units where $\frac{h}{2\pi} = c = 1$, p has units of fm^{-4}. The condition for minimization of U_{tot} with respect to R_o is that

$$\frac{\partial U_{tot}}{\partial R_o} = 0 = \frac{-Q^2}{2R_o^2}\left(\frac{1}{\epsilon}-1\right) + 4\pi R_o^2 p \tag{2.12}$$

or

$$R_o = \left(\frac{Q^2}{8\pi p}\left(\frac{1}{\epsilon}-1\right)\right)^{\frac{1}{4}} \tag{2.13}$$

In the limit that $\epsilon \ll 1$ we have

$$R_o \approx \left(\frac{Q^2}{8\pi\epsilon p}\right)^{\frac{1}{4}} \tag{2.14}$$

and the mass of the cavity is:

$$M = U_{tot} \approx \frac{4}{3}\left(\frac{\pi p Q^6}{2\epsilon^3}\right)^{\frac{1}{4}} \tag{2.15}$$

Note that the mass of the cavity becomes infinite as the dielectric becomes perfectly antiscreening (ie. as $\epsilon \rightarrow 0$). This cavity can be associated with a free color state.

Rather than a single charge, one could consider a dipole at the center of a hollow cavity (figure 2.2). In this case, we don't have spherical symmetry and must consider the effect of the dielectric on all components of the field. The tangential component of $\vec{E}$ must be continuous across the surface of the cavity:

$$\vec{E}_{tan}(r = R_o^-) = \vec{E}_{tan}(r = R_o^+) \tag{2.16}$$

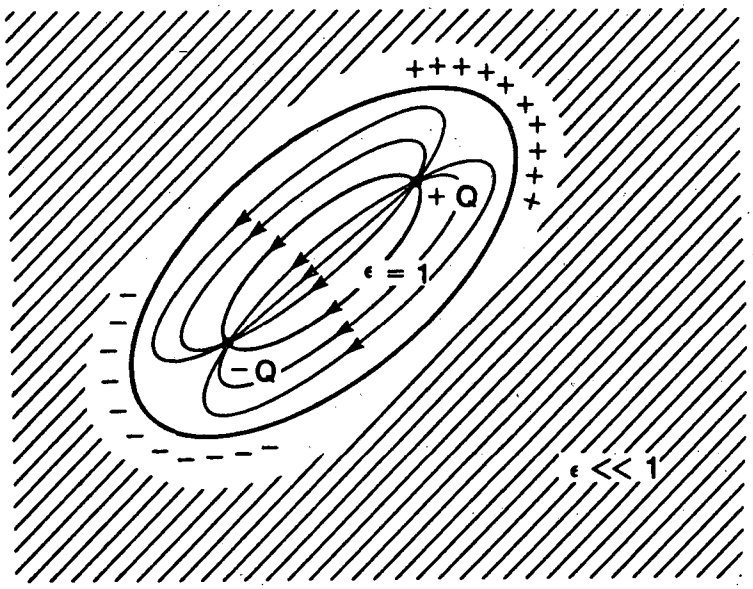

Figure 2.2: A dipole in a cavity surrounded by an antiscreening dielectric.

For a unit vector, $\hat{n}$, normal to the surface of the cavity, we have:

$$\hat{n} \cdot \vec{D}(r = R_o^+) = \hat{n} \cdot \vec{E}(r = R_o^-) = \epsilon \hat{n} \cdot \vec{E}(r = R_o^+) \tag{2.17}$$

(*cf.* equation (2.4)).

Let us now suppose that the hypothetical dielectric is a perfect antiscreening medium, that is, ϵ is exactly zero. In this case the normal component of $\vec{E}$ at the surface of the cavity must vanish by the above condition. Only the tangential component of the field $\vec{E}$ is non-zero. When this occurs, the field lines from the dipole must be contained within the cavity and thus $\vec{D}$ vanishes outside the cavity. This is illustrated in figure 2.2. Since $\vec{D}$ vanishes outside, the field energy remains finite. This is to be contrasted with the monopole case in which the mass of the cavity system becomes infinite as $\epsilon \to 0$.

This is qualitatively how confinement is thought to arise. Because of the antiscreening nature of the gluon field at large distances, the QCD vacuum acts like a perfect (or nearly perfect) antiscreening dielectric. Mesons, which are essentially color dipoles, have a finite mass, but a free quark has a large mass which becomes infinite in the limit that $\epsilon \to 0$. The condition in which ϵ is small but non-zero is one form of what is termed quasiconfinement, because quarks appear confined at low center of mass energies.

In the argument above, we have assumed that the QCD vacuum acts like an antiscreening dielectric. If one really accepts this kind of model, one must account for the fact that the dielectric constant is a property of the vacuum and not the result of the bulk properties of a collection of dipoles in matter. Since we must have a Lorentz invariant vacuum, c must be a constant (1 in these units). This constrains the magnetic permeability, μ, of the vacuum, since $(\mu\epsilon)^{-\frac{1}{2}} = 1$. This implies that as $\epsilon \rightarrow 0$, the color "magnetic" permeability of the vacuum approaches infinity.

Clearly the color dielectric constant ϵ doesn't have to be exactly 0 to agree with the current status of quark searches. Lee [15] has shown the limits as of 1979 on the mass of free quarks imply a constraint on ϵ in equation (2.15):

$$\epsilon < 0.013 \left(\frac{g^2}{4\pi}\right) \tag{2.18}$$

where g is the strong coupling constant measured on a length scale of 1 fm; here g subsumes the constants p and Q in equation (2.15). If ϵ is small, but non-zero, free quarks can exist, but they must possess a much greater mass than ordinary mesons and baryons.

One drawback of Lee's model is that the dielectric constant, ϵ, is a macroscopic property. In many ways it would be preferable to formulate a model of confinement in terms of microscopic quantities, such as masses and charges. DeRújula, Giles and Jaffe [16] have developed a variant of the bag model with some similarities to T. D. Lee's model, but with the advantage that the the gluon mass plays the role of the adjustable parameter ϵ. All eight gluons are given an equivalent mass.

In the DeRújula, Giles and Jaffe (DGJ) model, no field lines can leave the bag. This is essentially the $\epsilon = 0$ limit of Lee's model. The role of the gluon mass is to make the interquark potential fall to zero at large distances. In the limit of zero gluon mass quarks will be absolutely confined. For a non-zero gluon mass, μ, the color equivalent of Gauss's equation is:

$$\nabla^2 \phi_a - \mu^2 \phi_a = 4\pi \rho_a(x) \tag{2.19}$$

where a is the color index. In order to find the free quark mass and radius, one can go through a derivation very similar to the one above. As with Lee's model, the energy of the bag will be a

minimum for an infinite radius, only in this case the energy scales as R_o^{-3} rather than R_o^{-1}. A stable solution with a finite volume can be found if a pressure is introduced as in equation (2.11). By adding a term of the form pV to the bag energy and minimizing with respect to V, a finite radius solution can be found. DeRújula *et al* obtain a scaling law for the mass of free quarks in terms of the gluon mass.

$$M_Q = \frac{0.18(GeV^2)}{\mu} \tag{2.20}$$

To give one a feel for the relationship between the gluon and free quark masses in this model, one can use equation (2.20) to show that a 10 GeV free quark will result if the gluon mass is 18 MeV. Note that permanent confinement will result if one takes the gluon mass to be exactly zero.

In the limit that the free quark mass becomes infinite, one finds that confined particles would have a non-zero flux integral over the surface of a volume containing them, whereas free states, like mesons, baryons, and glueballs, have no net flux piercing this surface. In electrodynamics we would say that the free particles are neutral. In chromodynamics, we say that these free states are color singlets (ie $SU(3)_{color}$ transformations leave these unchanged).

In addition to the prediction that free quarks will be very massive, both of the above models have the common feature that free quarks possess radii larger than common hadrons (*cf* equation 2.14). DeRújula Giles and Jaffee estimate that a 10 GeV free quark would have a radius $\approx 3\ fm$ [16]. The large size of free quarks implies that they have form factors similar to hadrons, but with even more long wavelength components. The large size of free quarks also implies that they have substantial nuclear cross section. DGJ estimate a nuclear cross section for free quarks that scales as

$$\frac{\sigma_{Qp}}{\sigma_{pp}} \approx \frac{1}{4}\left(1+\left(\frac{M_Q}{M_p}\right)^{\frac{1}{3}}\right)^2 \tag{2.21}$$

where M_p and M_Q are the proton and free quark mass respectively.

2.2. Models with free diquarks.

In the DGJ model all eight gluons are given an equal mass leading to the possibility that any

colored representations (ie non-singlets) can exist as free asymptotic states. Slansky, Goldman and Shaw (SGS) [9] have proposed a model in which the $SU(3)_{color}$ symmetry is broken in such a way that color triplets are permanently confined, but some higher order representations (eg. a color 6) can exist as free asymptotic states. In this model, what was an exact $SU(3)_{color}$ symmetry is broken to an $SO(3)$ symmetry termed glow. Three gluons, corresponding to the generators of $SO(3)_{glow}$ are left massless, while the remaining 5 gluons acquire a non-zero mass.

The effect of this symmetry breaking is to allow unconfined glow singlets which are not color singlets. In particular, diquarks, which have an $SO(3)$ singlet representation, can be free states in this model, but single quarks cannot be free states. The action of the $SU(3)$ generators can be represented by 8 traceless 3 by 3 unitary matrices acting on the 3 dimensional vectors consisting of triplets in color space. The three color dimensions (or charges) are labeled as red, green and blue (r, g, and b). A convenient representation of the $SU(3)$ generators are the Gell-Mann matrices, $F_a = \frac{1}{2}\lambda_a$. The λ_a's are given by:

$$\lambda_1 = \begin{pmatrix} 0 & 1 & 0 \\ 1 & 0 & 0 \\ 0 & 0 & 0 \end{pmatrix} \quad , \quad \lambda_2 = \begin{pmatrix} 0 & -i & 0 \\ i & 0 & 0 \\ 0 & 0 & 0 \end{pmatrix}$$

$$\lambda_3 = \begin{pmatrix} 1 & 0 & 0 \\ 0 & -1 & 0 \\ 0 & 0 & 0 \end{pmatrix} \quad \lambda_4 = \begin{pmatrix} 0 & 0 & 1 \\ 0 & 0 & 0 \\ 1 & 0 & 0 \end{pmatrix}$$

$$\lambda_5 = \begin{pmatrix} 0 & 0 & -i \\ 0 & 0 & 0 \\ i & 0 & 0 \end{pmatrix} \quad \lambda_6 = \begin{pmatrix} 0 & 0 & 0 \\ 0 & 0 & 1 \\ 0 & 1 & 0 \end{pmatrix}$$

$$\lambda_7 = \begin{pmatrix} 0 & 0 & 0 \\ 0 & 0 & -i \\ 0 & i & 0 \end{pmatrix} \quad \lambda_8 = \frac{1}{\sqrt{3}} \begin{pmatrix} 1 & 0 & 0 \\ 0 & 1 & 0 \\ 0 & 0 & -2 \end{pmatrix}$$

If one includes $F_0 = \frac{1}{\sqrt{6}}I$ (I is the identity), the above group is $U(3)$. $SO(3)$ is a subalgebra of $SU(3)$, and has the generators F_2,F_5, and F_7. In three color dimensions they represent the possible glow transformations. A triplet under $SU(3)$ is also a triplet under $SO(3)$. Since single quarks form a color triplet, they will not exist as free particles in the SGS scheme. Diquarks, however, do have an $SO(3)$ singlet representation. Under $SU(3)$ the possible representations of diquarks come from the rule

$$3 \otimes 3 = 3^* \oplus 6 \tag{2.22}$$

The 3^* of color comes from the antisymmetric color combinations:

$$\frac{rg - gr}{\sqrt{2}}$$
$$\frac{rb - br}{\sqrt{2}}$$
$$\frac{gb - bg}{\sqrt{2}}$$

Under $SO(3)$ this representation remains a triplet. The symmetric 6, given by:

$$\frac{rg + gr}{\sqrt{2}} \qquad rr$$
$$\frac{rb + br}{\sqrt{2}} \qquad gg$$
$$\frac{bg + gb}{\sqrt{2}} \qquad bb$$

does have one $SO(3)$ singlet representation. Under the $SU(3)_{color} \rightarrow SO(3)_{glow}$ symmetry breaking the color 6 is broken into a glow 5 and a glow 1. The member of the color 6 with a glow singlet representation is:

$$\frac{(rr + gg + bb)}{\sqrt{3}} \tag{2.23}$$

Glow can be considered an effective $SO(3)$ charge in much the same way color is considered and effective $SU(3)$ charge. The glow singlet possesses no net glow. Because of this, in the SGS model, the glow singlets will not experience an effective potential due to the exchange of the 3 gluons represented by the subgroup $SO(3)$. The glow singlets will, however, experience the effect of the remaining 5 massive gluons. Since these have a finite mass , the potential generated by their exchange will only extend over a finite distance. The glow singlets will exist as heavy states, but can be liberated with a sufficient center of mass energy. States like quarks, with no glow singlet representation, will feel the effective potential generated by the exchange of the 3 massless gluons and will not exist as free states.

2.2.1. Mass splittings of diquarks

The above scheme allows for free diquarks, but not free quarks. What these arguments do not address are the physical properties of free diquarks, such as strangeness, charge, mass splittings,

isospin etc. As will be shown there are certain forms of the mass splittings, in particular the color hyperfine splitting, which will give rise to a $Q = \frac{4}{3}e$ diquark as the lightest and perhaps only stable fractionally charged object. If free diquarks are produced at PEP energies (29 GeV in the center of mass), it is unlikely that they will contain b or c quarks, because these quarks are so massive. Accordingly, I will consider here only the effects of $SU(3)_{flavor}$. $SU(2)$ spin will also be considered.

The representations of diquarks under $SU(3)_{flavor}$ are the same as for $SU(3)_{color}$, only here the indices stand for quark flavors. The possible representations are:

$$(3 \otimes 3)_{flavor} = (6 \oplus 3^*)_{flavor} \tag{2.24}$$

The 6 is the set of symmetric combinations of u,d and s, given by

$$\frac{ud + du}{\sqrt{2}} \qquad uu$$

$$\frac{us + su}{\sqrt{2}} \qquad dd$$

$$\frac{ds + sd}{\sqrt{2}} \qquad ss$$

The 3^* is the set of antisymmetric combinations of u,d and s given by

$$\frac{ud - du}{\sqrt{2}}$$

$$\frac{us - su}{\sqrt{2}}$$

$$\frac{ds - sd}{\sqrt{2}}$$

The $SU(3)_{flavor}$ symmetry is broken by two effects. Since the strange quark is more massive then the up and down quarks, the mass of diquarks will vary according to their strangeness. The splitting of baryon masses within individual multiplets is such that each unit of strangeness implies a mass increase of order 140 MeV. A phenomenological interaction of the form

$$H_{int} = \frac{\delta m}{3}(F_0 - F_8)_{flavor} \tag{2.25}$$

with $\delta m \approx 140\ MeV$ describes this splitting well. This implies that the (ss) diquark will be about 300 MeV heavier than the (uu) diquark. The diquark isospin multiplets are also split by

the electromagnetic interaction due to the different charges of the quarks. This splitting seems to arise because the effective mass of the d quark is ≈ 5 MeV heavier than the u quark. In addition to this, the Coulomb force between the quarks will cause like charged quarks to be more loosely bound than unlike charge quarks. It is difficult to find an effective interaction Hamiltonian which will describe this splitting well for both mesons and baryons. If the electromagnetic splitting of baryons are taken as a reference, one might expect that the (uu) diquark would be ≈ 10 MeV lighter than the (du) diquark. Since our knowledge of these splittings is very poor, in reality the electromagnetic splittings may be much larger, or even have a different sign.

Under $SU(2)_{spin}$, the allowed combinations for diquarks are the triplet and the singlet:

$$(2 \otimes 2)_{spin} = (3 \oplus 1)_{spin} \tag{2.26}$$

The triplet represents the symmetric spin 1 states, the singlet is the antisymmetric spin 0 state. These states will be split by the color hyperfine interaction. In baryon systems, this splitting is on the order of 300 MeV. In the color hyperfine interaction, one must take into account the fact that there are 3 color charges and not one as in electromagnetism. One plausible form of this interaction has been suggested by Lipkin [17]:

$$H_{QCD} = -\Delta \sum_{i \neq j} \sum_{\sigma} \frac{F_{i,\sigma} F_{j,\sigma}}{m_i m_j} S_i \cdot S_j \tag{2.27}$$

where $F_{i,\sigma}$ and $F_{j,\sigma}$ are the $SU(3)_{color}$ color generators (σ is the color index) acting on the ith and jth particles respectively. Δ is a positive constant with units of $(energy)^3$. This form of the color hyperfine interaction has the advantage that it predicts both the sign and relative magnitude of the spin-spin splitting in the low lying baryon and meson multiplets. The expectation value of $< \sum_{i \neq j} \sum_{\sigma} F_{i,\sigma} F_{j,\sigma} >$ can be found easily for a two particle system from the quadratic Casimir (invariant) operators for $SU(3)$:

$$< 2 \sum_{\sigma=1}^{8} F_{1,\sigma} F_{2,\sigma} >= (F_{tot}^2 - F_1^2 - F_2^2) \tag{2.28}$$

Here the F^2 Casimir operators are defined to be:

$$F^2 \equiv \sum_{\sigma=1}^{8} F_{\sigma}^2 \tag{2.29}$$

Representation	F^2
1	0
3	$\frac{4}{3}$
3^*	$\frac{4}{3}$
6	$\frac{10}{3}$
8	3
10	6

Table 2.1: SU(3) quadratic Casimir operators.

Color	Spin	$< H_{color} >$
3^*	0	$-\frac{1}{2}$
3^*	1	$+\frac{1}{6}$
6	0	$+\frac{1}{4}$
6	1	$-\frac{1}{12}$

Table 2.2: Expectation values for color hyperfine splitting.

Table 2.1 gives a listing of the values of the $SU(3)$ quadratic Casimir operators for some representations.

For the allowed color states of a diquark, (3^* and 6), the values of $< \sum_{\sigma=1}^{8} F_{1,\sigma} F_{2,\sigma} >$ are:

$$3^* \quad : \quad < F_3 F_3 > = \frac{1}{2}(F_{3^*} - 2F_3^2) = -\frac{2}{3}$$

$$6 \quad : \quad < F_3 F_3 > = \frac{1}{2}(F_6^2 - 2F_3^2) = \frac{1}{3}$$

Here $< F_3 F_3 >$ is a shorthand notation for $< \sum_{\sigma=1}^{8} F_{1,\sigma} F_{1,\sigma} >$ acting on two triplet representations. Evidently the splitting will have a different sign for the different color states of the diquarks. The treatment of the expectation value of $< S_1 \cdot S_2 >$ for a two particle state can be handled in the same way as in electromagnetic hyperfine interactions

$$< S_1 \cdot S_2 > = \frac{1}{2}(S_{tot}(S_{tot}+1) - S_1(S_1+1) - S_2(S_2+1)) = \frac{1}{2}(S_{tot}(S_{tot}+1) - \frac{3}{2})$$

This results in a factor of $-\frac{3}{4}$ and $\frac{1}{4}$ of $< S_1 \cdot S_2 >$ for the $SU(2)_{spin}$ singlet and triplet respectively. If we combine all the factors together, one obtains the expectation values for the hyperfine splitting shown in table 2.2.

As one can see the situation is complicated by the color factor. The spin singlet is the lighter state for the 3^*, but the spin triplet is the lighter state for the 6. From fits of $\frac{\Delta}{m_1 m_2}$ to the

Representation	F^2
1	0
3	2
5	6

Table 2.3: SO(3) quadratic Casimir operators.

splitting of the $\Delta - N$ baryon resonances, using H_{QCD} above, a value of 300 MeV for $\frac{\Delta}{m_1 m_2}$ has been found. If the above assumptions are true, then the spin 0 diquark from the color 6 will be ≈ 100 MeV heavier than the spin 1 diquark. All the above arguments are premised on a guessed form of the hyperfine splitting, assuming an exact $SU(3)_{color}$ symmetry.

If, on the other hand, the $SO(3)_{glow}$ splitting dominates over the $SU(3)_{color}$ splitting, then the situation will be quite different. Both the magnitudes and signs of the splittings will change. For the representations of interest, the $SO(3)$ F^2 Casimir operators are shown in table 2.3. If one assumes a spin-spin term for $SO(3)_{glow}$ similar to (2.27), then:

$$H_{glow} = -\Delta \sum_{i \neq j} \sum_{\sigma=2,5,7} \frac{F_{i,\sigma} F_{j,\sigma}}{m_i m_j} S_i \cdot S_j \tag{2.30}$$

then the possible spin-spin splittings can be found in a manner similar to the way they were found for $SU(3)$ above. The expectation values of $2 < \sum_{\sigma=2,5,7} F_{1,\sigma} F_{2,\sigma} >$ are:

$$1 \quad : \quad < F_3 F_3 > = \frac{1}{2}(F_1^2 - 2F_3^2) = -2$$

$$3 \quad : \quad < F_3 F_3 > = \frac{1}{2}(F_3^2 - 2F_3^2) = -1$$

$$5 \quad : \quad < F_3 F_3 > = \frac{1}{2}(F_5^2 - 2F_3^2) = +1$$

The $< S_1 \cdot S_2 >$ expectation values are the same as those for the $SU(3)_{color}$ case, the singlet state has an expectation value of $-\frac{3}{4}$ and the triplet has $\frac{1}{4}$. Table 2.4 shows the relative values for $< H_{glow} >$ defined above. In this case, the spin 0 of the glow 1 has a lower mass than the spin 1 bound state with the same glow representation. Recall that the glow 1 comes from the color 6. The sign of the spin-spin coupling evidently depends on which symmetry dominates the effective hyperfine interaction. One can go through similar arguments for the splittings due to spin-orbit coupling [8], but there are similar results, namely that one cannot a priori decide on even the sign of the splitting. These arguments will not be presented here.

Glow	Spin	$< H_{glow} >$
1	0	$-\frac{3}{2}$
1	1	$+\frac{1}{2}$
3	0	$-\frac{3}{4}$
3	1	$+\frac{1}{8}$
5	0	$+\frac{3}{4}$
5	1	$-\frac{1}{4}$

Table 2.4: Expectation values for glow hyperfine splitting.

We must now combine the representations of diquarks under the different symmetries, bearing in mind that eventually Fermi statistics must be satisfied by requiring the total wave function to be antisymmetric with respect to the interchange of particle indices. $O(3)$ of orbital angular momentum will not be considered here.

When one considers spin and flavor simultaneously, $SU(6)_{flavor+spin}$ one gets an antisymmetric 15 and a symmetric 21.

$$6 \otimes 6 = 15^* \oplus 21$$

The 15 is the symmetric flavor 6 combined with the antisymmetric spin triplet and the antisymmetric flavor 3^* combined with the symmetric spin triplet. The 21 is the combination of the flavor 6 and spin 3 with the flavor 3^* and spin singlet. Under the notation $(rep_{flavor}, rep_{spin})$, the breakdown is:

$$(15^*)_{flavor+spin} = (6,1) \oplus (3^*,3) \tag{2.31}$$

$$(21)_{flavor+spin} = (6,3) \oplus (3^*,1) \tag{2.32}$$

Since quarks are spin $\frac{1}{2}$ particles, the overall wave function must be antisymmetric. In order to satisfy the exclusion principle, the $15_{flavor+spin}$ must go with the symmetric color 6 and the $21_{flavor+spin}$ gets the antisymmetric color 3^*. Under the notation $((rep)_{flavor+spin}, (rep)_{color})$ the allowed antisymmetric representations are $(15^*,6)$ and $(21,3^*)$. The symmetric representations, $(15^*,3^*)$ and $(21,6)$, are discarded as unphysical. In the SGS scheme, the $(15^*,6)$ will have a glow singlet representation. The 15^* consists of the $(6,1^*)$ and the $(3^*,3)$ of $(flavor, spin)$. Consider the following situation. Suppose the $SO(3)$ hyperfine splitting dominates over the $SU(3)$ hyperfine splitting. In this case the $(6,1^*)$ would be lighter than the $(3^*,3)$. Within the

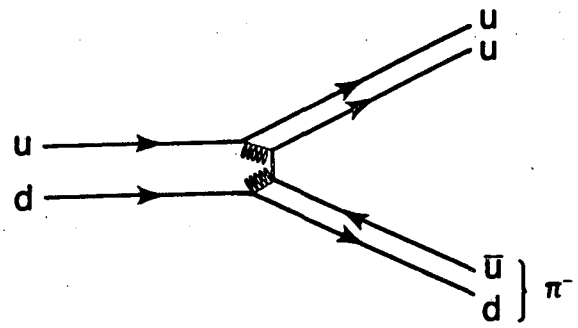

Figure 2.3: Decay of (ud) into a pion and (uu) diquark.

6, because of the $SU(3)_{flavor}$ splitting, the three diquarks (dd), $\frac{(ud+du)}{\sqrt{2}}$, and (uu) will be the lightest members. Of these three members, it is possible that the (uu) diquark will be the lightest and perhaps only stable diquark. If, for example, the (ud) diquark is more than 1 pion mass heavier than the (uu) diquark, then it might decay to the (uu) combination via the emission of a pion in a process similar to that shown in figure 2.3. Given this set of circumstances, the only stable free fractionally charged object would have $Q = \frac{4}{3}e$. One can go through similar plausibility arguments involving the orbital angular momentum, $O(3)$, and an $L \cdot S$ coupling to show that the $Q = \frac{4}{3}e$ combination may be the lightest and only stable free fractionally charged objects [8].

2.3. Production of Free Quarks

The success of the quark parton model has spawned many accelerator searches for fractionally charged particles (for a review, see reference [2]). To date, no free quarks have been have been detected in these searches, allowing one to set limits, albeit model dependent, on their mass. Every time an increase in the available center of mass energy occurs, with the construction of new accelerators, new searches are conducted. Presently, because of the large center of mass energies available, colliding beam facilities are being used for quark searches. Three main channels can be used to search for the production of free quarks at these energies, pp, $p\bar{p}$, and e^+e^- interactions. Soon searches with ep colliding beams may be possible, although this will not be considered here.

Although $p\bar{p}$ collisions start with quarks and gluons in the initial state, the bulk of the interactions are peripheral and tend to have low momentum transfer to the final state. In these collisions the three high p_t processes which may produce free quarks are the s and t channel exchanges, and gluon fusion mechanisms, shown in figure 2.4. The s channel process proceeds via a $q\bar{q}$ annihilation through a virtual photon or gluon into a final state which can have hadrons, and possibly free quarks. The t channel exchange involves a hard scatter of two quarks mediated by a gluon or photon exchange. Gluon-gluon fusion occurs when two gluons from the sea combine to produce a $q\bar{q}$ pair. In all of these processes, the particles in the initial state are either valence quarks or quarks and gluons from the sea. One major problem with the understanding of these mechanisms is that one lacks detailed knowledge of the initial state . The interpretation of a null result is difficult because the momenta of quarks and gluons in the proton are smeared out. Not only should one have some knowledge of how free quarks may be produced , but one must also understand both the momentum distributions of the valence and sea quarks and the contribution of higher order QCD effects.

e^+e^- annihilations at the current energies have an advantage over hadron-hadron collisions in that one is starting with a point-like initial state. In order to determine a momentum transfer to the finial state, one does not have to integrate over a large spectrum of constituent momenta as one must in hadron-hadron processes. The annihilation proceeds to first order in a QED process shown in figure 2.5 through an intermediate virtual photon state. The photon has a calculable coupling, and, to first order, a known momentum transfer to the elementary constituents of the final state. Initial state radiation will smear out the photon energy, but this can be calculated.

Two reactions with free quarks (or diquark) in the final state will be considered here, the exclusive channel,

$$e^+e^- \rightarrow \gamma^* \rightarrow Q\bar{Q}$$

and the inclusive channel,

$$e^+e^- \rightarrow \gamma^* \rightarrow QX$$

where Q stands for a free quark (or diquark) and X means hadrons. Since free quarks and

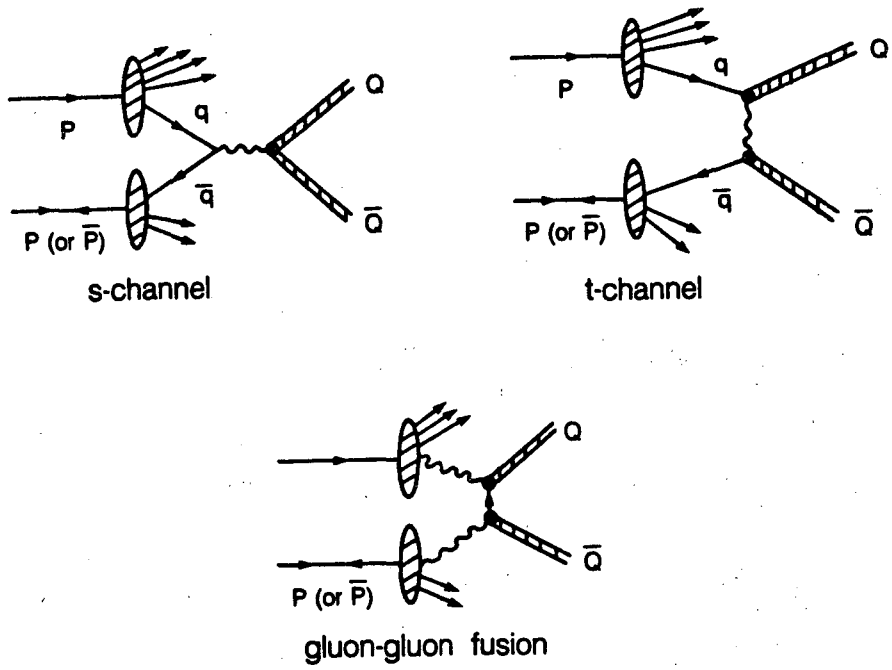

Figure 2.4: Productions mechanisms for free quarks in hadron hadron collisions. Possible channels are the s and t channel exchanges and gluon-gluon fusion.

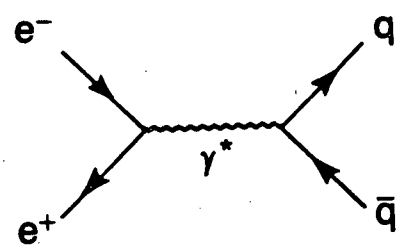

Figure 2.5: First order QED process for the reaction $e^+e^- \rightarrow q\bar{q}$.

diquarks in some ways resemble hadrons, one can use our knowledge of hadronic final states in e^+e^- annihilations as a guide to the production of these particles. As a starting point, consider the first order cross section for the production of a fermion-antifermion pair, $f\overline{f}$:

$$\sigma(e^+e^- \to \gamma^* \to f\overline{f}) = \frac{4\pi Q_f^2}{3q^2}\left(1+\frac{M_f^2}{q^2}\right)\sqrt{1-\frac{4M_f}{q^2}} \tag{2.33}$$

where Q_f is the charge, and M_f is the mass of the fermion. $\sqrt{q^2}$ is the momentum transfer to the final state ($\sqrt{q^2}$ is the center of mass energy). Because the dimuon ($\mu^+\mu^-$) final state is pointlike, it is convenient to use the process $e^+e^- \to \mu^+\mu^-$ as a reference. At the current PEP energy, 29 GeV in the center of mass, the dimuon cross section is .103 nb. If free quarks were point-like entities, then one might expect an exclusive production rate at about the same order of magnitude as the dimuon rate. Experiments sensitive to exclusively produced free quarks report lower limits on $\sigma(e^+e^- \to Q\overline{Q})$ at $\sim 10^{-2}$ that of the dimuon cross section. It is convenient to define the ratios R_{excl}, and R_{incl} as

$$R_{excl} \equiv \frac{\sigma(e^+e^- \to Q\overline{Q})}{\sigma(e^+e^- \to \mu^+\mu^-)} \tag{2.34}$$

and

$$R_{incl} \equiv \frac{\sigma(e^+e^- \to QX)}{\sigma(e^+e^- \to \mu^+\mu^-)} \tag{2.35}$$

This ratio is often cited because it factors out the $1/q^2$ dependence from the photon propagator.

As seen in this section, there are good theoretical grounds to believe that quarks are extended objects, like hadrons. When one considers the exclusive production of extended objects, such as hadron pairs or free quarks, one must include the effects of form factor suppression, which can reduce the cross section to a level way below the point-like cross section. If one knows the quark form factor as a function of the spacelike momentum transfer squared, $F(q^2)$, then according to D újula, Giles and Jaffe, one can approximate R_{excl} similar to the way one computes exclusive hadronic final states: as the product of the point-like R_{excl} for a $Q\overline{Q}$ pair and the form factor squared [16]:

$$R_{excl} \approx \frac{\sigma(e^+e^- \to Q\overline{Q})_{point-like}\,(F(q^2))^2}{\sigma(e^+e^- \to \mu^+\mu^-)} \tag{2.36}$$

DeRújula *et al* take an educated guess for $F(q^2)$ based on hadronic form factors. For R_{excl} they obtain:

$$R_{excl} \approx Q^2 \frac{\sqrt{1-\frac{4M_Q^2}{q^2}}}{\left(1+\frac{q^2R_Q^2}{10}\right)^{2p}} \tag{2.37}$$

where q is the timelike momentum transfer, Q is the charge, M_Q is the mass and R_Q is the radius of the free quark or diquark. p is a parameter which reflects whether the form factor is of the monopole or dipole form and can take the values 1 or 2; the relevance of this will be discussed shortly.

The denominator of (2.37) comes from the expected free quark form factor, and is nearly identical to what one expects for hadronic form factors. One could, in fact, substitute typical hadron masses and radii into (2.37) and obtain a reasonable approximation to R_{excl} for the exclusive hadronic (hh) final state. Equation (2.37) implies a very low cross section for $e^+e^- \rightarrow hh$, with $R_{excl} \sim 10^{-3}$ to 10^{-4} expected at PEP energies. For practical purposes (backgrounds, statistics) this is almost beyond measurability. At lower energies, 1 *GeV* CMS for example, one expects R_{excl} to be much larger; the two pion final state can be seen at these energies, but at a very low rate [18].

Qualitatively, the form factor suppression occurs because in exclusive production, phase coherence must be maintained over a distance scale comparable to the radius of the produced object. This becomes very improbable at high energies. The product q^2R^2 in the denominator of (2.37) is the embodiment of this statement, with $1/\sqrt{q^2}$ being the typical distances probed and R being the typical hadron (or free quark) radius; one is, in effect taking the ratio of two length scales. Distances probed at PEP are about two orders of magnitude smaller than typical hadronic dimensions, so it is not surprising that the process $e^+e^- \rightarrow hh$ is not observed at these energies. One can apply the same arguments to the exclusive production of free quarks. As seen earlier, one expects that very massive quarks possess radii even larger than hadrons, this would imply that R_{excl} for free quarks will be suppressed even more than for hadrons. Figure 2.6 shows DGJ's predictions for R_{excl}. It is apparent that it may be exceeding difficult to produce and detect free quarks or diquarks in the exclusive channel at these energies.

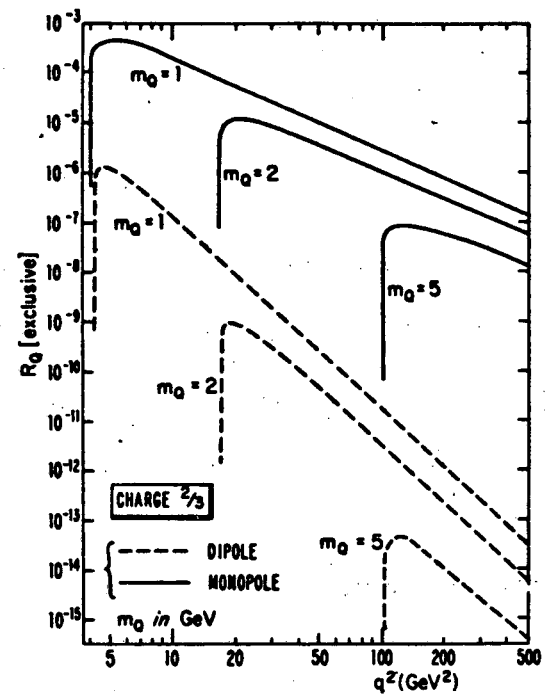

Figure 2.6: The predictions of DeRújula, *et al.* for R_{excl} (defined in the text).

The situation is not so dire in the inclusive channel. The energy scale, Λ, over which hadronization occurs is comparable to the inverse hadronic size ($\sim$ 500 MeV). As a quark antiquark pair separate, no hadrons form until the separation reaches $\approx 1/\Lambda$. At this energy scale hadron production is relatively copious, with color forces tending to rearrange the system into color singlets. One expects that inclusively produced free quarks will be produced at the same energy scale, accordingly, one can substitute $\sqrt{q^2} = \Lambda$ in the denominator (form factor) of (2.37) to get a rough estimate of R_{incl} for free quarks and diquarks. Since the free quark size increases with increasing mass, its form factor will still give suppression to the inclusive production rate relative to hadrons. Typical values expected for free quark masses and radii imply that the ratio R_{incl} will be on the order of a few 10^{-2} to 10^{-3} or smaller [16],[19].

Since diquarks are composite objects, one expects even additional form factor suppression [9]. The choice of a dipole form factor (p=2) is appropriate for baryons (p=1 is appropriate for mesons) because qualitatively, one must first form diquarks before forming baryons, and the

probability of getting 2 quarks into the same "bag" goes something the square of the probability of getting one quark into the "bag". The suppression probably carries over to free diquarks for the same reason. All these estimates are, of course, very speculative, but they point out the need for high statistics searches searches in order to constrain these models.

Chapter 3.

Apparatus

The fractional charge search was performed with data collected at the SLAC-LBL positron electron project (PEP, described below) by the PEP-4 detector facility. The time projection chamber (TPC), the central tracking chamber of the PEP-4 detector system is uniquely suited to perform a fractional charge search because of its ability to identify particles through a simultaneous measurement of energy loss and momentum. The needs of both a high statistics search for fractionally charged particles and relativistic hadron identification put extreme requirements on the design of the detector. In particular, many samples (~ 200) of track ionization must be taken, with a pulse height determination accurate to 1 %.

3.1. PEP

PEP is an electron positron storage ring 2200 m in circumference, located at the Stanford Linear Accelerator Center. It was built to extend the study of e^+e^- interactions to energies ~ 30 GeV in the center of mass, and has 6 interaction regions available for experiments. So far, experimental running has been limited to one center of mass energy, 29 GeV. During the data acquisition, the machine ran with 3 e^+ and 3 e^- bunches in the ring, with the positrons circulating counterclockwise when viewed from above. In this mode, the collision rate is 400 kHz at any interaction region. The detector run-in took place during the Spring 1982 cycle of PEP. The data used in this dissertation were collected during the Fall-Spring 82-83 running cycle. Peak total current in the ring averaged 20 mA per beam. Peak luminosities during this cycle were typically $2-4 \times 10^{31}$ $cm^{-2}sec^{-1}$ with $\approx 200-400$ nb^{-1} of integrated luminosity collected

daily. The beam profile has a vertical width of 50 μm, and a horizontal width of 500 μm. The energy spread of the beam was $\sigma_E = 200\ MeV$. Over the course of the running cycle, 77 pb^{-1} of integrated luminosity were collected, consisting of 29,094 multihadron events (selection criteria described in chapter 5).

3.2. The PEP-4 detector

The PEP-4 detector operated at interaction region 2 at PEP; this is approximately northeast of the center of the ring. The overall structure of the detector is similar to most e^+e^- colliding beam detectors, consisting of concentric layers of cylindrical detector subsystems, with the beam pipe forming the central axis. Figures 3.1 and 3.2 show a longitudinal and a transverse cross section of the detector, refer to table I for dimensions and thicknesses of the detector elements. Radially outward from the beam pipe, one encounters an aluminum inner pressure wall followed by an inner drift chamber (IDC). The TPC surrounds the IDC and has a radius of 100 cm and a length of 200 cm. An axial magnetic field is established by a solenoidal magnet coil surrounding the TPC. Outside the magnet coil is the outer drift chamber (ODC), followed by an electromagnetic calorimeter, consisting of 6 azimuthal modules forming a hexagon; this is refered to as the HEX calorimeter. Outside of the HEX calorimeter is an iron flux return yoke and hadron absorber, this is followed by four muon chambers, alternating with iron hadron absorber. The muon system also consists of six azimuthal sections, forming a hexagon. On the end caps of the detector system are a pair of electromagnetic calorimeters, magnet pole faces and a low angle muon tagging system The time projection chamber will described in detail in the next section.

The IDC operated in an 8.5 atm mixture of 80 % Ar - 20% CH_4, and consisted of four radial layers with 60 sense wires per layer. An intrinsic position resolution of 150 μm in the bending plane was obtained from cosmic ray tests [20]. The ODC operated in an 1 atm mixture of 80 % Ar and 20 % CH_4, and consisted of three radial layers with 216 sense wires in each layer. The ODC has an intrinsic position resolution of $\sim 200\ \mu m$ in the bending plane, as determined from cosmic ray tests [20]. Position information from the drift chambers was not used in track fitting,

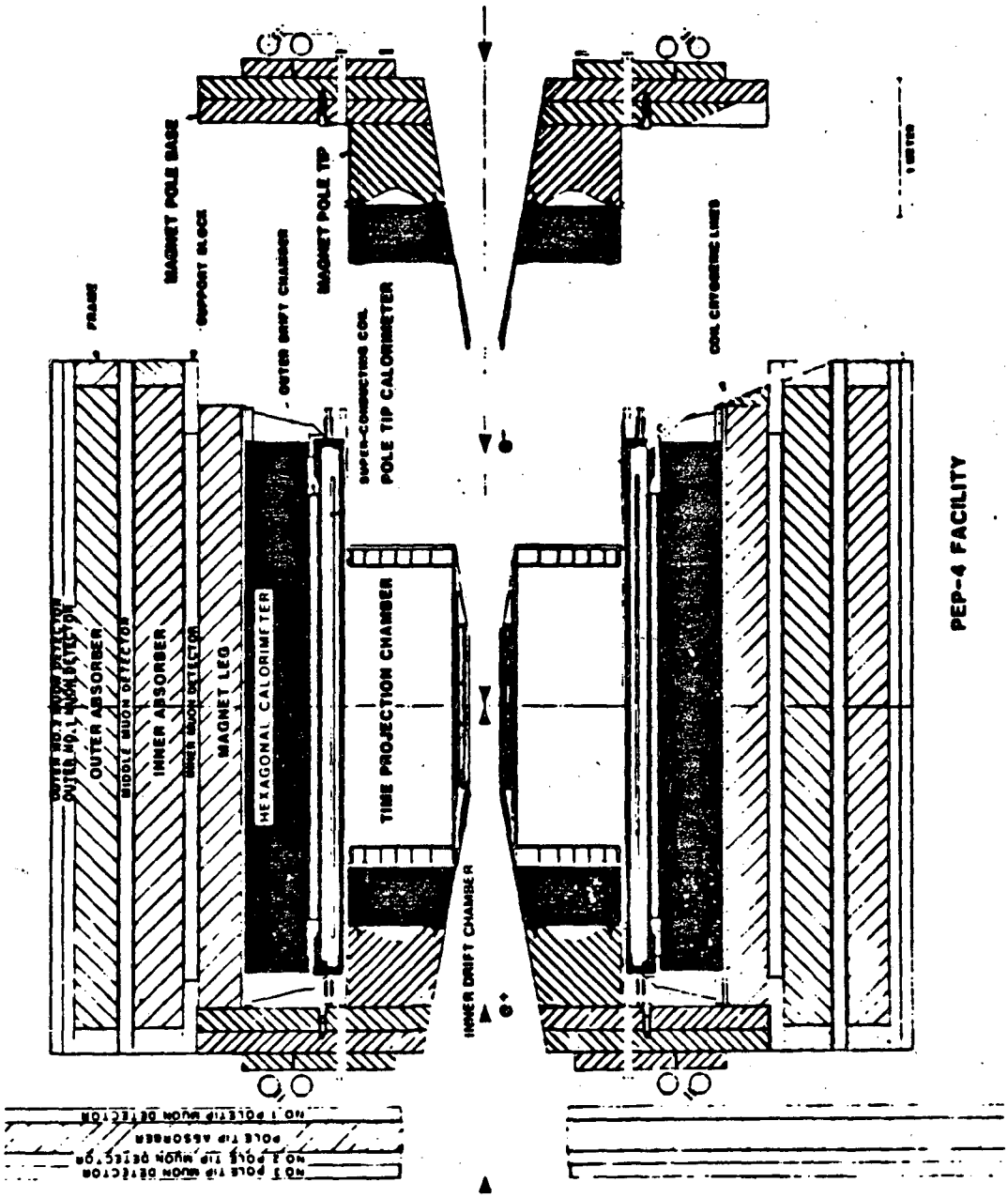

Figure 3.1: Longitudinal cross section of the PEP-4 detector.

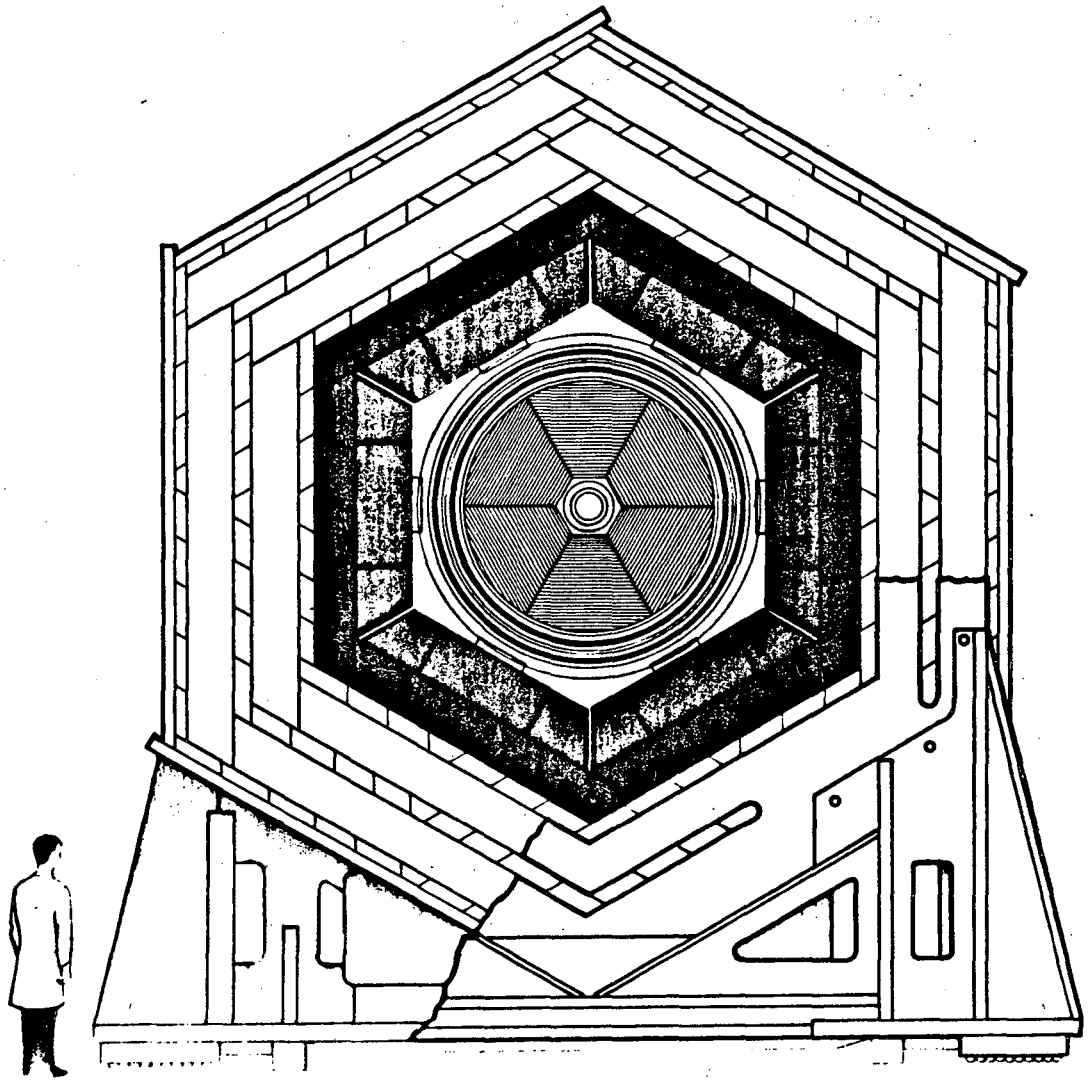

Figure 3.2: Transverse cross section of the PEP-4 detector.

Item	Outer Radius (cm)	% Rad. Length	Material
Beam pipe	8.7	2.6	Al
Pressure wall	11.5	7.1	Al
IDC	19.0	2.3	G-10,Cu,Ar,CH_4
Field cage	22.3	7.5	G-10,mylar,kapton
TPC	97.5	4.9	Ar,CH_4
Field cage	100.0	10.1	G-10,mylar,kapton
Magnet	117.0	130.0	Al,epoxy
ODC	122.0	6.5	G-10,Cu,Ar,CH_4
HEX	180.0	1370.0	Pb,Al,Ar
Muon system	320.0	8000.0	Fe,Al,Ar,Ch_4

Table 3.1: Radial dimensions of barrel part of PEP-4 detector.

although information from the chambers were used to help identify photon conversion pairs. The drift chambers were used primarily for fast trigger definition because it takes ≤ 500 $nsec$ for the drift of electrons to the wires. In contrast, it takes ~ 20 μsec for track ionization to drift the full length of the TPC.

The magnet was a conventional water cooled solenoid, consisting of four layers of Al conductor with 115 turns per layer. The conductor was wound on a 1 in thick Al spool which also supported the TPC and provided a pressure wall. At the design current, 2200 Amp, the field strength was 3.9 kG [21]. Several Hall probes were used during data acquisition to monitor the strength of the magnetic field.

Each HEX calorimeter module consisted of 40 planes of 3 mm thick Pb-Al laminate (13.7 radiation lengths), alternated with sense wire planes. The position of electromagnetic showers are determined in the HEX with a projective geometry formed by cathode strips oriented at $\pm 60^o$ angles with respect to the sense wires. The sense wires operated in Geiger mode, with each sense wire in the center of a cell 5×10 mm^2 in cross section, in 1 atm of Ar, with 3 % C_2H_5Br as a quenching agent. The energy resolution of the HEX calorimeter is 17 $\%/\sqrt{E}$ (E in GeV), and an angular resolution of $6-10$ $mrad$ [22]. Because of chemical reactions involving aluminum and bromine, 2 of the 6 modules stopped operating in the middle of the 1983 running cycle.

The pole tip calorimeters (PTC's) consisted of 51 layers of alternating wire planes and Pb-Al laminate. The PTC, like the HEX determined shower location using a projective geometry, and

three 60° views. It operated in an 8.5 *atm* mixture of 80 % Ar and 20 % CH_4 in proportional mode. The PTC has an energy resolution of $17\%/\sqrt{E}$ (E in GeV), and an angular resolution of ~ 4 *mrad*. Luminosity, derived on a run by run basis, was found from the Bhabha scattering rate into the PTC's. Taken together, the two PTC and six HEX modules cover 3.5π *strad* of solid angle.

The muon chambers cover 98 % of solid angle, and consist of 3284 triangular extruded aluminum drift cells. One plane of muon chambers consists of these cells stacked in a zig-zag pattern to optimize the spatial coverage. The first three radial muon chamber layers have the sense wires oriented parallel to the beam line, while the last layer is oriented perpendicular. The chambers operated in an 80 % Ar 20 % CH_4 gas mixture at a pressure of 1 *atm*, and provided a position resolution of 700 μm [23]. In order to penetrate to the outermost layer of the muon chambers, a track must pass through at least 90 *cm* of iron, corresponding to a pion punch-through probability of ≤ 1 % at 3 GeV/c.

3.3. The TPC

3.3.1. Principle of Operation

The time projection chamber (TPC, figure 3.3) is a highly segmented 3 dimensional imaging drift chamber . Ionization deposited in the TPC by charged particles drift up to 1 meter in an axial electric electric field parallel to the magnetic field to arrays of proportional wires called sectors (for a review, see references [24] and [25]). The TPC is 2 *m* long with an inner and outer radius of 20 *cm* and 100 *cm* respectively. Under nominal operating conditions, the TPC is filled with an 8.5 *atm* mixture of 80 % Ar and 20 % CH_4.

The drift field (75 kV/m) is established by a screen of woven tungsten wires bisecting the TPC held at negative high voltage, and a field cage, consisting of a series of equipotential rings on the inner and outer walls of the TPC, terminating at the sector shielding grids, which are held at ground potential. At the TPC operating voltage, with the gas mixture used, the drift velocity is ≈ 5 $cm/\mu sec$. Track ionization deposited on either side of this membrane will drift

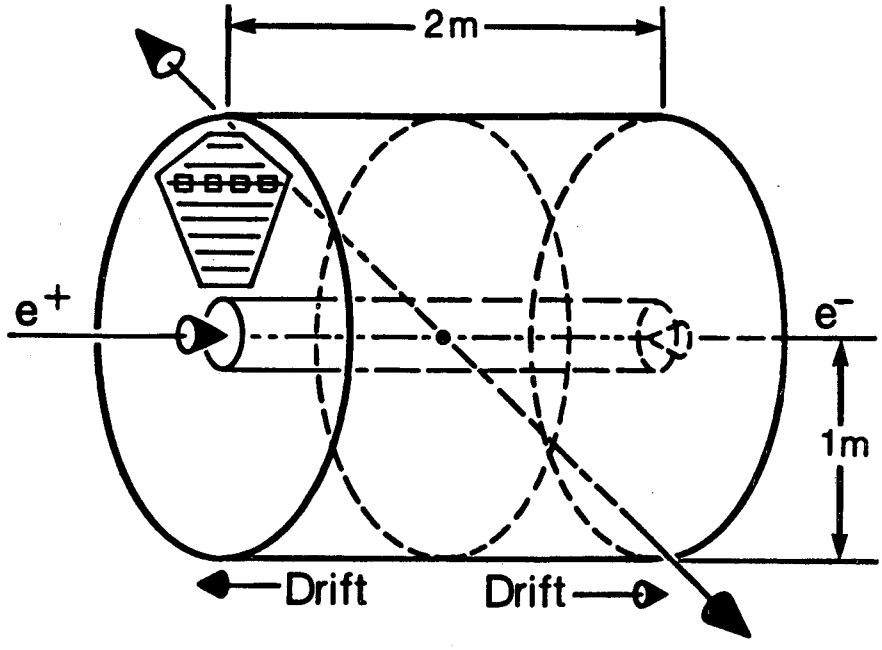

Figure 3.3: Schematic view of the TPC. Track ionization formed in the active volume drifts to the endcaps where they are detected by arrays of proportional wires called sectors (one shown, 6 per endcap). Coordinates perpendicular to the drift direction are found from rows of cathode pads etched into the sector ground plane (one of 15 rows shown).

to sectors on opposite end caps. The sectors (6 per endcap), consist of 183 proportional wires strung perpendicular to the radial line bisecting each sector above a conducting ground plane. Parallel to the sense wires are 15 rows of cathode pads pads etched into the ground plane. Track coordinates perpendicular to the drift field (x, y) are determined from the image charge of the proportional signals induced on the cathode pads. The coordinate parallel to the drift field, z, is inferred from the arrival time of the track ionization at the sectors relative to a common start time, defined by the beam-beam crossing.

The TPC was designed to identify charged particles in multihadron events by making a simultaneous measurement of momentum and of energy loss per unit length $< dE/dx >$. The $< dE/dx >$ measurement is derived from many samples of track ionization, as measured by the proportional wires on the sectors. As will be seen in the next chapter the ability to separate relativistic hadrons using $< dE/dx >$, and the ability to perform a high statistics search for fractionally charged quarks and diquarks place similar requirements on the detector specifications. In both cases, one needs to measure the energy loss of a charged particle to an accuracy of $\sim 3 - 4$ %. Operating at high pressure improves the $< dE/dx >$ resolution by increasing the number of atomic collisions per unit distance, and thus reducing the dispersion of the energy loss distribution. The requirements of $< dE/dx >$ resolution also dictate that many (~ 200) samples of track ionization be taken. With these specifications, the intrinsic resolution of an ideal detector is ≈ 2 %; systematic errors in the track ionization measurements made in the TPC must be at or below the 1 % level. This requirement puts severe constraints in particular on the design of the sectors and the signal processing electronics.

The operation of the TPC as a tracking chamber is possible because the transverse diffusion of ionization electrons is limited, allowing reasonable spatial resolution even after long drift lengths [26]. On average, a typical charge-$1e$ track will deposit ~ 150 ionization electrons per 4 mm sample length. The transverse distribution of this electron cluster arriving at the sense wires after drifting one meter will be a Gaussian with a width of 1.4 mm. If one could measure the position of each electron to an arbitrary accuracy, then one could reconstruct the position of the track to an accuracy of $1.4/\sqrt{150} \approx 100\ \mu m$ in the transverse plane. By imaging the profile

of the ionization cluster on several (two or three) pads, the TPC can achieve a resolution on the order of 180 μm in this plane.

3.3.2. Field cages

The field cages at both the inner and outer radius of the TPC each consist of two layers of equipotential rings and resistor chains; these are designated as the coarse and fine field cages. The coarse field cage rings are spaced 20 mm apart, consisting of 5 mm wide conductor on a kapton insulating surface and are connected by high precision resistors. The fine field cage rings are spaced 5 mm apart and consist of 0.5 mm wide conductor on a Nema-G10 surface connected by high precision resistors.

During the initial running of the TPC, distortions of the drift field were discovered, in which the effective potential differed from the design values by several kilovolts. One of the causes of the distortions was the electrostatic charging of the G-10 between conducting rings. Because of these distortions, the path followed by track ionization drifting to the sectors were deflected from the path that would have been taken in a uniform field. When charged particle tracks were reconstructed assuming a uniform drift field, they appeared to have kinks in regions close to the field cages. The distortions were such that 4 cm radially into the active volume, the path taken by drifting electrons was distorted by as much as ~ 1 cm from the path they would take in a perfectly uniform field. A partial cure for this problem was developed, and involved placing 4 mm wide copper conducting strips on top of the strips on the fine field cage, this reduced the size of the distortions by a factor of 10 [27].

3.3.3. Sectors

The TPC sectors (figure 3.4) are kite shaped, and consist of 183 proportional wires strung 4 mm above a ground plane of copper plated on an insulated G-10 backing. Parallel to the sense wires, spaced ~ 5 cm apart are 15 rows of 7.5×7.5 mm^2 cathode pads etched into the copper ground plane. Preamplifiers for the pads and wires are located behind the cathode plane, in a G-10 housing. The spacing of the cathode pads was constrained by the need to sample a track

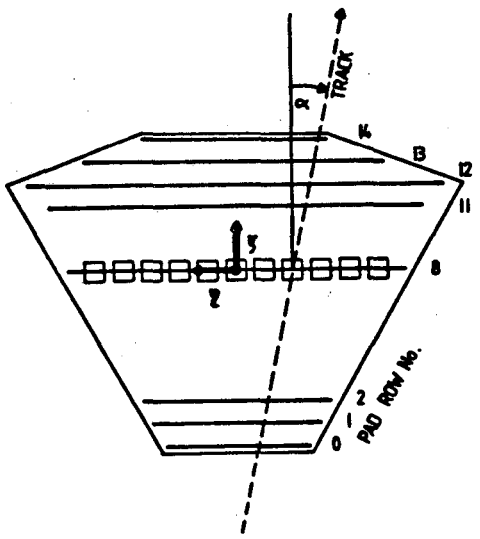

Figure 3.4: One TPC sector. 183 proportional wires are strung above a conducting plane. Track coordinates perpendicular to the drift direction are found on rows of cathode pads etched into the conducting plane. This coordinate is designated the η coordinate, with $\eta = 0$ taken at the center of the sector.

ionization cluster with at least two pads, at 10 to 15 points along a track length, and by the number of electronic channels that could be fit into any sector [28].

Figure 3.5 shows the the sector cell geometry. A plane of wires spaced 1 mm apart is suspended 8 mm above the cathode plane; this is held at ground potential and acts as a shielding grid. The sense wire plane is 4 mm above the cathode plane, and consists of 75 μm diameter gold coated Be-Cu field shaping wires alternating with 20 μm diameter gold coated tungsten sense wires. Sense and field shaping wires were spaced 2 mm apart . The wires were strung under a tension of 55 gm, 250 gm, and $\sim$ 500 gm for the sense, field and grid wires respectively. Under 55 gm of tension, the sense wires have a gravitational sag of, at most 10 μm [29]. Wire cross talk was $\sim$ 5 % between neighboring channels. In order to obtain sufficiently uniform wire response ($\sim$ 1 %) , the sense wire planes had to be be flat to within 20 μm and had to be located parallel to each other and to the cathode plane with a similar accuracy [29]. The field wires had to be positioned to an accuracy of $\sim 100 \mu m$.

Under normal operating conditions, the sense wires were held at 3405 V, and the field shaping wires were held at -700 V. With the above voltages and the TPC gas mixture, the

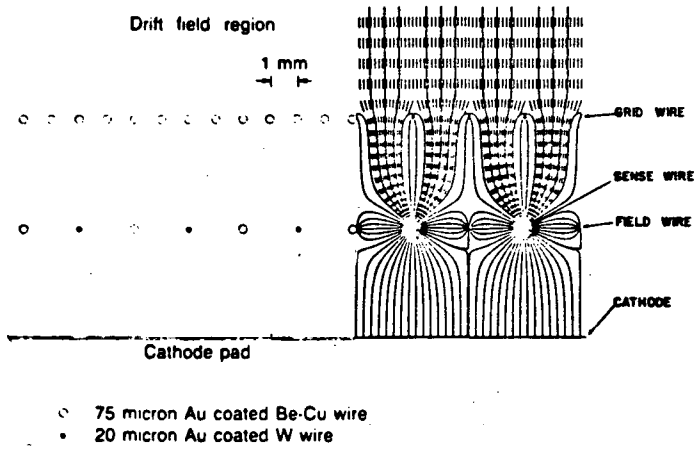

Figure 3.5: Sector cell geometry. Signals are detected on the sense wires, spaced 4 mm apart. Field shaping wires are spaced between the sense wires. A shielding grid located 8 mm above the ground plane defines the end of the drift field.

sense wire gain is typically 10^3. Studies [30] show that the maximum stable gain the sectors can reach is approximately 10^4 at 10 atm. The sectors were run at low gain both to reduce electrostatic distortions from the migration of positive ions back into the TPC active volume, and to keep the proportional signal linear in the number of ionization electrons arriving at the sense wires (discussed in more detail in the next chapter).

In order to measure a relatively small proportional signal with better than 1 % accuracy, special low noise preamplifiers were developed, which were placed directly behind the cathode plane in order to minimize signal attenuation from long cable runs and noise. Each preamplifier had a power dissipation of $\sim$ 100 mW, and with approximately 1300 preamplifiers distributed non-uniformly in any sector, large temperature gradients can develop across the cathode plane and over the length of the wires, which can strongly affect wire response. In order to ensure uniform response, a water cooling system is built into the sectors which maintains the temperature across the cathode plane constant to $1/3^o$ C [30].

To calibrate the wire response, three movable rods with Fe^{55} sources were located behind the cathode plane at the middle and edges of the sectors. When the rods were actuated, the Fe^{55}

sources "shine" through holes in the cathode planes, allowing photoionization electrons to reach the sense wires. From the Fe^{55} spectra, gain shifts were monitored periodically over the course of the running cycles .

3.3.4. Electronics

The requirement of making an accurate measurement (to 1 %) of small proportional signals necessitated the development of special low noise electronics. Figure 3.6 shows a block diagram of the signal processing chain. The induced signals on the wires and pads are capacitively coupled to preamps on the sectors. The output of the preamps are fed via coaxial cables to an electronics enclosure where they provide input to shaping amplifiers. The signals from the shaping amplifiers are clocked into charge coupled devices (CCD's), which were employed as linear analog shift registers. If a trigger is defined by fast signals from either the wire shaping amplifiers, or from other detectors, the CCD clock frequency is reduced to 20 kHz and the information is digitized and read into a data buffer. This buffer was subsequently read out by a VAX 11/780 computer during data acquisition A PDP 11/70 computer was used to control and calibrate the electronics. At several points in the analog part of the signal processing chain, it was possible to inject test pulses of varying amplitudes in order to test and calibrate components.

The sense and pad signals were capacitively coupled out to the preamplifiers located behind the cathode plane. These preamplifiers [31] have a rise time ≤ 50 $nsec$, and an input noise level equivalent to ~ 500 electrons RMS at the input (a typical signal was 10^5 electrons). Not only did the preamplifiers have to be small, inexpensive and interchangable, but they also had to be free of ferromagnetic materials, and components that could poison the TPC gas with electronegative impurities. The output signals from the preamplifiers were fed along twisted pair to a high pressure feedthrough, and then along coaxial cable to the electronics enclosure.

The proportional signals seen at the sense wires characteristically have a short rise time (~ 100 $nsec$), followed by a long tail lasting a few microseconds, resulting from the slow migration of positive ions away from the sense wire. In order to avoid track pile-up, a negative feedback loop is used in the shaping amplifiers to produce a relatively symmetric ("pseudo-Gaussian")

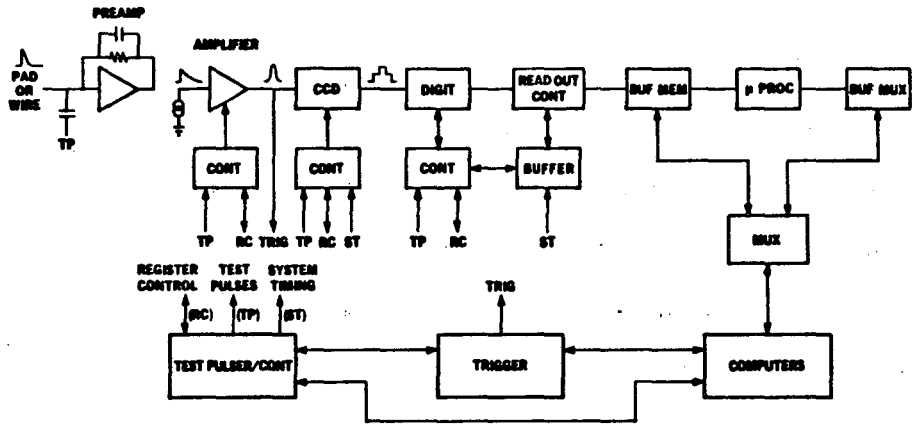

Figure 3.6: The TPC signal processing chain. Signals capacitively coupled to a preamplifier go through a shaping amplifier, are held in a CCD if a trigger decision is made, then digitized, and stored in a buffer, which is read out by a VAX 11/780. Test pulses could be injected at various places in the chain.

pulse with a peaking time of ~ 250 $nsec$. The wire shaping amplifiers have a voltage gain of 160, and the pad shaping amplifiers have a voltage gain of 230 [31]. The outputs of the wire shaping amplifiers were also connected to discriminators. The output of these discriminators were connected to trigger electronics.

Fairchild 321A CCD's were employed as sample and hold devices; these had a dynamic range of ~ 4 V [32]. In order to obtain good resolution in the drift coordinate, and in order to measure the amount of ionization deposited accurately, the wire pulses had to be sampled at a rate of 10 MHz; this means that a typical signal will be sampled 5 to 7 times. Since it takes ≈ 20 μsec for track ionization to drift over the entire length of the TPC, the full readout occupies about 200 registers (or buckets) of the CCD's, which have a maximum capacity of 455 buckets. The CCD contents were clocked to the digitizers at a rate of 20 kHz. Two characteristics of the CCD's made them difficult to calibrate. The CCD response as a function of input voltage (see figure 3.7) can be non-linear, with typically a long shoulder near saturation, these non-linearities varied substantially from chip to chip. In order to obtain the requisite 1 % accuracy in response, a relatively sophisticated fit to the CCD response was needed to take into account these non-linearities [33], [34]. Because of dark current, the baseline voltage of late buckets will be offset by as much as 2 %. Fortunately, this shift is linear in bucket number, and can be corrected for by subtracting an appropriate offset which is determined in calibration. In order to measure noise, and to aid in calibration of the electronics, a positive bias voltage, refered to as pedestal, is added to the CCD output, this is typically $300 - 400$ mV.

The digitizers have a 9 bit range; this allows for an arbitrary scale of pulse heights ranging from 0 to 511. A minimum ionizing track will generate a pulse height which is on average 100 counts above the pedestal level. Because of the enormous amount of information held in the CCD's, a readout threshold can be set on the digitizers in random access memories (RAM's). A CCD voltage level will be read out of the digitizer only if that level is above the preset level in the RAM. The noise level (4 counts RMS at the digitizer inputs) determined where the RAM thresholds were set . The RAM thresholds were set about 10 counts above the nominal pedestal level, this makes the minimum possible ionization signal that could be detected at the wires

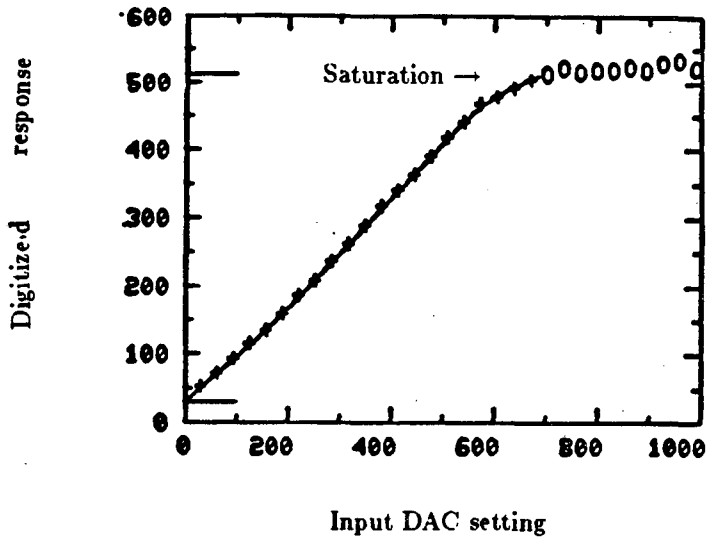

Figure 3.7: Typical response of a single channel to test pulses of varying amplitudes. The horizontal scale is the input DAC setting, the vertical scale is the digitized response. The curve is the result of a cubic splines fit. The shoulder near saturation is the result of non-linearities in the CCD chips.

approximately one tenth the ionization produced by a minimum ionizing charge-1e track. The upper limit of the digitizer range, and the saturation value of the CCD's both determine the largest amount of ionization that can be detected, this corresponds to $\sim$ 5 times the ionization deposited by a minimum ionizing charge-1e track.

At the end of each CCD output clock cycle, the digitized data higher than the RAM thresholds are multiplexed out to a set of buffers. Channels are read out in groups called lists. One wire list consists of 192 channels, one pad list consists of between 768 and 1024 channels. The information from one channel for one bucket cycle is stored on a 32 bit data word containing the digitized pulse height, the channel address, the CCD bucket number, and parity information. A typical event will have $\sim$ 6000 words of data to be read out, while a multihadron event might have ten times this. Wire list buffers can store up to 8k works, and pad list buffers can store up to 2k words. The digitized data in the buffer are read out by a VAX 11/780 computer. These data, after some preliminary error checking are then written to magnetic tape.

In order to calibrate the response of the entire signal processing chain, it is necessary to introduce test signals with reproducible amplitudes and rise times substantially shorter than the

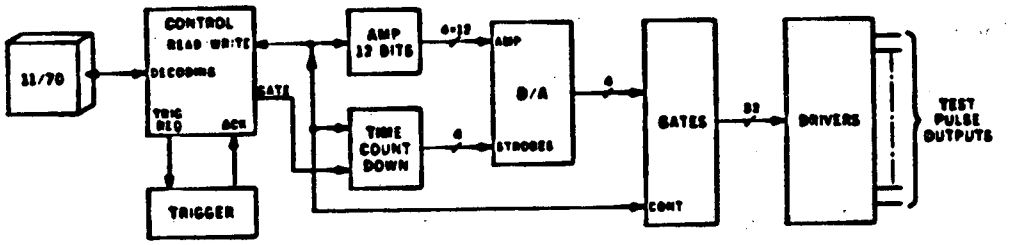

Figure 3.8: The electronics test pulsing system. Signals set by a 12 bit DAC are sent by a MOSFET driver to the shielding grid on the TPC sectors.

time constant of the shaping amplifiers. The pulsing system (figure 3.8) was composed of a digital to analog converter with 12 bit accuracy hooked to MOSFET drivers. The pulsing system could produce signals between 0 and 6.5 V with a rise time of 30 $nsec$, a 0.2 % linearity, and ≤ 1 % variation from channel to channel [33]. For both the wire and pad calibration, test signals from the MOSFET drivers are coupled to the shielding grid. The induced signal on the wires and pads are then used to produce a calibration curve for each discrete detector element. Calibration curves (figure 3.7) were fitted by cubic splines, with maximum deviations from the curves on the order of one to three counts [34].

3.3.5. Track reconstruction

The first step in track reconstruction is refered to as cluster finding. The production of clusters in the raw data is schematically illustrated in figure 3.9. First, the digitized data are reordered into individual detector elements as a function of CCD bucket number. These reordered data are scanned to find local pulse height maxima. Any local maximum at least 5 counts higher than neighboring peaks is labeled a cluster. A parabolic fit is then made to the highest 3 buckets in each cluster. From this fit, the pulse height, pulse width, and z position of the cluster are

determined. Since the z coordinate is the result of a fit to several samples, it is possible to obtain a position resolution better than the width of the CCD bucket, but since the shape of the z cluster also depends on the shaping response of the amplifiers, the determination of the z cluster position will not be as accurate as the determination of the pad cluster position.

In order to obtain an accurate measurement of the z location of a cluster, we must know the drift velocity. Changes in the drift velocity due to systematic shifts in pressure, temperature and drift field could be corrected for from monitored information [35]. However, because of unmeasurable changes in the there was a substantial variation (~ 1 %) in drift velocity over the course of the running cycle which could not be corrected. Changes in the methane fraction on the order of 4 % would be necessary to account for the changes in drift velocity of this size, it is also possible that impurities were responsible for these fluctuations. Two passes were made on the data to determine constants such as electron attenuation, drift velocity, overall gain, *etc* . On the first pass, the locations of the clusters are plotted as a function of CCD bucket number. Figure 3.10 shows such a plot, the sharp edges are the physical boundaries of the detector, (the sectors and the HV membrane). From fits to these edges, the drift velocity, and origin of the z coordinate are determined on a run by run basis to an accuracy of about 0.5 mm for ionization drifting over the entire 1 m length. The measured drift velocity is then used on subsequent analysis passes to assign accurate z coordinates for clusters.

Two other effects had to be corrected for in determining the z coordinates of clusters. Even with the wide copper strips on the field cages, the electrostatic charging caused distortions on the order of 1 mm within 4 cm of the field cages. It was possible to parameterize these distortions so that they could be measured and corrected for on a run by run basis. From the first analysis pass, the magnitude of this effect was calculated as a function of both z and radius, and was corrected for on the second pass [27]. In addition to this, it was discovered that there was a temperature gradient of $\sim 3.0^{o}$ C from the top to bottom of the TPC active volume. With this gradient, the ionization will drift at different rates at the top and bottom of the TPC, resulting in a systematic distortion of up to 4 mm. This, too, was corrected for in subsequent analysis passes.

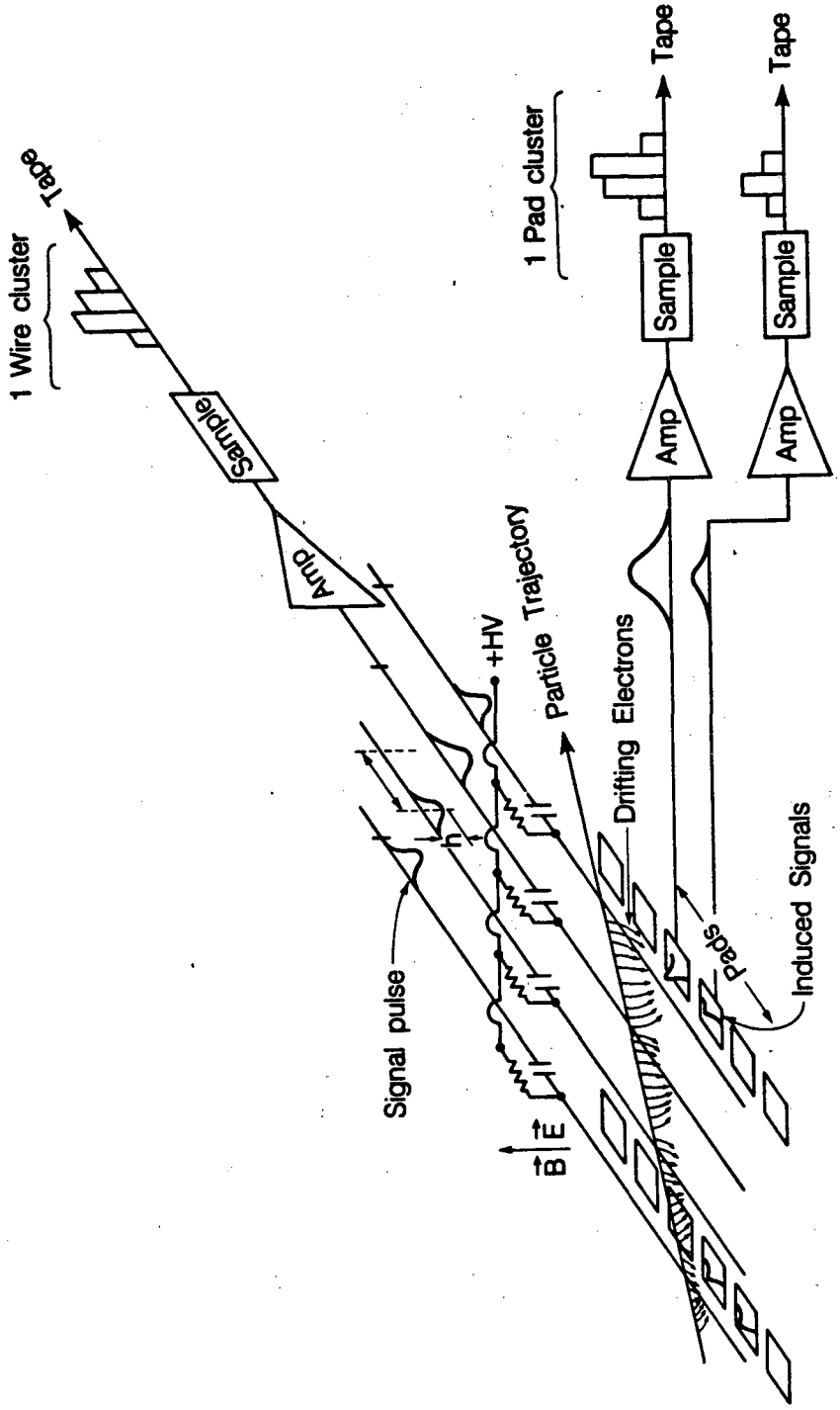

Figure 3.9: Illustration of track clusters seen on one wire and two pad channels. The wire cluster consists of 5 to 7 CCD buckets. The pad cluster (in this case) consists of two z clusters on neighboring pads.

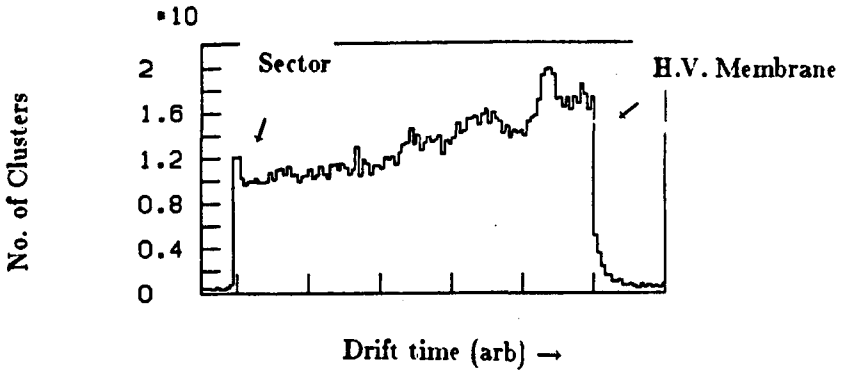

Figure 3.10: The location of clusters as a function of drift time. The sharp edges are from the physical boundaries of the drift volume. This distribution was used to determine the drift velocity on a run by run basis.

After the pad z clusters are formed, these are then scanned to find neighboring pads with z clusters at roughly the same z position. If the pulse heights of 2 or more neighboring pads form a local maximum as a function of pad number, the associated pad z clusters are tagged as an η cluster. The cluster location in the coordinate perpendicular to the drift direction, η, is determined from the centroid of the pad pulse heights when 2 pad are fixed on a cluster. When 3 or more pads are associated in a cluster, a Gaussian fit to the 3 pulse heights is used to determine not only its η coordinate but also the width of the cluster.

The charge imaged on one pad row from a single track will have contributions from the proportional signals on the nearest five wires to the pad row. The width of the resulting pad response will depend on the pulse heights on these wires, the track inclination with respect to the pad row, α, (see figure 3.11), the magnetic field, the wire spacing, and the drift length. As a function of η, the coordinate along the pad row, the spatial distribution of the induced charge on the pad row will be the sum of five Gaussians, one for each wire [36]:

$$PH_{pad}(\eta) \propto \sum_{i=-2}^{2} w_i H_i e^{-\eta_i^2/2\sigma^2} \tag{3.1}$$

where

i stands for wire number ($i = 0$ is centered on the pad row, $i = \pm 1$ is on the edges of the pad row *etc*)

H_i is the pulse height on the ith wire

PH is the pad pulse height

η_i is the distance along the pad row from the avalanche on the ith wire to the center of the pad

σ is the intrinsic width of the pad response from the avalanche on one wire

w_i is a geometrically determined weight for each wire

The weights are: $w_0 = 0.239$, $w_{\pm 1} = 0.117$, and $w_{\pm 2} = 0.0135$ [36]. The width of the pad response, σ is typically 4 mm. If one includes the effects of diffusion, the magnetic field, and track inclination, the pad response, σ , can be written as [36]:

$$\sigma = \left[\sigma_o^2 + \sigma_D^2 \frac{L}{L_m} + \left(\sigma_D^2 \frac{L}{L_m} + \sigma_\alpha^2\right) tan^2\,\alpha - \frac{2D^2}{12}\, tan\beta\, tan\alpha + \frac{D^2}{12} tan^2\beta\right]^{\frac{1}{2}} \qquad (3.2)$$

where

L_m is the maximum drift length ($= 1\ m$)

D is the spacing between wires ($4\ mm$)

σ_o is the intrinsic width ($3.6\ mm$)

σ_D and σ_α are related to the α dependence ($\sigma_\alpha = 3.5\ mm$, $\sigma_D = 1.4\ mm$)

β is related to the avalanche spreading out in the presence of a magnetic field (see figure 3.11)

The first term is the intrinsic response of the pad to a point source of ionization causing an avalanche at the sense wire. The second and third term are the result of the transverse diffusion of the electrons as they drift to the endcaps. The last two terms arise because the magnetic field will tend to spread out the avalanche along the sense wire. With no magnetic field, the track ionization will follow a path perpendicular to the wire as the avalanche develops (dashed line in figure 3.11). In the presence of a magnetic field, $E \times B$ effects will skew the actual path followed by an angle β, as shown in figure 3.11. With the TPC operating parameters described earlier $\beta = 4.2^o$ [36],

After clusters in the TPC have been determined, the pad clusters are used by a pattern recognition program to find charged particle tracks. Since the pad information is essentially

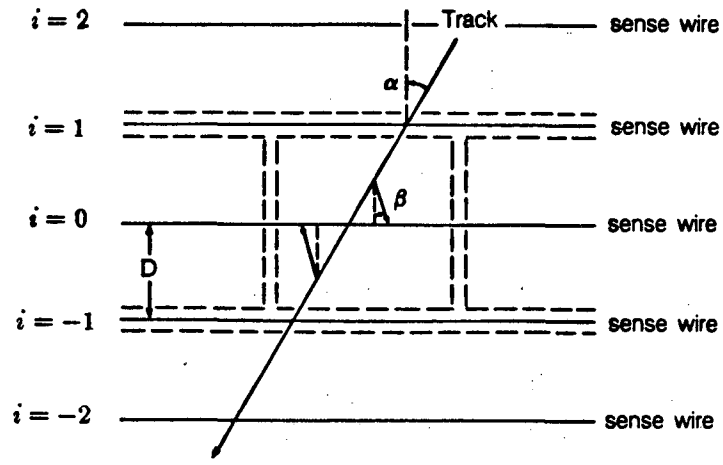

Figure 3.11: Illustration of the variables used in pad cluster reconstruction.

three dimensional, the TPC has a unique ability to reconstruct tracks, particularly in complicated multihadron events. This is to be contrasted to other colliding beam detectors which must rely on projective geometries or charge division to reconstruct track coordinates in all three dimensions. The pattern recognition program uses the "histogram" and "two " and "three point" algorithms [37]. A track must have at least 4 pad clusters on it for it to be detected by the reconstruction software. Because of electrostatic distortions, the pad row closest to the inner radius field cage was not used in track reconstruction. From hand scans of the data, it is estimated that the track reconstruction efficiency is 95 % for track with at least 4 pad clusters. After a rough fit is obtained for the trajectory, a detailed fit is applied, which includes an extrapolation through the beam pipe, and the effects of energy loss and multiple scattering.

The position resolution for tracks in the TPC can be determined from residuals to the fitted trajectories. The z resolution, determined using cosmic rays is $\sigma_z = 340 \pm 5\ \mu m$ [36]. The resolution in the bending plane, σ_{xy} is typically 180 μm, but will depend on its inclination with respect to the pad rows , α. In general, the α dependence of σ_{xy} can be written as [36]:

$$\sigma_{xy}^2(\alpha, L) = \sigma_A^2 + \sigma_B^2 \frac{L}{L_m} e^{\gamma L} \sec\alpha + \sigma_C^2 e^{\gamma L} \cos\alpha \tan^2\alpha \tag{3.3}$$

where

γ is the electron attenuation ($\sim 0.06\ m^{-1}$ in the TPC).

L is the drift length

L_m is the maximum drift length ($1\ m$)

σ_A represents the intrinsic resolution of the detector, this is limited by ionization statistics, electronic noise, and the pad width ($\sigma_A = 160 \pm 2\ \mu m$). The second term arises because transverse diffusion will vary over the drift length. For operating conditions, $\sigma_B = 105 \pm 6\ \mu m$ [36]. Fluctuations in the avalanche process give will tend to smear out the track location, reducing the resolution. The third term is the result of this smearing, with $\sigma_C = 249 \pm 7 \mu m$ [36]. Both the second and third term in (3.3) have a factor, $e^{\gamma L}$, which is the result of electron attachment over the drift length.

The momentum resolution for energetic tracks ($\geq 1.5\ GeV/c$) where multiple scattering is negligible, is $\Delta p_\perp / p_\perp^2 \approx 4.5\ \%$ where p is measured in GeV/c. If the track fit is vertex constrained, the resolution is $3.7 \pm 0.3\ \%\ (GeV/c)^{-1}$.

Details of the $< dE/dx >$ reconstruction are given in the next chapter.

3.4. Triggering

Since this dissertation is concerned primarily with charged particle data, only the relevant charged particle triggers employed in the PEP-4 detector will be discussed. The low angle Bhabha trigger, necessary for luminosity monitoring, will also be described. There are 2.45 μsec between between beam crossings. Since it takes $\sim 20\ \mu sec$ for tracks to drift the length of the TPC, a fast pretrigger ($\sim 2\ \mu sec$) is needed to determine on which beam crossing an event was produced. This pretrigger was provided by fast signals from the IDC, the ODC, and from prompt signals seen on the sense wires from tracks going through the sectors. The final trigger used information from the TPC sense wires, and could trigger on tracks pointing back to the beam-beam crossing point.

An IDC or ODC "hit" is defined if a pair of cells in different layers but with the same

azimuth fire within $\sim 0.5\mu sec$ of a beam crossing. The single cell efficiency is estimated to be 99 % in both chambers, however, the IDC was run with only two layers active because of voltage breakdown problems caused by deposits in the chambers. This efficiency is expected to be true for tracks with as little as 10 % of the ionization deposited from charge-1e tracks [38]. For triggering purposes, the IDC and ODC are both divided into twelve 30° sections in azimuth (see figure 3.12).

There are fast discriminators connected to the output of the TPC wire shaping amplifiers. The discriminators can be set to fire if a signal is above a preset threshold , which varies from 1 to 16 on an arbitrary scale. Discriminator thresholds were typically 4, where 10 corresponds to the pulse height seen from a minimum ionizing charge-1e track [39]. The output of these discriminators are sent to logic units where trigger decisions are made. For triggering purposes, the wires on a sector were grouped into 23 radial groups of 8 wires . Each group of 8 wires is termed a majority unit. A majority unit is turned on if three out of eight wires in the unit have pulse heights over the discriminator threshold within a 2 μsec window. The sector signals were also ganged together azimuthally in pairs in what are termed supersectors (figure 3.12). There are 6 supersectors per endcap, consisting of overlapping segments, each covering 120° in azimuth; the overlap of a pair of neighboring supersectors is 60°. If a charged track from the beam-beam crossing goes through a sector, about 10 cm of drift length for that track can be seen in a 2 μsec window around the beam crossing. This information was used in defining a pretrigger.

The azimuthal and radial trigger elements for the IDC, ODC, and TPC are indicated in figure 3.12.

The following two conditions were used to define a pretrigger:

1. An IDC hit **AND** a prompt TPC majority hit on one of the supersectors overlapping the IDC azimuthal section. The TPC majority hit had to occur in the upper half of the sector.

2. An IDC hit **AND** an ODC track hit in the corresponding or one of the adjacent ODC azimuthal sections.

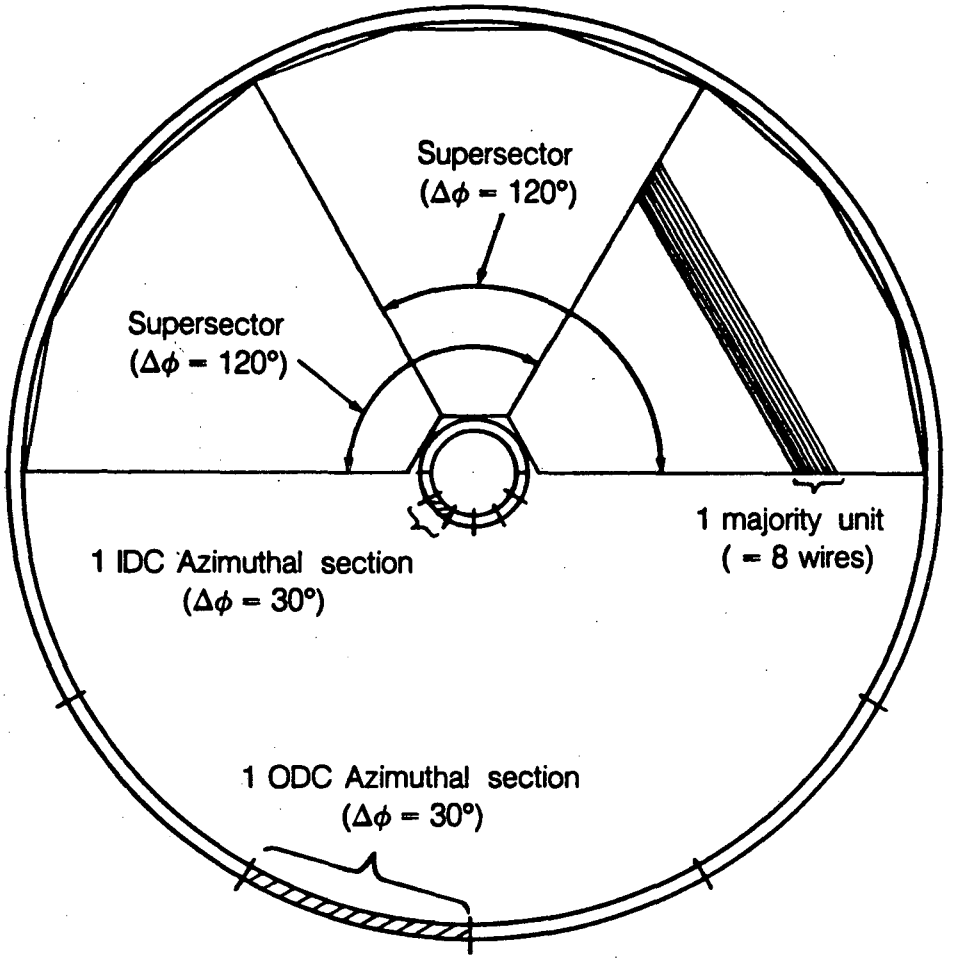

Figure 3.12: Azimuthal groupings of IDC, ODC and TPC detector elements into trigger units. The TPC supersectors consist of 6 overlapping pairs of sectors, each covering 120° in azimuth.

For a pretrigger to be satisfied, there had to be a coincidence of two separate instances of either of the above conditions within 2 μsec of a beam crossing. Said another way: either 1 and 2, or 1 and a separate 1, or 2 and a separate 2 would define a pretrigger. Pretrigger rates ranged from 0.5 to 1 kHz, depending on beam conditions. Because the first pretrigger requires a track to go through the upper half of the sector, this restricts the triggerable dip angles to the range, $60^o \geq \theta \geq 45^o$. Only tracks with a dip angle smaller than 45° will satisfy the second pretrigger above. Because of track curvature in a magnetic field, some low momentum tracks will not satisfy the above triggers. 60 MeV/c and 85 MeV/c are the minimum values of $p_\perp$ that will satisfy the above pretriggers.

One important feature of the TPC triggering configuration was the ability to trigger on beam associated tracks by extrapolating in the z coordinates. A *ripple* is defined for a TPC track if a line of majority hits can be formed which point to within ± 20 cm of the beam-beam crossing [40].

A trigger was satisfied by the logical **OR** of the following conditions:

TPCT The majority latches are ganged into groups of eight, dividing each sector into three. TPCT is true if all three of these groups are true on one endcap, and two of these groups are true on the other endcap. In addition to this, a ripple had to be found pointing back to the beam crossing. This is used to trigger on tracks with near zero dip angle. (typical rate $= 0.05\ sec^{-1}$)

TPCS TPCS is true if 2 or more ripples are found in non-adjacent sectors. (typical rate $= 0.7\ sec^{-1}$)

COPL The COPL (for coplanarity) trigger was true if there were hits in back to back sections of either the IDC or ODC, in conjunction with a single ripple in a supersector overlapping one of the hit drift chamber sections. (typical rate $= 0.05\ sec^{-1}$)

COLN (colinearity) is true if there are IDC hits in back to back azimuthal sections in conjunction with one ripple trigger in a corresponding supersector, and back to back majority hits

in corresponding supersectors, in opposite endcaps. (typical rate = 0.05 sec^{-1})

Trigger rates were typically 1 Hz. The live time during data acquisition averaged 80 %. The estimated triggering efficiency for multihadron events, 99 %, was quite high because of the large multiplicity of these events [39].

For luminosity monitoring purposes, the pole tip calorimeters were used to count low angle Bhabha scattering events. A Bhabha trigger was "true" if there was at least 4 GeV/c in each PTC module. Typical PTC Bhabha trigger rates were 0.3 Hz.

3.5. Luminosity Monitoring

The integrated luminosity for data runs was determined by counting the low angle Bhabha scattering rate. Both the wide angle Bhabha rate into the HEX calorimeter , and the number of multihadron events were used to corroborate the derived luminosity. The angular range of acceptance of the Bhabha trigger was limited to between 15.6° and 32.9° in the polar angle (0 = beam axis) [41]. For a Bhabha event to be counted, in addition to satisfying the Bhabha trigger detailed above, each electron had to have at least one third of the beam energy. The maximum acolinearity angle allowed between showers was 10° [41]. Including detection efficiency, and radiative corrections, this number was used to derive the luminosity from QED predictions, with the recipe

$$\mathcal{L} = .102\, nb^{-1} \times N_{Bha}$$

The systematic uncertainty in the luminosity measured in this way is put between 6 and 10 % [41]. In all, the total luminosity for the Spring 1983 running cycle was found to be $77 \pm 6\, pb^{-1}$, where the error assigned is systematic, [42].

Chapter 4.

Energy loss measurement in the TPC

Quarks and diquarks are fractionally charged ($\frac{1}{3}e, \frac{2}{3}e, \frac{4}{3}e$), and if produced as free particles will ionize matter differently than charge-1e particles. The TPC identifies charged particle species through a simultaneous measurement of momentum and ionization, and although designed primarily to identify $Q = 1e$ particles, it is sensitive to these fractionally charged particles in certain domains of ionization, mass and momentum. The energy loss per unit length, $< dE/dx >$ is a function of the charge and velocity of the incident particle, and of the characteristics of the medium. In gaseous detectors, such as the TPC, the energy loss curves assume a characteristic shape, (figure 4.1), falling as $1/\beta^2$ ($\beta = v/c$) at low velocities, going through a minimum and then rising logarithmically with $\beta\gamma$ until it reaches a constant value. If one plots $< dE/dx >$ versus *momentum* rather than velocity, the charge-1e particles will fall along curves with this characteristic shape but displaced along the momentum axis, as shown in figure 4.2.

As will be discussed later, the ionization curves of fractionally charged particles have qualitatively the same shape but are shifted in both $< dE/dx >$ and measured momentum relative to the $Q = 1e$ population. Since the energy loss of a charged particle scales approximately as its charge squared, the $< dE/dx >$ curves are expected to shift by a factor of $\sim Q^2$. Because track curvature in a magnetic field also depends on charge, the apparent momentum, (or rigidity) p/Q, will shift for fractionally charged particles by a factor of $1/Q$ relative to the charge-1e population.

In order to be sensitive to small numbers of free quarks and diquarks, one must search in regions of $< dE/dx >$ and apparent momentum not populated by the stable $Q = 1e$ particles (e, p, K, π, μ). The search regions will be dictated by the shape of the charge-1e ionization

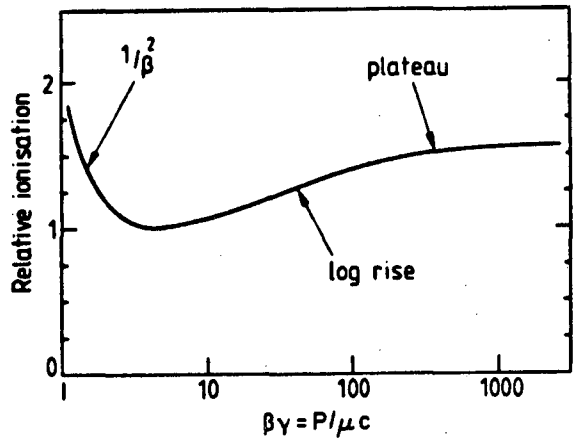

Figure 4.1: Plot of energy loss per unit length, $< dE/dx >$ as a function of the product of the kinematic variables $\beta\gamma$.

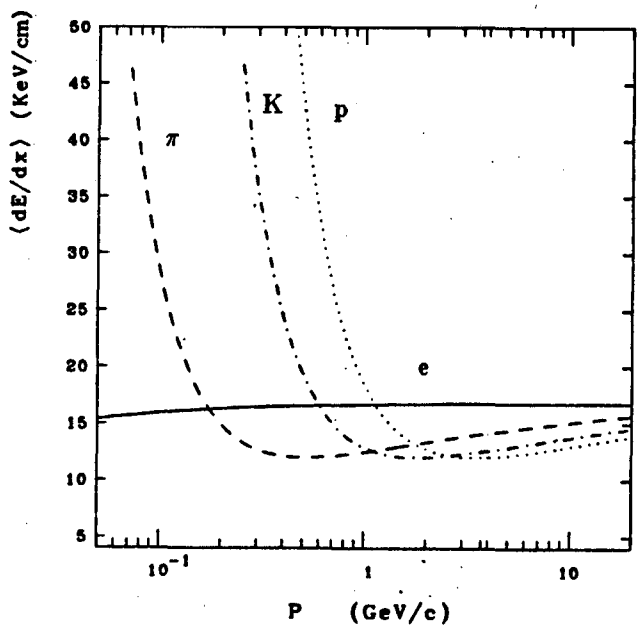

Figure 4.2: Curves of expected $< dE/dx >$ vs. momentum for the stable charge-1e particles p, K , π, and e. The curves are calculating assuming the TPC operating conditions, detailed in chapter 3.

curves, and the detector resolutions in these variables. As will be shown, the requirements of relativistic charged hadron identification and a sensitive free quark search put similar constraints on the $< dE/dx >$ resolution. We must also know where the expected $< dE/dx >$ curves of the fractionally charged particles lie with reasonable accuracy in order to calculate efficiencies.

$< dE/dx >$ as measured in a multiwire proportional chamber, such as the TPC, is not a single measurement, but a fit to or average of many samples of ionization for each particle collected at the sense wires. The ionization spectrum seen at the wires for a single particle is both very broad and asymmetric, accordingly many samples are required to achieve high resolution both through statistics, and by throwing out the long, high energy tail of this spectrum. The detailed shape of the $< dE/dx >$ curves, and the $< dE/dx >$ resolution will be determined not only by the details of the atomic collisions between the incident particle and the medium, but also by the way one reconstructs $< dE/dx >$ from the data. In this chapter, a parameterization for $< dE/dx >$ as a function of velocity and charge will be described, along with the factors affecting the $< dE/dx >$ resolution in the TPC.

4.1. $< dE/dx >$ as a function of $\beta\gamma$, and charge.

The energy loss of a charged particle results from the coupling of its electric field to atoms in the medium it traverses, with the dominant contribution coming from atomic excitations. Qualitatively, the probability of exciting an atom in a medium scales as the square of the transverse component of the incident particle's electric field with respect to its velocity vector. This can be understood in terms of the "golden rule" from perturbation theory: the atomic transition probability goes like the square of the amplitude, and this, in turn, is proportional to the transverse field strength. By symmetry, the longitudinal component of the electric field will not contribute to the transition amplitude. From this scaling, it is not difficult to see that the transition probability, and hence the energy loss will scale as the charge of the incident particle squared. One can also relate the different regions of the $< dE/dx >$ curve to how the transverse component of the electric field scales with the kinematic variables β and γ.

The $1/\beta^2$ part of the ionization curve arises because as the velocity of the incident particle increases, it spend less and less time near any single atom in the medium, with no appreciable increase in the transverse field strength. When the velocity approaches the speed of light, the amount of time spent near any atom tends to a constant value. At these velocities, another effect comes into play: the Lorentz contraction causes an increase in the transverse component of the electric field with $\beta\gamma$. Due to this increase, the energy loss scales as $ln(\beta\gamma)$. At even higher values of $\beta\gamma$, because of the shielding effect of atomic polarization, the energy loss curve levels out onto the relativistic plateau. Atoms in the medium will have a polarization proportional to the transverse electric field strength, and when $\beta\gamma$ of the incident particle goes beyond a certain range, its increased field will be exactly compensated by the increased amount of shielding, resulting in a constant value of $< dE/dx >$. The actual range of $\beta\gamma$ at which the the relativistic plateau is reached is determined by the properties of the medium [44].

On the basis of a relatively simple derivation (*cf* reference [45]), one can write a good approximation to the average energy loss per unit length, $< dE/dx >$ as:

$$< dE/dx > \approx \frac{4\pi n Q^2 e^2}{m_e c^2 \beta^2} \left\{ ln \left(\frac{2 m_e \beta^2 \gamma^2}{I^2 + (\hbar\omega)^2 \beta^2 \gamma^2} \right) - 2\beta^2 \right\} \tag{4.1}$$

where

I is the logarithmic mean atomic ionization potential

ω is the plasma frequency of the medium

n is the electron density of the medium

m_e is the electron mass

e is the electron charge

Q is the charge of the incident particle

The $1/\beta^2$ scaling of the curve for non-relativistic velocities is apparent from the term in front of the curly brackets. The logarithmic rise with $\beta\gamma$ and subsequent plateau are both apparent from the arguments of the logarithm. It is important to note that the onset of the relativistic plateau,

and the slope of the logarithmic rise are determined by the relative values of I and $\hbar\omega\beta\gamma$ in the denominator of logarithm. One can see that gases with larger ionization potentials will have larger relativistic rises than media with lower values of I. For detectors designed to separate $Q = 1e$ particles on the $ln(\beta\gamma)$ part of their ionization curves, one typically chooses a gas with a large ionization potential, such as argon, so that the $< dE/dx >$ separation in the relativistic rise is as large as possible.

Another effect contributing to the energy loss results from the Rutherford scattering of atomic electrons by the incident particle. These are termed knock-on electrons, or δ-rays. The probability of an energy transfer, ΔE, to electrons from Rutherford scattering goes as $1/(\Delta E)^2$, and extends out to the kinematic limit of energy transfer, which can be substantial for relativistic incident particles. With the approximation that the mass of the incident particle is much greater than the electron mass, then the maximum energy transfer can be written as:

$$\Delta E_{max} \approx 2m_e\beta^2\gamma^2 \tag{4.2}$$

For typical values of $\beta\gamma$ found in hadronic final states at PEP energies this limit can be several hundred MeV, meaning that secondary electrons appearing as relatively stiff tracks in the detector can be produced. The $1/(\Delta E)^2$ dependence of the Rutherford scattering cross section is responsible for the long high energy tail of the ionization distribution.

A realistic treatment of energy loss in a gaseous detector, containing, for example, argon, must include the effects of many atomic energy levels, and the contribution of the δ-rays. A treatment along these lines [46] is used to fit the TPC charged particle data, and is the basis for the calculation of the detection efficiencies of fractionally charged particles. A convenient starting point is the inelastic differential cross section, $(d^2N/dxdE)$ for a charged particle in a dense medium. The *average* energy loss per unit distance can be found by integrating this cross section over $E\,dE$ up to the maximum allowed energy transfer E_{max}:

$$< dE/dx >_{average} = \int_0^{E_{max}} \left(\frac{d^2N}{dxdE}\right) E\,dE \tag{4.3}$$

There are three contributions to the inelastic cross section,

$$\left(\frac{d^2N}{dxdE}\right) = \left(\frac{d^2N}{dxdE}\right)_{exc} + \left(\frac{d^2N}{dxdE}\right)_{\delta} + \left(\frac{d^2N}{dxdE}\right)_{\check{C}} \tag{4.4}$$

This includes the contributions from atomic excitations, δ-ray production, and from Čerenkov emission. The Čerenkov term contributes less than 1 % to the overall $< dE/dx >$ and will be neglected here. As input to the inelastic cross section, one needs some measure of how likely a given energy, E, is to be transfered to the atoms in the medium. This measure is a function representing the detailed structure of atomic absorption levels, and is refered to as the generalized oscillator strength, $f(E)$. For some arbitrary $f(E)$, the inelastic cross section for excitations can be written as [46]:

$$\left(\frac{d^2N}{dxdE}\right)_{exc} = \frac{\alpha Q^2 P}{\beta^2}\frac{f(E)}{E}\left[ln\left(\frac{2m_e v^2\gamma^2}{E(1+\beta^2\gamma^2(1-\epsilon))}\right) - \beta^2 Re(\epsilon)\right] \tag{4.5}$$

where

P is the gas pressure in atm

α is a constant containing the factors of electron density (123 $eV/atm\ cm$ for Ar)

ϵ is the complex index of refraction of the medium

E is the energy loss in the collision (in eV)

Note that this expression is quite similar to equation (4.1). This is no accident, for if one were to take $f(E)$ to be a single delta function at an energy I, (ie if $f(E) = \delta(I)$) then from integrating over $E\ dE$, one would obtain a result with much the same form as (4.1).

The δ-ray term results from quasi-free scattering of electrons by the incident particle, and is simply the Rutherford scattering cross section. If we take into account the atomic binding energy, the ionization term can be written as [46]:

$$\left(\frac{d^2N}{dxdE}\right)_{\delta} = \frac{\alpha Q^2 P}{\beta^2}\frac{(1-\beta^2 E/E_{max})}{E^2}\int_0^E f(E')dE' \tag{4.6}$$

Here E_{max} is the same kinematic limit as in (4.2), and α is the same as in equation (4.5).

In order to turn $(d^2N/dxdE)$ into an energy loss, one must integrate over EdE. To do this some model is needed for $f(E)$, the atomic oscillator strength. This simplest approximation would be to take $f(E)$ as a single δ function, representing the logarithmic mean ionization potential for the gas. A slightly more involved approach would be to approximate each level in the gas as a δ

function, and sum $(d^2N/dxdE)$ over all levels. With reasonable accuracy, one can approximate $f(E)$ with the photoabsorption cross section [47], reflecting the fact that the ionization and excitation of atoms in the medium are driven by the flux of virtual photons surrounding the incident particle. Figure 4.3 shows the photoabsorption cross section for argon as measured with x-rays. An analytic model of this will give reasonable predictions for $< dE/dx >$ (accurate to $\sim 1\ \%$). One can break up $f(E)$ into a sum over oscillator strengths for individual levels, as

$$f(E) = \sum_i W_i f_i(E) \tag{4.7}$$

where W_i represents the probability of exciting the ith atomic level (see table 4.1). For the TPC gases, each $f_i(E)$ can be parameterized by a function of the form [46]:

$$f_i(E) = \begin{cases} 0, & \text{if } E < E_i; \\ \frac{(S_i-1)}{E_i}\left(\frac{E}{E_i}\right)^{-S_i}, & \text{if } E_i < E < \infty \end{cases}$$

The constants, E_i, and S_i can be found from table 4.1 for argon and methane. This function approximates the "edge" like structure of the argon and methane photoabsorption cross sections. With this approximation, the excitation and δ-ray terms can be integrated to find $< dE/dx >$. The excitation term for the average $< dE/dx >$ is

$$< dE/dx >_{exc} =$$

$$\frac{\alpha Q^2 P}{\beta^2} \sum_i W_i \int_{E_i}^{E_{max}} \frac{(S_i-1)}{E_i}\left(\frac{E}{E_i}\right)^{-S_i} \left\{ ln\left(\frac{2m_e v^2\gamma^2}{E(1+\beta^2\gamma^2(1-\epsilon))}\right) - \beta^2 Re(\epsilon)\right\} dE \tag{4.8}$$

An approximation for ϵ can be made for each level; this is [45]:

$$(1-\epsilon) = \frac{\omega^2 P}{E_i'} \tag{4.9}$$

here P is the gas pressure (in atm), and ω is a constant which takes the value of $0.82\ eV/atm^{\frac{1}{2}}$ for argon. The product, $\omega\sqrt{P}$ is the plasma frequency of the medium. For the TPC operating conditions, $\omega = 0.77$. Here we have introduced the notation

$$E_i' \equiv E_i e^{\frac{1}{S_i-1}} \tag{4.10}$$

The excitation term can now be evaluated, and with the above substitution, one obtains

$$< dE/dx >_{exc} = \frac{\alpha Q^2 P}{\beta^2} \sum_i W_i \left\{ ln\left(\frac{2m_e v^2\gamma^2}{E_i' + \beta^2\gamma^2\omega^2 P/E_i'}\right) - \beta^2 \right\} \tag{4.11}$$

in the limit that $E_{max} >> E_i'$. Note that in the above equation each energy level, E_i, has a different value for the logarithmic rise, which also depends on the operating pressure. Higher pressure means a lower value of $\beta\gamma$ for the onset of the plateau, and hence less separation between relativistic charge-1e species.

The δ-ray term to be evaluated is

$$< dE/dx >_\delta =$$

$$\frac{\alpha Q^2 P}{\beta^2} \sum_i W_i \int_0^{E_{max}} \left\{ \frac{(S_i - 1)}{E_i} \frac{(1 - \beta^2 E/E_{max})}{E} \int_0^E \theta(E' - E_i) \left(\frac{E'}{E_i}\right)^{-S_i} dE' \right\} dE \quad (4.12)$$

here θ is just the step function. With the approximation that $E_{max} >> E_i'$ this yields:

$$< dE/dx >_\delta = \frac{\alpha Q^2 P}{\beta^2} \sum_i W_i \left\{ ln\left(\frac{E_{max}}{E_i'}\right) - \beta^2 - \left(\frac{1}{S_i - 1}\right) \right\} \quad (4.13)$$

To find the total energy loss, we must add the excitation and δ-ray contributions together, this gives:

$$< dE/dx > = \frac{\alpha Q^2 P}{\beta^2} \sum_i W_i \left\{ ln\left(\frac{2m_e v^2 \gamma^2 E_{max}}{E_i^2 + \beta^2\gamma^2\omega^2 P}\right) - 2\beta^2 - \left(\frac{1}{S_i - 1}\right) \right\} \quad (4.14)$$

Table 4.1 gives the values of W_i, S_i, E, and E_i' for the argon K,L and M shells; also are shown the values for the methane levels. It should be noted that even the above equation is incomplete; some energy loss processes have been neglected, such as the ionization from δ-rays, which can lose energy through atomic excitations and subsequent ionization. The best way to calculate the expected energy loss is through a detailed computer simulation which models not only the atomic processes, but also characteristics of the detector, such as finite sample thickness, the proportional process, angled tracks, *etc*. Such a simulation has been written, but is very time consuming to run and is not as practical as an analytic approximation.

With a knowledge of how energy loss scales with $\beta\gamma$, it is possible to identify singly and fractionally charged particles by making a simultaneous measurement of $< dE/dx >$ and momentum. Equation (4.14), a good approximation for $< dE/dx >$, is a function of the incident particle's velocity and charge alone. Mass does not play a role; this is because $< dE/dx >$ depends only on the electric field of the incident particle. If one measures $< dE/dx >$ and momenta of different

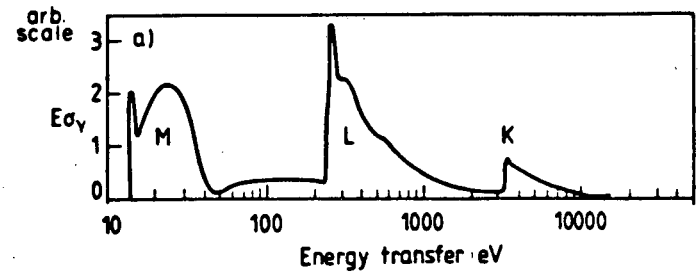

Figure 4.3: Argon photoabsorption cross section, from reference [47].

Level	W_i	S_i	E_i (eV)	E_i' (eV)
Ar K	0.111	2.75	3206	5677
L	0.444	2.29	248	538
M	0.133	3.20	52	82
M	0.311	3.20	16	25
CH_4	0.8	2.15	12	27
CH_4	0.2	2.52	283	546

Table 4.1: Values of parameters used in determining the energy loss curves.

species of $Q = 1e$ particles, one will find a set of curves with similar characteristics (ie. value of minimum ionization, plateau, etc.), but displaced in momentum relative to each other. Figure 4.2 shows the curves of expected $< dE/dx >$ vs momentum for the stable charge-$1e$ particles e, p, K and π from equation (4.14), using a 20 % CH_4 80 % Ar mixture at 8.5 atm as input parameters. One of the goals prompting the construction of the TPC was the separation of relativistic kaons and pions by using $< dE/dx >$ measurements. The $K - \pi$ separation on the logarithmic rise is typically 15 % in $< dE/dx >$ for the TPC operating conditions. For a five standard deviation separation of these particles at a momentum of 4 GeV/c, a $< dE/dx >$ resolution on the order of 3 % is required.

The simultaneous measurement of momentum and $< dE/dx >$ is also the basis for the fractional charge search. As seen in equation (4.14), $< dE/dx >$ scales as $\sim Q^2$; this means that the overall scale of ionization for $Q = \frac{1}{3}, \frac{2}{3}$, and $\frac{4}{3}e$ particles will scale in $< dE/dx >$ by factors $\approx \frac{1}{9}$, $\frac{4}{9}$ and $\frac{16}{9}$ relative to the $Q = 1e$ particles. Because the momentum in the TPC is inferred from a measurement of track curvature, and since curvature scales as Q, the rigidity, or apparent

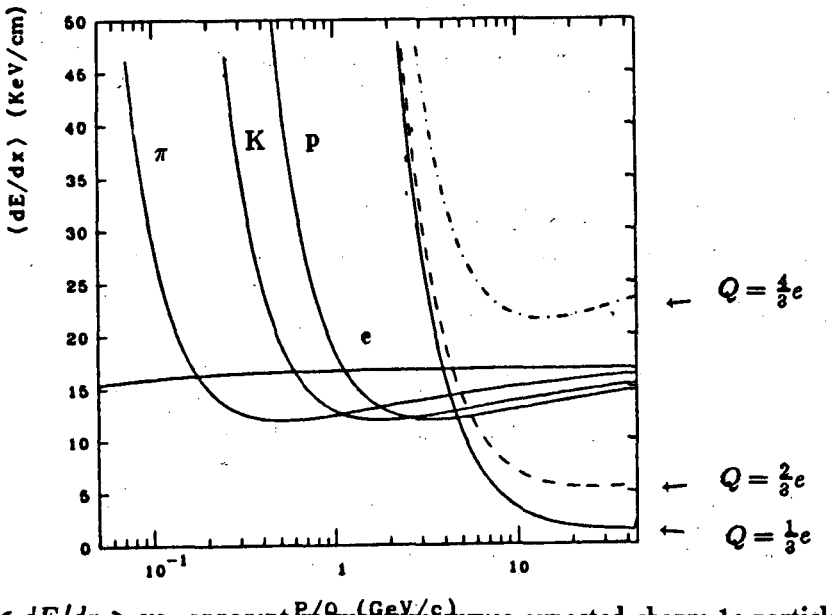

Figure 4.4: $< dE/dx >$ vs. apparent momentum curves expected charge-1e particles π, K, p, and e, and for $Q = \frac{1}{3}, \frac{2}{3}$, and $\frac{4}{3}e$ particles with a mass of 5 GeV/c^2.

momentum, p/Q for fractionally charged particles will be shifted by a factor of $1/Q$ relative to the $Q = 1e$ population. The curves expected for $Q = \frac{1}{3}, \frac{2}{3}$, and $\frac{4}{3}e$ particles with a mass of 5 GeV/c^2 are shown in figure 4.4 against the $Q = 1e$ curves. Since at most, a tiny yield of fractionally charged particles is expected, one needs good resolution to search in regions of $< dE/dx >$ and apparent momentum with little or no background expected from the stable charge-1e particles. As an example, consider the resolution needed to achieve a 10 standard deviation separation between relativistic electrons and $Q = \frac{4}{3}e$ particles at minimum ionization. With a minimum ionization for a charge-$\frac{4}{3}e$ particle expected at about $\frac{16}{9}$'s that for a charge-1e particle, and a relativistic plateau for electrons expected at about 1.4 times that of minimum ionization, such a separation implies a $< dE/dx >$ resolution of ~ 3 %. The requirements of $< dE/dx >$ resolution for relativistic particle separation and the fractional charge search are thus quite similar.

4.2. The energy loss distribution

The shape of the energy loss distribution will determine the $< dE/dx >$ resolution in the detector. As stated earlier, the actual spectrum of energy loss for charged particles is very broad

and asymmetric. The shape of the curve depends not only on factors such as atomic energy levels, velocity, etc., but also on sample thickness, which introduces operational questions as to how a real detector measures $< dE/dx >$.

There are two contributions to the shape of the energy loss distribution, the first is from atomic excitations. In the limit of a single δ function atomic energy level, the resulting energy loss distribution for thick samples will be a Gaussian, in which the width will obey $1/\sqrt{N}$ statistics, where N is the number of excitations per sample. For thin samples with few excitations, the energy loss will follow a Poisson distribution. The TPC energy loss distribution will be approximately Gaussian for M shell excitations ($\sim$ 80 per sample), and Poisson for K and L shell excitations ($\sim$ 4 and 0.03 per sample). As a consequence of the fact that the number of excitations varies with velocity, the corresponding width of the energy loss distribution will also be a function of velocity.

The second contribution to the shape of the energy loss distribution comes from δ-ray production The shape of the energy loss distribution for ionizations in thin samples was first described by Landau [48] for an idealized plasma. He derived the following approximation for the probability of seeing an energy loss Δ, in a sample of thickness x:

$$P(x,\Delta) = \frac{1}{2\pi i}\int_{-i\infty}^{i\infty}\left\{exp\left[p\Delta - x\int_0^{E_{max}}\left(\frac{d^2N}{dxdE}\right)_\delta (1-exp(-pE))\,dE\right]\right\}dp \qquad (4.15)$$

where

$(d^2N/dxdE)_\delta$ is the differential cross section from the Rutherford term

E and p are integration variables

E_{max} is the kinematic limit of δ-ray production

Although a complete treatment of this distribution is beyond the scope of this paper, some of the important features will be examined. The Landau distribution has a long, high energy tail which falls as $1/\Delta^2$, resulting from the energy dependence of the Rutherford scattering cross section. A relatively sharp rise to a maximum characterizes the low energy end of this distribution. The shape has a non-trivial dependence on both Q, the charge of the incident particle, and the sample

thickness, x. A good measure of how the shape changes with x and Q is the most probable value of Δ. In argon, this is given by [46]:

$$\Delta_{mp} = \frac{\alpha Q^2 P x}{\beta^2} \, ln \left(\frac{1.219 \alpha Q^2 P x}{\beta^2} \sum_i \frac{W_i}{E_i''} \right) \tag{4.16}$$

Where the variable,

$$E_i'' \equiv E_i \frac{S_i}{S_i - 1}$$

has been introduced; E_i, W_i, and S_i can be found in table 4.1.

The shape of the real energy loss distribution will be a superposition of Gaussians, Poissons, and a Landau distribution, all convolved with the detailed shape of the photoabsorption cross section of the chamber gas. For a minimum ionizing particle there will be ~ 90 excitations, and ~ 10 quasi-free scatters per 4 mm sample size at the TPC operating conditions. The resulting energy loss distribution is therefore mostly Gaussian, with some tail (figure 4.5). As before, the best way to find the expected energy loss distribution is to use a detailed computer simulation of all the gas processes, and to rely on empirical fits as a guide to an analytic approximation.

The width of the Gaussian part of the energy loss distribution will be a limiting factor in achieving good $< dE/dx >$ resolution. Sample thickness and pressure will partly determine this width; naively one might expect the resolution to scale as the square root of the number of excitations in the gas. For pions at minimum ionization, the energy loss distribution has a full width at half the maximum of ~ 55 %. In order to achieve the requisite 3 % resolution, one can go to very thick samples, or to high pressures, or both, thus increasing the number of atomic collisions per sample length. For the separation of relativistic particles, like π's and K's, one must also consider that increasing the pressure will also reduce the slope of the logarithmic rise.

One can gain in resolution by taking more samples of ionization, here the detector size and granularity are the limiting factors. The relationship between resolution and the number of samples, n will to some extent also depend on the shape of the energy loss distribution: for a δ function distribution, not many samples are necessary, for a perfectly flat distribution, an infinite number of samples will not give any information. Since the shape of the distribution is approximately Gaussian, one should improve the resolution as $\sim 1/\sqrt{n}$. With a finite number of

samples, the best method for reconstructing $< dE/dx >$ from the energy loss distribution is not clear. One approach [47] is to fit the distribution with some analytic function, from which one can derive $< dE/dx >$. This has the disadvantage that one needs a detailed model for how the distribution varies with mass, energy, path length, etc. In general it may be impossible to come up with function which is easily integrable, in which case $< dE/dx >$ reconstruction takes up much computing time. The approach adopted by the TPC is to use only the information in the Gaussian part of the distribution as a measure of $< dE/dx >$, this is because the Landau tail is very flat, and large fluctuations under this tail can significantly reduce $< dE/dx >$ resolution. This technique is refered to as the truncated mean algorithm.

Allison and Cobb [47] have derived a power law formula for the resolution of gaseous detectors as a function of sample thickness x (in cm), pressure, P (in atm) and number of samples n, based on a fitting algorithm. In terms of the resolution, R, as a % full width half maximum, they find a scaling law that goes as:

$$R = 96\, n^{-0.46} (xP)^{-0.32} \tag{4.17}$$

Walenta [49] found that a scaling law of the form $n^{-0.43}$ is appropriate in estimating $< dE/dx >$ resolution from a truncated mean algorithm. For the TPC pressure and sample thickness, R is expected to be ≈ 8 %, for 100 samples. This corresponds to a standard deviation of ~ 3 %, which is compatible with the resolution requirements detailed earlier. Note that the relationship between n and R follows approximately $1/\sqrt{n}$ scaling. Because of the scaling of resolution with n, one should require a minimum number of ionization samples for the identification of charged particles. For the fractional charge search, tracks were required to have at least 80 usable samples of ionization.

For the present analysis, the value of $< dE/dx >$ is *defined* to be the mean of the lowest 65 % of the energy loss samples. The choice of 65 % is somewhat arbitrary, as there is only a slight dependence of the $< dE/dx >$ resolution on the fraction of samples used in computing the mean of the truncated energy loss distribution [50]. One could, for example, use a 45 % or a 75 % truncated mean $< dE/dx >$ with little loss in resolution.

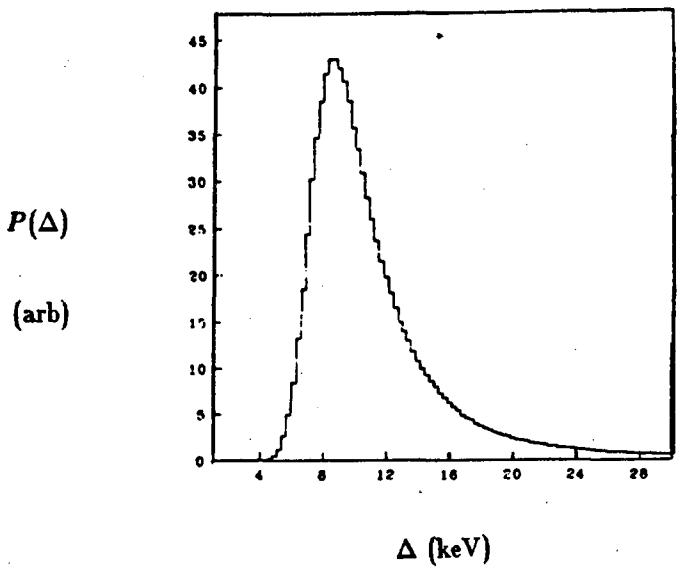

Figure 4.5: Energy loss distribution in the TPC.

With the above operational definition for $< dE/dx >$, it is apparent that neither the most probable value, nor the average value of $< dE/dx >$ will give an exact correspondence to the truncated mean $< dE/dx >$. A modified version of equation (4.14) is used to predict the ionization curves for both $Q = 1e$ and fractionally charged particles. This function is a mixture of empirical fits to the TPC data and the detailed atomic model described earlier. With the values taken in table 4.1 , the expected $< dE/dx >$ (in keV/cm) for a cell thickness x (in cm), taken from the 65 % truncated mean of the energy loss distribution is given by [46]:

$$< dE/dx >= \frac{\alpha p Q^2}{\beta^2} \left\{ \sum_i W_i ln \left(\frac{2m_e \eta^2}{E_i' + \eta^2 \omega^2 p / E_i'} \right) + A\ ln \left(\frac{1.219 \alpha p Q^2 x}{\beta^2} \sum_i \frac{W_i}{E_i''} \right) - \beta^2 \right\} \tag{4.18}$$

The constants in (4.18) are $\alpha = 123\ eV/atm\ cm$ and $\omega = 0.77\ eV/atm^{\frac{1}{2}}$. Here $\eta \equiv \beta\gamma$. The constant A is a free parameter of order unity which can be used to fit the log-length dependence from the data.

The second term in the curly brackets results from the changing shape of the Landau distribution with sample thickness, x, and charge, Q. The Q dependence of this term arises because of the Q^2 term in the Rutherford scattering cross section. Since the shape of the Landau curve will shift with Q and x, the truncated mean will also be affected. There is only $\sim 2\%$ deviation

of equation (4.18) from the idealized Q^2 dependence of $< dE/dx >$. Since the Q dependence of $< dE/dx >$ is of primary importance to the fractional charge search, it is of some concern how accurate equation (4.18) is, especially in the absence of fractionally charged particles as a calibrant. It is shown in appendix B, however that the detection efficiencies for free quarks do not strongly depend on small deviations from the above scaling.

Because of the changing shape of the Landau distribution with sample thickness, there will be a non-trivial dependence of $< dE/dx >$ on the inclination of tracks with respect to the sense wire plane. This dependence is difficult to derive analytically, especially with a truncation algorithm. In practice this dependence was measured using cosmic rays, and a correction factor was defined which normalized all $< dE/dx >$ measurements to a standard sample length. From equation (4.16) one sees that $< dE/dx >$ scales with the sample thickness as $ln(x)$. The actual correction factor used was

$$< dE/dx >_{corrected} = < dE/dx >_{measured} - 0.9 ln(x) \tag{4.19}$$

where x is in centimeters. This behavior is consistent with the results of detailed simulations [50]. All measurements of $< dE/dx >$ in the TPC are normalized to a sample thickness of 5 mm.

Figure 4.6 shows the prediction of equation (4.18), taking $A = 1$, along with the results of a ninth order polynomial fit to muons and electrons in the TPC. Both curves are normalized to the same value of minimum ionization, 12.1 keV/cm; this overall normalization is necessary because it is impossible to derive the absolute ionization scale to much better than 10 %, as a result of the various processes other than ionization through which tracks lose energy. The curves agree remarkably well, except for the value of the relativistic plateau, for which the data is $\sim 2.5\%$ lower than $< dE/dx >$ found from 4.18. The source of the discrepancy is not known, but this will not significantly affect the fractional charge search, as the momentum for particles other than electrons on the relativistic plateau must be at least ~ 100 GeV/c. The value of the relativistic plateau, taken from the $\pi - e$ separation in the charged particle data is 1.39 times that of minimum. Equation 4.18 predicts that this separation should be 1.41.

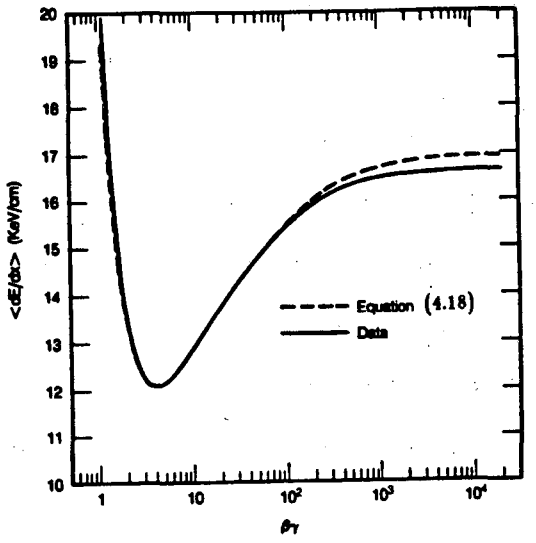

Figure 4.6: $< dE/dx >$ vs $\beta\gamma$ for Q=1e particles as predicted by equation (3.28), and from the TPC data. The curve representing the data comes from a ninth order polynomial fit to muon and electron data.

4.2.1. Practical considerations

Recall that both the quark search and relativistic hadron identification require $\sim 3 - 4$ % $< dE/dx >$ resolution. Since the intrinsic resolution is ~ 3 %, one must ensure that systematic shifts in the energy scale are below the 1 % level. These systematic shifts include electron attachment, wire dependent gain shifts, non-linearities in the proportional process, electronic baseline shifts, voltage and pressure fluctuations *etc* .

In the TPC, the measurement of energy loss is an indirect process, involving many steps. An implicit assumption is that the number of free electrons produced per unit track length is proportional to $< dE/dx >$, that is the energy loss, ΔE_i in the ith sample can be estimated as:

$$\Delta E_i = const. \times n_i \tag{4.20}$$

where there are n_i free electrons produced. The constant of proportionality can be deduced from source spectra, or calculated directly. Neither of these methods are entirely satisfactory, therefore one really has to measure the energy loss of a set of known particles in order to set the scale of $< dE/dx >$. Not all the energy lost shows up in the form of free electrons. Some of it shows up

as thermalization and low energy photons, both of which will escape detection in a proportional chamber.

As ionization electrons in the gas drift to the proportional wires, they will diffuse, and some fraction will be absorbed by electronegative impurities, such as O_2, in the gas. For detectors with long drift lengths, like the TPC ($\sim 1\ m$), one must take care to minimize the absorption. In order to reduce the attachment, electronegative impurities in the gas must be kept below 1 ppm. This can be achieved with commercial purifiers, but even with these, some residual attachment remains ($\sim 6\ \%$ over a meter of drift). This can be measured and corrected for on a run by run basis, with a function of the form:

$$n_{corrected} = n_{measured} \times e^{\gamma L} \tag{4.21}$$

where $n_{measured}$ is the number of ionization electrons collected at the sense wires, L is the drift length, and γ is the attachment coefficient. γ had typical values of $0.06\ m^{-1}$.

When the ionization electrons arrive at the sense wire, they produce an avalanche. Only when running at low gains can the actual signal seen at the wire be used as a measure of the number of ionization electrons [51]. Since there is a finite spatial extent to the electron cloud, some electrons will avalanche before others. If the chamber runs at a very high gas gain, the first electrons avalanching will tend to deplete the population of atomic electrons near the wire, making the the late arriving electrons produce smaller avalanches. This can destroy the linearity of the proportional process. At gains above $\sim 10^4$ this effect begins to introduce angle dependent non-linearities [47]. For this reason, and to reduce electrostatic distortions resulting from positive ions drifting into the active volume, the TPC ran at a gas gain of $\sim 10^3$.

The actual pulses seen on the wires are generated by the slow migration of positive ions away from the sense wires. The time structure of the induced signals will show a sharp rise time ($\sim 100\ nsec$) and a long tail. Since the TPC is a multitrack detector, the long tail from the proportional process can cause a substantial baseline shift. For this reason, the TPC amplifiers have a negative feedback built in (time constant $\approx 100\ nsec$) which cancels the long tail, giving a fairly symmetric pulse shape. Even with pulse shaping, one must be careful to eliminate any

residual baseline shifts. In order to avoid pile-up from such shifts, ionization detected on the wires were used for $< dE/dx >$ reconstruction only if there were no other clusters within 3 cm in z. Residual baseline shifts were ≤ 0.5 % with this separation requirement [52].

Fe^{55} source spectra were used to calibrate the TPC wire gain. At the operating pressure and gas mixture, the Fe^{55} spectra show two peaks, a primary peak at 5.9 KeV, and a secondary Auger peak at 3.0 KeV. These spectra were useful because they provided an absolute calibrant of wire gain by depositing a constant number of electrons near a wire.

Fe^{55} source spectra were first used to measure gain variations from wire to wire, and along the length of each wire (*ie* in the η coordinate). Detailed maps of the wire response were made for each wire at 4° intervals for all sectors at the time of construction. These maps, showing typically ~ 3 % variation in response along a wire, were used to correct the pulse height information during track reconstruction. Over the course of the running cycle, source spectra were taken periodically at 3 points along each wire to check for systematic drifts in the response. No evidence of ageing was seen.

Drifts in voltage, gas density and composition were large enough to cause substantial gain shifts (~ 5 %). To achieve the desired resolution, several compensation factors were used to accomodate these fluctuations. The voltage supplies used were capable of maintaining voltages to within ~ 0.2 %. In terms of gain, a 1 % voltage change corresponds to a 18 % change in gain. During the running, the sense wire voltages were monitored, and a pulse height correction factor was used in track reconstruction of the form:

$$PH_{corrected} = PH_{measured} \times \left(\frac{V_{s,m}}{V_{s,o}}\right)^{-17.8} \tag{4.22}$$

where

PH is the pulse height

$V_{s,o}$ is the nominal sense wire voltage (3405 V)

$V_{s,m}$ is the measured sense wire voltage

The exponent was determined empirically.

The density dependence of gain arises because of gas processes near the wire. If the density near the wire goes up, the mean free path goes down, hence the average velocity of electrons between collisions goes down, making the gain drop. Typically, a 1 % change in density implies a 10 % change in gain. A power law correction factor was used to compensate for density changes, of the form:

$$PH_{corrected} = PH_{measured} \times \left(\frac{\rho_m}{\rho_o}\right)^{0.1} \tag{4.23}$$

where

ρ_o is the nominal gas density

ρ_m is the measured gas density

Again, the exponent was determined empirically.

In order to find ρ_m, one must measure both the gas pressure and temperature. Since pressure tends to equilibrate rather quickly throughout a gas volume, only one pressure measurement is necessary, and commercially available pressure transducers were more than adequate to track pressure changes. On the other hand, because of the large thermal mass of various parts of the detector, the temperature varied substantially ($\sim 3^o\ C$) from one part of the TPC to another. It would have been desirable to know the gas temperature directly at the sense wires in order to determine the local gas density, but unfortunately, it was not feasible to do so. An average of the gas inlet temperatures was used as an overall temperature constant. It was also discovered that a temperature gradient of $\sim 2.5^o\ C$ existed between the top and the bottom of the TPC active volume. This, too, was corrected for in determining the gas density at the sense wires.

Despite these corrections, there were still overall gain changes as large as 8 % over the course of as few as 2 days. Fortunately, both the drift velocity, the wires, and independent Fe^{55} monitors in the same gas volume tracked with these gain shifts. Although it is not known with certainty, changes in gas composition are thought to have been responsible for these drifts. The actual fraction of methane, and the level of impurities were never measured directly, but, independent tests indicate that the methane fraction must be kept constant to within 0.2 % for a resulting

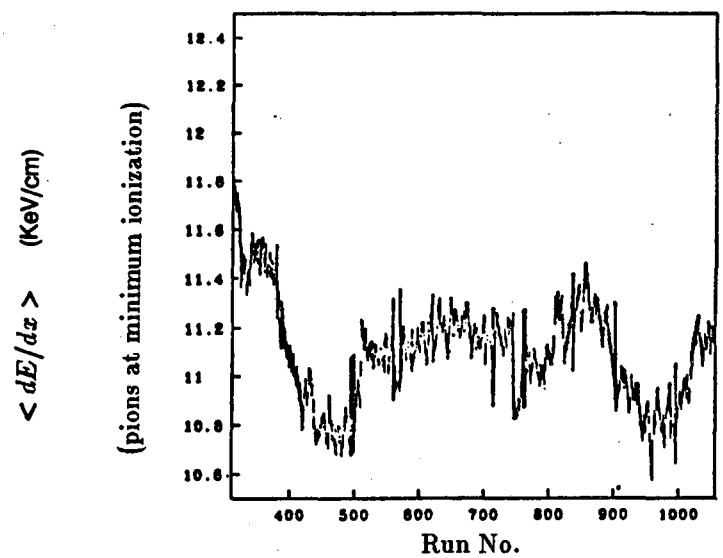

Figure 4.7: Gain shifts as a function of run number for data collected between February 9th and April 10th, 1984. Each run typically lasts 1 hour.

1 % gain stability [53]. Impurity levels can also affect gain, but there are little data on these. Since there were residual shifts in overall gain as large as 8 %, and since one of the putative causes could not be measured, it was necessary to determine directly from charged particle data these overall gain shifts on a run by run basis. For this reason, two passes were made on the entire set of charged particle data. From the first pass, not only was the position of minimum ionization for pions measured, but also a number of other quantities, such as attenuation factors, temperature gradient, *etc* were determined. These constants were then used to correct the data on a second pass in which the overall gain shifts were taken out. Figure 4.7 shows the gain as measured from minimum ionizing pions before corrections as a function of time for part of the data taken in the Spring of 1983.

With the gain correction factors measured and put in, the $< dE/dx >$ resolution for pions at minimum ionization was measured to be $3.6 \pm 0.1\%$ using a Gaussian fit, and requiring at least 80 ionization samples on a track. For wide angle Bhabha electrons with at least 80 ionization samples, the resolution was measured to be 3.1 ± 0.1 % using a fit to a single Gaussian (figure 4.8). The Bhabha sample was analyzed using gain corrections identical to those used on the multi-hadron sample. The difference in resolutions is presumably due to the smaller width of the energy

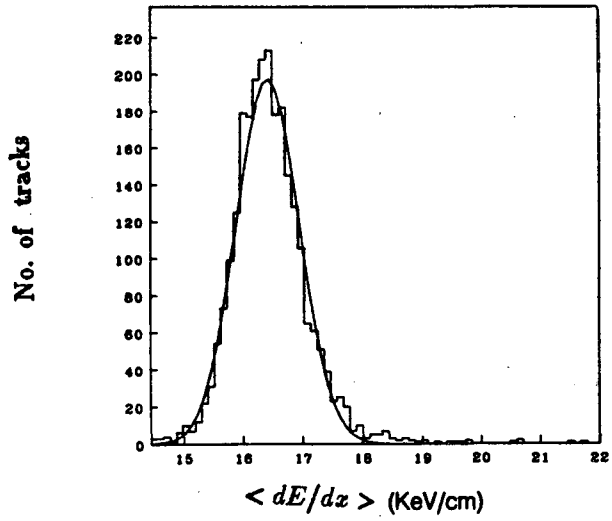

Figure 4.8: Distribution of $< dE/dx >$ for wide angle Bhabha electrons with at least 80 samples of ionization. The line is the result of a fit with a single Gaussian function; the resulting width is 3.1 %.

loss distribution for electrons, because of the larger number of excitations per sample. Figure 4.9 shows a scatter plot of $< dE/dx >$ *vs* apparent momentum for tracks in the multihadron sample (defined in the next chapter) with at least 80 samples of ionization.

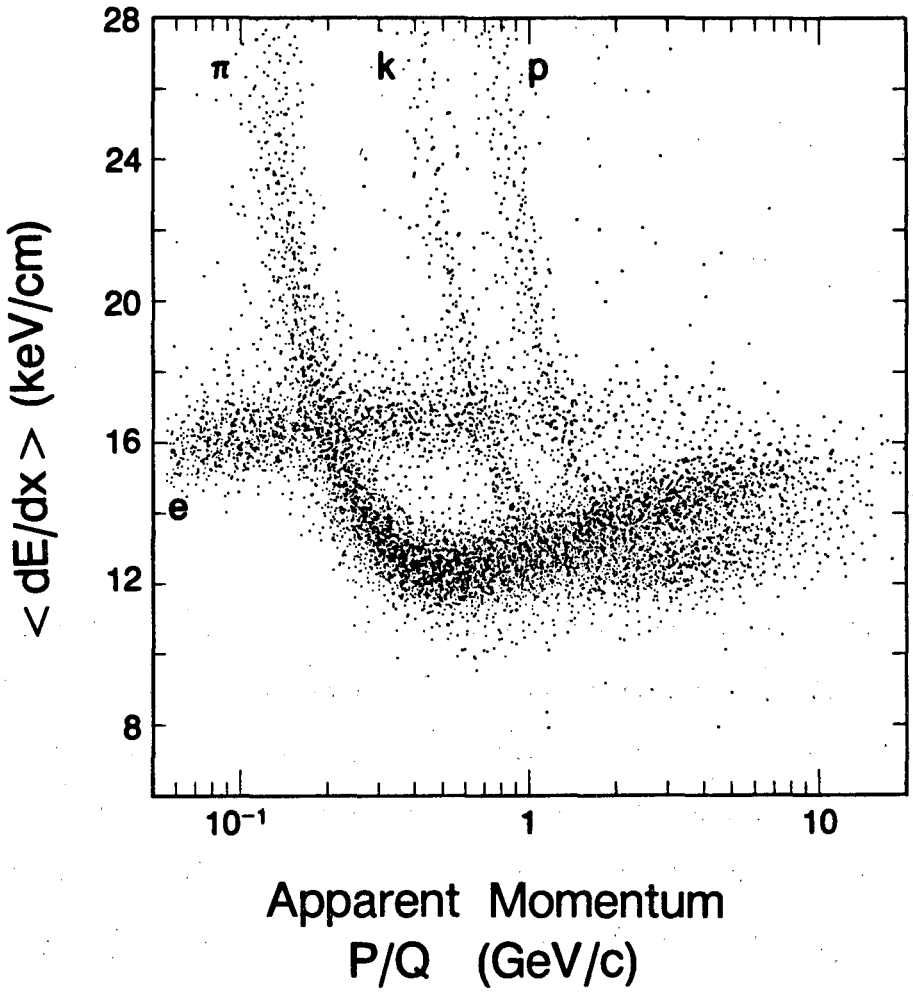

Figure 4.9: Scatter plot of $< dE/dx >$ vs apparent momentum for tracks in multihadron events. Tracks in this plot had to have at least 80 samples of usable ionization. The apparent bands correspond to the ionization curves from the stable $Q = 1e$ particles, e,π,K,μ, and P.

Chapter 5.

Data analysis

5.1. Overview

The data analysis used in the search for free fractionally charged particles is described in this chapter. Here, we are looking for inclusively produced free quarks or diquarks in the reaction $e^+e^- \rightarrow QX$ where Q is the fractionally charged object, and X represents hadrons. As outlined in chapter 3, the technique used to identify fractionally charged particles is a simultaneous measurement of $< dE/dx >$ and momentum. In a plot of these two quantities, the definitive signature for the production of free fractionally charged particles would be the appearance of a band of tracks with the characteristics of an ionization curve, but scaled in $< dE/dx >$ by a factor approximately equal to Q^2 relative to the population of $Q = 1$ tracks. The apparent momenta of these tracks will scale as $1/Q$ relative to the charge-1e population.

Even before starting the search it is reasonable to to expect that the inclusive free quark production in e^+e^- collisions will not be so copious as to generate a solid band of tracks. This expectation is justified in light of previous searches conducted at accelerators, all with null results (see references [4], [6], and [5]), and to a somewhat lesser extent by theoretical expectations that the production cross sections will be suppressed strongly relative to typical hadronic processes [16], [9]. Given the expectation of a low yield, one must then search in regions with almost no background. This means using regions of $< dE/dx >$ and momentum with relatively little or no contamination from the stable ($\gamma c\tau \geq 100\ cm$) charge-1$e$ particles produced in multihadron events. There are two regions meeting this criterion. These are the shaded areas in figure 5.1,

shown with the expected ionization curves for charge-1e and fractionally charged particles. One is at high momentum and high $< dE/dx >$, and the other is at low $< dE/dx >$. In general, the resolutions of $< dE/dx >$ and momentum for the $Q = 1e$ population will determine the actual shapes and positions of the boundaries of the search regions. If these are drawn properly, there should be a negligible contribution from these particles. There are two other boundaries to the search regions; these are imposed by electronic considerations. In principle one could measure pulses almost as small as the noise level, in practice, the thresholds set in the detector electronics will prevent low amplitude pulses from being detected, setting a lower limit on measurable $< dE/dx >$. An upper limit on the measurable $< dE/dx >$ is set by the dynamic range of the electronics.

Even if one succeeds in the above goal, there are still two potential sources of background, both populating the search region at high $< dE/dx >$ and high momentum. The first comes from deuterons and tritons produced in interactions of primary tracks with the detector material. These particles have ionization curves lying partly in the sensitive region, and if produced in large enough quantites, would reduce the sensitivity to fractionally charged particles. The second potential background comes from overlapping track pairs. If two high momentum tracks have a small angular separation, the pattern recognition program sometimes reconstructs only one track. Because the detector cannot distinguish the ionization from two overlapping tracks, the ionization from these will add, and the $< dE/dx >$ for the reconstructed track will be approximately double that for $Q = 1e$ tracks. Since ionization scales as $\sim Q^2$, the overlapping pairs will appear to have a charge of roughly $\sqrt{2}\, e$.

It is possible to reduce this background significantly by applying a set of restrictions to all candidate tracks. Although the restrictions were based on visual scans of candidate tracks, they were made quantitative (ie. based on measurable track parameters) so that the loss of sensitivity due to the restrictions could be measured. Another reason for making the restrictions quantitative was to avoid a potential pit-fall: many searches of this type rejected a substantial number of candidates on the basis of a visual scan. These rejections were probably well justified, but the loss of sensitivity from such a procedure is impossible go quantify.

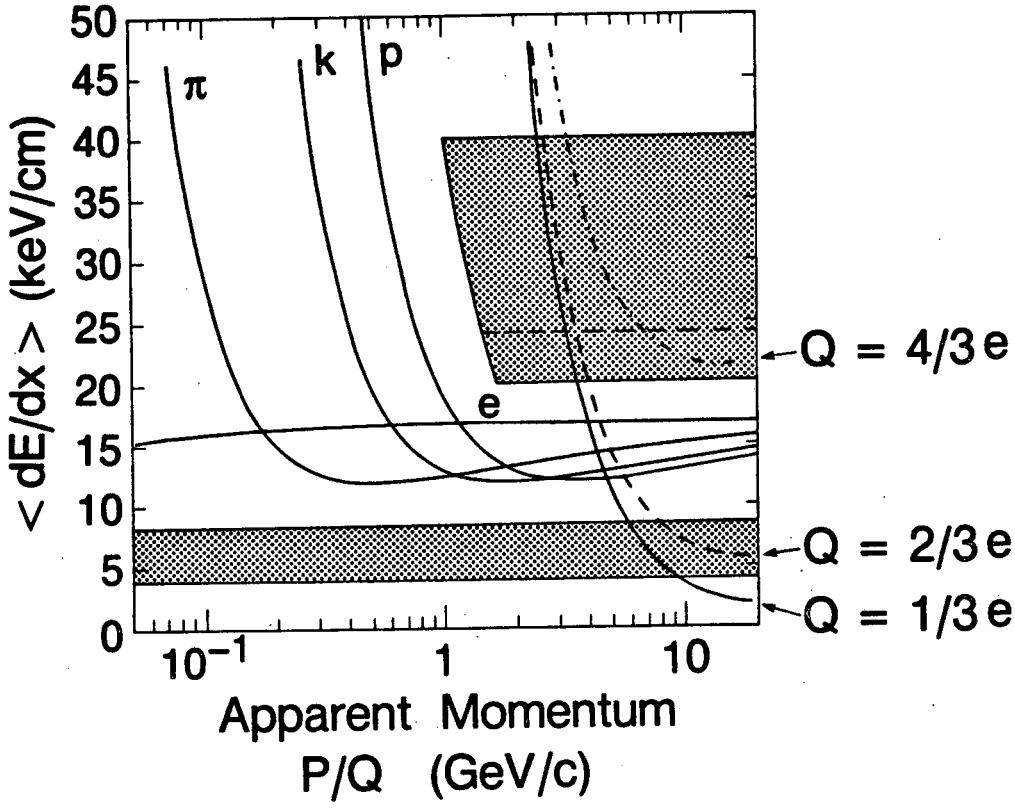

Figure 5.1: Search regions in $< dE/dx >$ and apparent momentum. These are the shaded areas. The ionization curves shown are for the stable $Q = 1e$ particles and for $Q = \frac{1}{3}$, $\frac{2}{3}$, and $\frac{4}{3}e$ particles with masses of 5 GeV/c^2. The search region for $Q = \frac{2}{3}$ and $\frac{1}{3}e$ particles includes the shaded region at low $< dE/dx >$, and the shaded region at high $< dE/dx >$ above the dotted line. The search region for $Q = \frac{4}{3}e$ particles is in the upper shaded region.

In general, when the search regions were defined, or when restrictions were placed on the data, the guiding principle was to reduce the background as much as possible while not significantly reducing the presumed signal. There were a number of ways of testing this maxim, including applying the same restrictions placed on candidates to the known $Q = 1e$ tracks.

The organization of this chapter is as follows, first the limits of the search regions will be defined, based on known resolutions. A preliminary set of cuts will be applied to get a multihadron sample, and candidate tracks will be tagged in this sample. The cuts used to reduce the backgrounds will be described, followed by a discussion of the cross checks used to ensure the validity of these cuts. After this, a discussion of remaining backgrounds will be presented.

5.2. The Search regions

As stated above, the boundaries of the search region are dictated by the detector resolutions in $< dE/dx >$ and momentum, and by the expected population of charge-$1e$ tracks in 77 pb^{-1} of integrated luminosity. A rough estimate of the population of $Q = 1e$ tracks is sufficient to determine where to place these boundaries. In this data sample, there are roughly 30,000 multihadron events at a 29 GeV center of mass energy. In this sample, with an average charged track multiplicity of 11, one expects roughly 300,000 pions. This will help determine where to place the upper boundary of the low $< dE/dx >$ search region. The population of electrons above 1 GeV/c and the population of protons in the $1/\beta^2$ region of the ionization curve will determine the boundaries of the search region in high $< dE/dx >$ and high momentum. One expects approximately 8,000 protons (and anti-protons) in the $1/\beta^2$ region of their ionization curve, and about 3,000 electrons (and positrons) with momenta above 1 GeV/c.

5.2.1. $< dE/dx >$ resolution

A standard requirement for good $< dE/dx >$ resolution is a restriction on the number of wire clusters used in forming the 65 % truncated mean. In this analysis a track is accepted if it has at least 80 good wire clusters along its length. Because of geometric constraints, this requirement

effectively reduces the fiducial volume by making 1.1 $mrad$ the maximum dip angle a track can have. Figure 5.2 shows the number distribution of the number of good wire clusters found on tracks in the multihadron sample. The dotted line represents the predictions of the fast detector simulation, TPCLUND (described in references [37],[55], and in the next chapter). With this restriction, the $< dE/dx >$ resolution is $\sigma_{<dE/dx>} \approx 3.6$ %, measured by fitting a gaussian to pions at minimum ionization. Using electrons from wide angle Bhabha scattered events, one finds a resolution of $\sigma_{<dE/dx>} \approx 3.1\%$. The difference in the resolutions arises because the electrons, being on the relativistic plateau, produce a larger number of primary ionization electrons per unit track length.

If the shape of the $< dE/dx >$ resolution is a Gaussian, one can use the following approximation to estimate the background. Suppose we have a population of N_o tracks of a known species, let us further suppose that they all have the same momentum, hence only one value of $< dE/dx >$ will be the mean. In order to avoid background contamination from this sample, we make a cut on the possible $< dE/dx >$ for tracks of the rare variety:

$$< dE/dx > \geq y_o \tag{5.1}$$

If the mean value of $< dE/dx >$ for the known species is μ, then the number of tracks in this sample expected with $< dE/dx >$ greater than y_o can be estimated as:

$$N = \frac{N_o}{\sqrt{2\pi\sigma^2}} \int_{y_o}^{\infty} exp - \left\{ \frac{(x-\mu)^2}{2\sigma^2} \right\} dx \tag{5.2}$$

If y_o is more than several σ larger than μ then the following expression can be used for the above integral:

$$\frac{1}{\sqrt{2\pi}} \int_{y_o}^{\infty} e^{-x^2} dx \approx \frac{e^{-y_o^2}}{\sqrt{2\pi} y_o} \left(1 - \frac{1}{2y_o^2}\right) \tag{5.3}$$

Figure 5.3 shows the result of a Gaussian fit to the $< dE/dx >$ resolution for wide angle Bhabha electrons. Because of radiative effects, Bhabha electrons are not monoenergetic, but because the $< dE/dx >$ curve is varying slowly with momentum for high energy electrons, these essentially have a constant value of $< dE/dx >$, and are therefore useful to measure the detector response. As one can see, there are longer tails in the distribution than in the fit, this is due

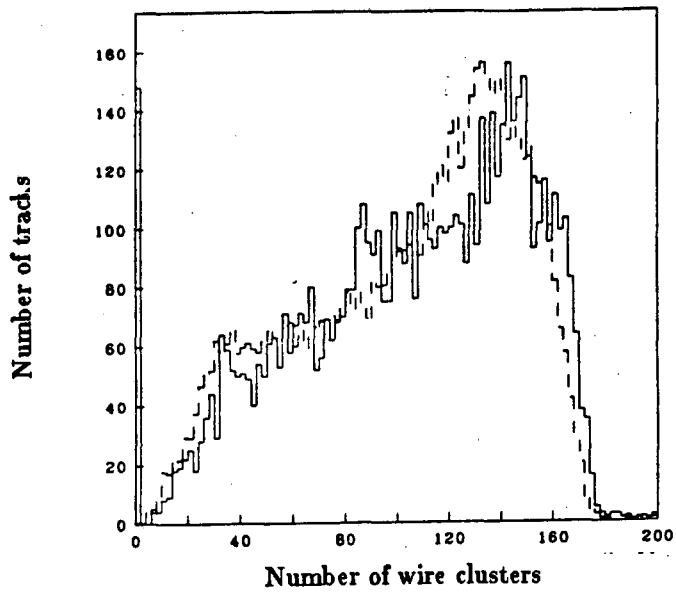

Figure 5.2: Number of tracks showing n wire hits. The dashed line is from the TPCLUND Monte Carlo.

to processes such as the production of very high energy δ rays. To a good approximation, the $< dE/dx >$ resolution function can be represented by the sum of two Gaussians with a common mean value. If the relative population under one of the Gaussians is denoted as f, then the resolution function can be written down as:

$$P(x) = \frac{N_o}{\sqrt{2\pi}} \left(\frac{f}{\sigma_1} exp - \left\{ \frac{(x-\mu)^2}{2\sigma_1^2} \right\} + \frac{(1-f)}{\sigma_2} exp - \left\{ \frac{(x-\mu)^2}{2\sigma_2^1} \right\} \right) \tag{5.4}$$

where σ_1 and σ_2 are the standard deviations of the Gaussians. As will be described in the section on backgrounds, this function gives a good approximation to the tails of the $< dE/dx >$ distribution (see also figure 5.4). A maximum likelihood fit to the $< dE/dx >$ resolution function for wide angle Bhabha electrons with at least 80 good wire clusters gives the following parameters:

$$\mu = 16.4 \pm 0.01$$

$$\sigma_1 = 0.473 \pm 0.007$$

$$\sigma_2 = 1.3 \pm 0.1$$

$$f = 0.93 \pm 0.01$$

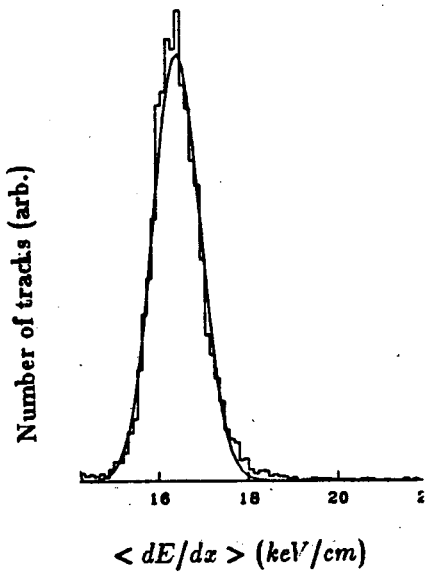

Figure 5.3: Gaussian fit to the $< dE/dx >$ resolution function for wide angle Bhabha electrons. The fit gives a standard deviation of 3.1 %. Note the long tails in the distribution which are not represented by the fitted curve.

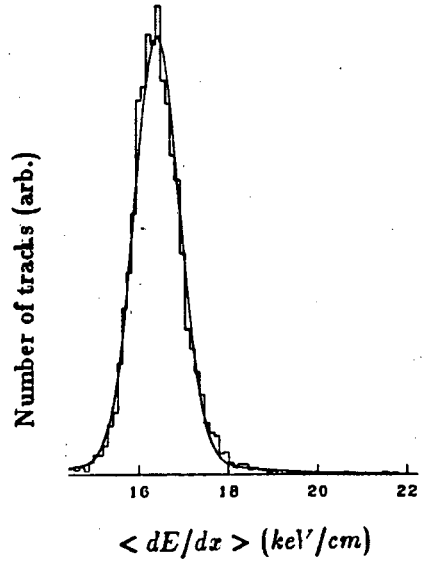

Figure 5.4: A two-Gaussian fit (see parameterization in text) to the $< dE/dx >$ resolution function for wide angle Bhabha electrons and positrons. Note that the long tail is much better approximated by this function.

A fit of the $< dE/dx >$ resolution function for pions at minimum ionization gives:

$$\mu = 12.07 \pm 0.01$$

$$\sigma_1 = 0.44 \pm 0.01$$

$$\sigma_2 = 0.8 \pm 0.1$$

$$f = 0.88 \pm 0.05$$

The largest potential background in the search region at low $< dE/dx >$ comes from $Q = 1e$ particles at minimum ionization. In order to make this negligible, candidates in this region were required to have values of $< dE/dx >$ less than or equal to 8 keV/cm. To a good approximation only the wider Gaussian contributes to the extreme tails of the $< dE/dx >$ resolution function. We can use the above approximation (5.3) to estimate the yield of pions in the sample below 8 keV/cm. It is expected that the contamination should be about 0.005; that is, one would need about 200 times the present statistics to expect with reasonable probability a track with 80 good wire clusters to fall in this region.

The resolution function for the Bhabha electrons will determine where to place the low $< dE/dx >$ boundary of the search region at high ionization and high momentum. For the $Q = \frac{2}{3}e$ and $Q = \frac{1}{3}e$ search, this boundary was set at the line $< dE/dx >= 24$ keV/cm. With this cut, the above approximation gives an expected yield of approximately 1 electron in 1000 times the present sample above the boundary. Placing the cut here gives problems for the $Q = \frac{4}{3}e$ search, however, as minimum ionization for these particles is expected at 21.4 keV/cm. The efficiency for $Q = \frac{4}{3}e$ tracks would be substantially reduced with the boundary here. For this search the lower boundary was chosen at $< dE/dx >$ equal to 1.2 times the value expected for highly relativistic electrons. With the boundary at this value, one expects 0.4 electrons in the given sample in the sensitive region, using the above approximation. The probability of finding at least one electron in this region is 30 %. As it turns out, no candidates were found with $< dE/dx >$ larger than 1.2 times that for electrons which matched the electron hypothesis.

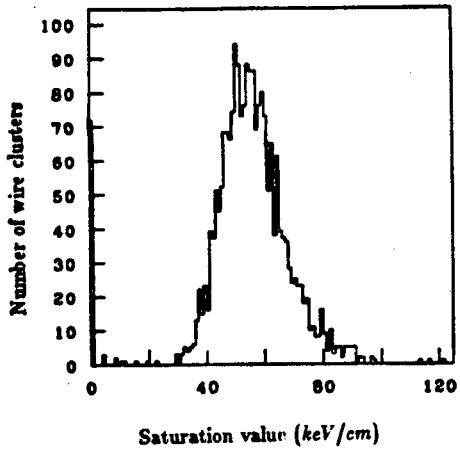

Figure 5.5: Saturation value of wire channels. Units are keV/cm.

5.2.2. Boundaries imposed by electronics

Because of electronic saturation there will be an upper bound to the sensitive region in $< dE/dx >$. In principle, one doesn't have to restrict the range of $< dE/dx >$, for if one found a track which saturated the electronics, yet had a high momentum, it would be clear that this was some particle with an exotic mass and/or charge, but one would have a difficult time making an unambiguous identification of the $< dE/dx >$. If the search region included the saturated region, the calculation of detection efficiencies would be complicated because of the effect of an indeterminate detection efficiency.

In order to avoid this problem, a restriction is placed on the maximum allowed value of $< dE/dx >$ Figure 5.5 shows a plot of the number of channels vs. their saturation in units of keV/cm. As one can see, above 50 keV/cm a significant number of channels are saturated. The restriction $< dE/dx > \leq 40$ keV/cm was chosen as a conservative cut.

Electronic noise and the settings of the digitizer readout thresholds presented a lower limit to the measurable $< dE/dx >$. The setting of the thresholds were typically 10 counts above the pedestal value (noise is about 4 counts RMS). This corresponds, on average, to an ionization $\sim 1/10^{th}$ that of a minimum ionizing $Q = 1e$ track. This is perilously close to the expected minimum ionization for a $Q = \frac{1}{3}e$ particle. Electronic noise will also reduce the position resolution for tracks with low ionization. The track detection efficiency will fall to zero as one approaches the threshold ionization.

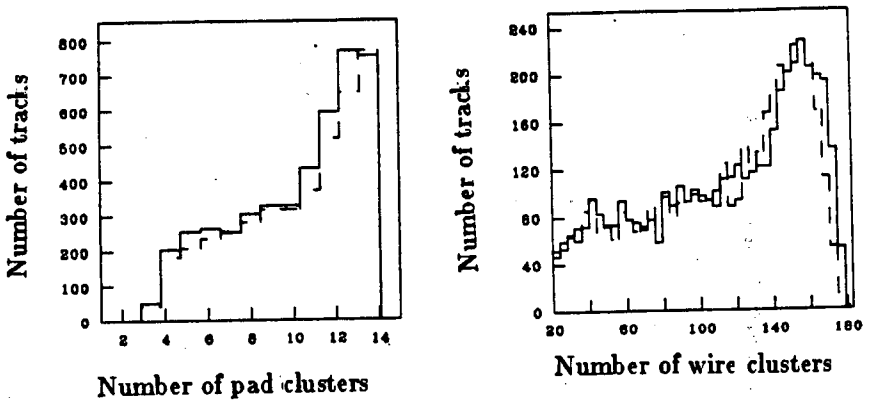

Figure 5.6: Distribution of pad and wire clusters found on tracks in low gain runs. The dashed line is the same distribution taken from normal runs.

In order to estimate the efficiency of tracks with low ionization, several runs were made in June 1983 on beam data with the TPC sector gain reduced by lowering the voltage on the sense wires. Runs were made at $-3300\ V$, and at $-3250\ V$ (nominal value is $3400\ V$). These corresponded to gains of 55 % and 42 % of the nominal operating value. At the reduced gain, the $Q = 1e$ tracks appeared to the signal processing chain past the wires as particles with minimum values of $< dE/dx >$ of 6.9 and 5.8 keV/cm. Unfortunately, time constraints precluded reducing the voltage even further, so an estimate of the loss of the efficiency must be extracted from these data. The results of these runs indicate that although the resolutions drop slightly, the track detection efficiency is reduced by no more than 3 %. Figure 5.6 shows a comparison of the number of pad and wire clusters found on a tracks from data taken on one of the low gain runs, and from the normal data taking. There is no reduction in the number of clusters found on tracks, in fact, there are more good wire clusters found on tracks in the low gain runs because of fewer saturations. Since there was no data was taken at lower gains, a lower limit was set conservatively by choosing 4 keV/cm as the lower boundary of the lower search region. At this value of energy loss it is estimated from extrapolation of the low gain runs that the spatial resolution in the bending plane will be about 300 μm. Figure 5.7 shows a comparison of the ionization spectra of

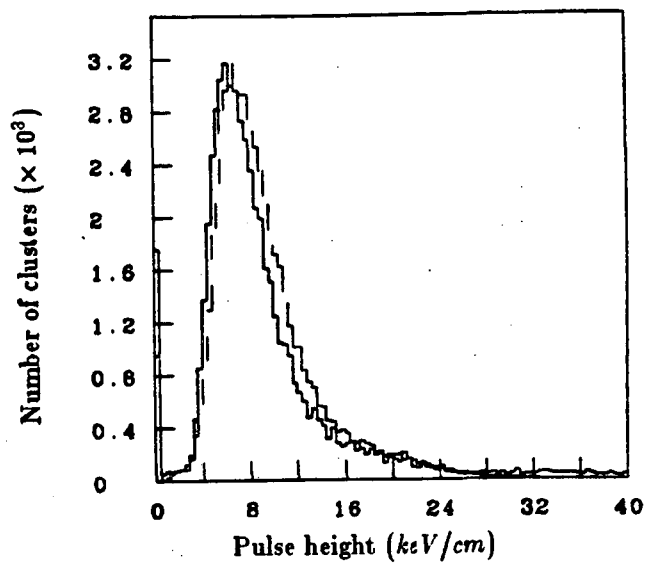

Figure 5.7: Ionization distribution (pulse height spectrum) taken from low gain runs (solid line) and from normal runs (dashed line). The curves are normalized to a common truncated mean $< dE/dx >$.

pions at minimum from normal data and from the low gain runs. The curves are scaled to have the same value of the 65 % truncated mean. The lower edge of the ionization curve will begin to fall below the RAM thresholds for tracks with a $< dE/dx >$ substantially below 4 keV/cm.

One disadvantage of choosing this for a lower boundary is that one is not sensitive to $Q = \frac{1}{3}e$ particles at their minimum ionization. It is certainly possible that one could detect particles with $< dE/dx >$ less than 4 keV/cm, but this would be with an indeterminate efficiency. This boundary is below the value of minimum $< dE/dx >$ for $Q = \frac{2}{3}e$ particles, however, and the detector is sensitive to them here. One also can detect $Q = \frac{1}{3}e$ particles in the $1/\beta^2$ part of their ionization curve in the lower part of this region. Also, as will be shown in Appendix B, the exact choice of the lower boundary of this region doesn't affect the efficiency strongly.

5.2.3. Low Momentum Boundary

So far, only the effect of $< dE/dx >$ resolution on where the boundaries are drawn has been discussed. Since there is a substantial population of charge-1e particles at low momentum and high $< dE/dx >$ in the $1/\beta^2$ part of their ionization curves, we must be careful to draw to low

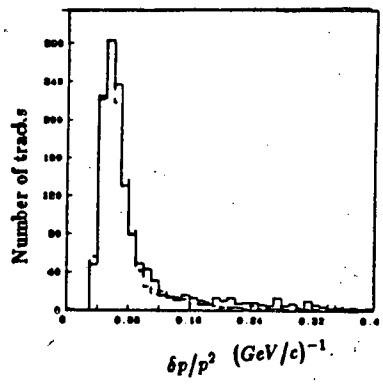

Figure 5.8: Distribution of momentum errors, $\delta p/p^2$ for tracks with momenta greater than 1.5 GeV/c, as determined from residuals to orbit fits. TPCLUND comparison is shown in dotted lines.

momentum boundary of the search region at high $< dE/dx >$ so as to avoid background from poorly fit tracks. The proton population, for which the $1/\beta^2$ part of the ionization curve is at the highest momentum, must be excluded. This consideration will largely determine where this boundary will be drawn. The momentum resolution of the TPC (discussed in chapter 3) is:

$$\frac{\delta p}{p} \approx \sqrt{(0.06)^2 + (0.035p)^2} \tag{5.5}$$

with p measured in GeV/c. For protons at 1 GeV/c ($< dE/dx > \approx 20\ keV/cm$), this implies that $\delta p/p \approx 8\ \%$.

The boundary in momentum was again chosen conservatively to guarantee no contamination from the proton population. This boundary was set at the curve of expected $< dE/dx >$ for a $Q = 1e$ particle with a mass of 1.8 GeV/c^2. It is quite difficult to estimate the "spill over" for this boundary from the protons because the errors in momentum are not Gaussianly distributed (since one is directly measuring the track sagitta, not the radius of curvature). However, one can calculate $\delta p/p$ for each track from the residuals to the fit. For tracks with momenta greater than 1 GeV/c, the error $\delta p/p^2$ is a constant in p. Figure 5.8 shows the $\delta p/p^2$ distribution for tracks with momenta greater than 1.5 GeV/c. Due to multiple scattering, tracks with momenta substantially less than 1 GeV/c will have much larger values of $\delta p/p^2$. As outlined in appendix A, the expression for $\delta p/p^2$ at high momenta is identical for particles with a charge other than 1e if one substitutes apparent momentum, p/Q for p above.

A way of keeping the proton background down to a negligible level is to make a restriction on $\delta p/p^2$; this will reduce the effect of the tail of this distribution. A standard requirement placed on candidates in the search region at high $< dE/dx >$ is to accept tracks with momentum errors $\delta p/p^2 \leq 0.1$. This effectively reduces to nothing the contribution of protons to a background signal in the search region at high $< dE/dx >$.

To summarize the boundaries of the search regions in $< dE/dx >$ and momentum are chosen so that the high $< dE/dx >$ boundary of the upper region at 40 keV/cm, the $< dE/dx >$ boundary set at 24 keV/cm for the $Q = \frac{2}{3}, \frac{1}{3}e$ search, and at $< dE/dx >= 1.2$ times the $< dE/dx >$ expected for electrons on the relativistic plateau for the $Q = \frac{4}{3}e$ search. The low momentum boundary of this region is defined by the curve of $< dE/dx >$ expected for a 1.8 GeV/c^2 charge-1e particle. The high $< dE/dx >$ boundary of the lower search region is set at $< dE/dx >= 8keV/cm$, the low $< dE/dx >$ boundary of this region is set at $4keV/cm$.

5.3. Multihadron Event Selection

The inclusive search is for free fractionally charged particles in the reaction $e^+e^- \rightarrow \gamma^* \rightarrow QX$, where $X = hadrons$ and Q is the exotic particle. Limits on the inclusive production cross section for fractionally charged particles are usually quoted in terms of $\sigma(e^+e^- \rightarrow Q\overline{Q}X)$, because charge conservation requires a fractional charge balance in the event. In this search, one is looking only for a single free quark (or diquark) in a multihadron event.

The multihadron selection criteria used here were very similar to those used in almost all e^+e^- experiments at these energies. A useful definition in describing these criteria is whether or not a track comes from the beam-beam crossing point; this will be referred to as beam associated. A track is beam associated if its distance of closest approach to the beam-beam crossing point in the (r, ϕ) plane is less than or equal to 5 cm and if the distance of closest approach in z is less than or equal to 10 cm. The beam profile has a horizontal width of 500 μm and a vertical width of 50 μm.

From the preanalyzed data tapes described in the previous chapter, multihadron events were

Source	% Contamination
$\tau\bar{\tau}$	3.2
$2\,\gamma$	2.0
Beam Gas	0.5
Cosmic Ray	2.5

Table 5.1: % contamination of the multihadron sample from various background sources.

selected if they satisfied the following criteria:

1. The event contains at least 5 beam associated tracks.
2. The scalar sum of the momenta of the charged particles in the event must be greater than or equal to half the beam momentum (*ie.* $\sum |p| \geq 7.25 GeV/c$).
3. The forward-backward energy imbalance, $\sum p_z / \sum |p|$ must be less than or equal to 0.4.

The object of these selection criteria is to reduce as much as possible the contamination from cosmic rays, $\tau\bar{\tau}$, $\mu^+\mu^-$,Bhabha, 2 photon and beam gas events. The restriction of 5 or more tracks is set because of the background from τ decays involving 4 charged particles in the final state. The second and third requirements reduce the contribution of beam gas and 2 photon events by requiring a symmetric (with respect to z) topology of the final state particles, and some minimum energy.

With these cuts there is $\sim$ 8 % contamination from these backgrounds. Table 5.1 shows the breakdown of the sources of background (for details, see references [37] and [43]). In the 77 pb^{-1} of integrated luminosity collected, 29,094 events passed these criteria. Studies with TPCLUND indicate that these criteria accept $\sim$ 80 % of all multihadron events.

5.4. Candidate selection at low dE/dx

A preliminary selection was made of events with tracks in the low $< dE/dx >$ search region. Events were selected from the multihadron sample if they had a beam associated track with at least 80 good wire clusters and a $< dE/dx >$ greater than or equal to 4 keV/cm and less than or equal to 8 keV/cm. Ten candidate events satisfied these criteria. A visual scan of the candidate

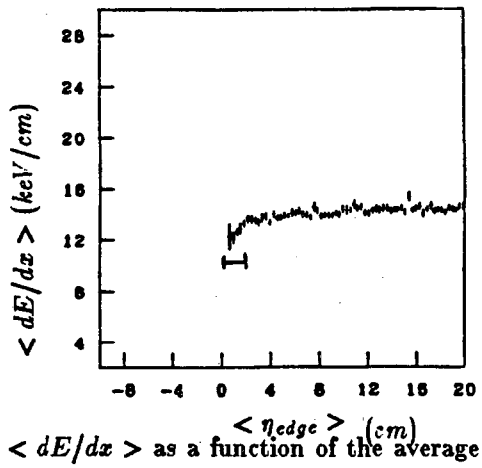

Figure 5.9: Average value of $< dE/dx >$ as a function of the average distance from the sector edge, $< \eta_{edge} >$.

tracks in this sample showed that they bordered the edge of the sectors which they were detected in.

Both the momentum resolution and the the gain of the TPC sectors drop rapidly within 2 cm of the edge. A reasonable requirement, then, is to require particles to be detected well away from this region. In order to quantify this, a measure was devised of how close a track came to the sector edge. Each pad hit has an η coordinate, η_i. For the pad row on which the hit was detected one also has a maximum allowed value of η, η_{max}, dictated by the sector geometry. For N pad hits, the average distance of all the pad hits on a track from the edge of the sector is given by:

$$< \eta_{edge} > \equiv \frac{1}{N}\sum_{i=1}^{N}(|\eta_i| - |\eta_{max}|) \tag{5.6}$$

If one plots (as in figure 5.9) the average value of $< dE/dx >$ as a function of $< \eta_{edge} >$, one finds that $< dE/dx >$ drops off for $< \eta_{edge} > \leq 2\ cm$. Clearly these tracks appeared in the sample because they lay right along the edge of the sector. A restriction was made that $< \eta_{edge} > \geq 2\ cm$ for all tracks in the data sample. After imposing this restriction, no candidate tracks remained in the data sample of low $< dE/dx >$.

As a check of the expected background from $Q = 1e$ tracks at minimum ionization, the high $< dE/dx >$ boundary of this region was raised to 9 keV/cm. Using the approximation to the $< dE/dx >$ resolution function described earlier, it is easy to show that one expects ~ 5 tracks in this region. Three tracks were actually found in this area, which is consistent with an estimate

of five.

5.5. Search region at high dE/dx and momenta

Candidate events in the multihadron sample were selected if they had a beam associated track with at least 80 good wire clusters, and a $< dE/dx >$ and momentum falling in the upper sensitive region. In addition, the momentum error, $\delta p/p^2$, for candidates in this region had to be less than or equal to 10 % (p measured in GeV/c). Because of problems in estimating δp for tracks near the edge of the sectors, a cut was made on $< \eta_{edge} >$ identical to the one discussed above ($< \eta_{edge} > \leq 2\ cm$).

The requirement that a track be beam associated helped reduce the background from deuterons produced in the beam pipe or in the detector itself. Because of finite production angles, nuclear secondaries produced in the detector will usually not extrapolate, within errors, through the beam-beam crossing point. This will be discussed in detail later.

In the $Q = \frac{4}{3}e$ search region, 132 candidates passed these criteria. 92 candidates passed these criteria in the upper $Q = \frac{1}{3}, \frac{2}{3}e$ search region. Figure 5.10 shows a scatter plot of these candidates in $< dE/dx >$ vs momentum. No clear band of ionization stands out to the eye.

There were two possible sources of background in this region. As mentioned above, deuterons can populate this region, but if these were deuterons, the candidates would tend to crowd the low momentum boundary, which is not seen. Since deuterons arise mainly from interactions in the detector, one would expect that if these were deuterons, they would be positively charged. There are roughly equal numbers of positively and negatively charged tracks in the sample, indicating that this is not the case. The second possible background arose from overlapping track pairs which were reconstructed as single tracks. This, as it turned out, was the largest source of these tracks.

5.5.1. Pad restrictions

A subset of these tracks (~ 50) was scanned visually to see if they possessed any unusual

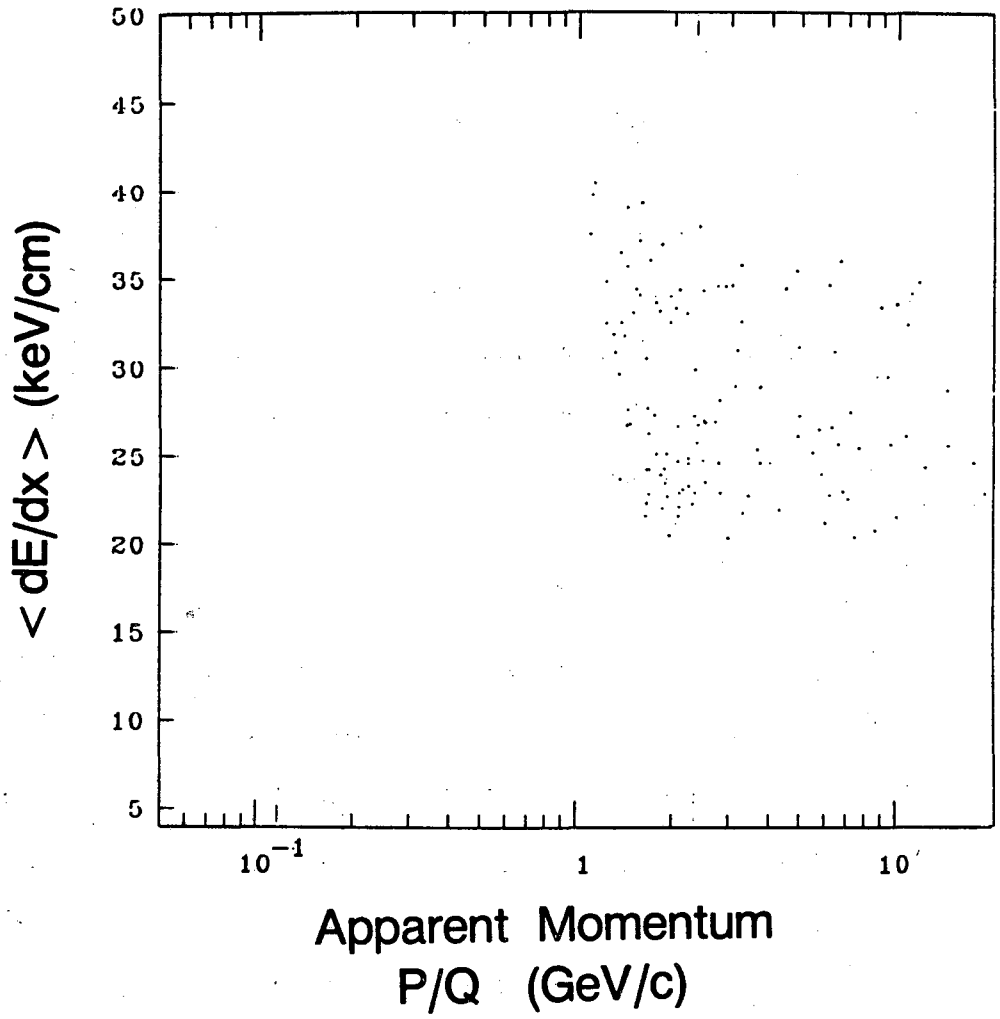

Figure 5.10: Scatter plot of candidates in the search region at high $< dE/dx >$ and momenta.

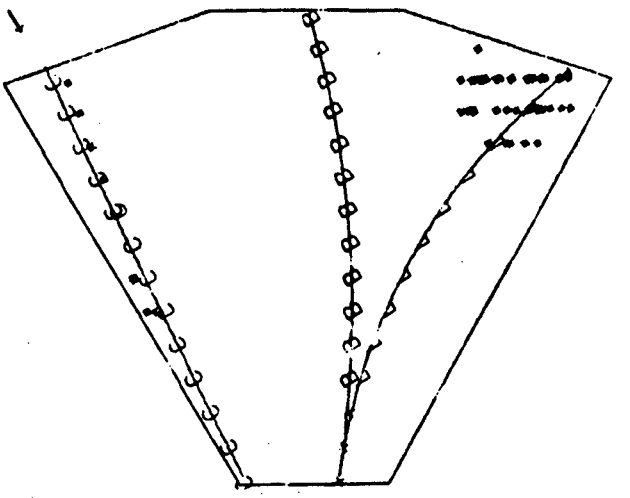

Figure 5.11: Overlapping track pair taken from the data sample.

characteristics indicative of the backgrounds described above. A close inspection of many of these candidates revealed characteristics which were very suggestive of overlapping track pairs. Figure 5.11 shows the pad clusters from such a candidate. The track is labeled G in the figure. One can plainly see next to the track the presence of pad hits (denoted by stars) not associated with a known track, yet indicative of a second track not detected by the pattern recognition program. Figure 5.12 shows the resultant pad clusters and fit when two tracks are generated with an angular separation of 10 *mrad* in the GLOBAL detector simulation. The GLOBAL simulation [37] was a very detailed, CPU intensive program, which emulated the physical processes of the detector response to both charged and neutral particles. The output of GLOBAL was in the same format as the raw TPC data. The raw data provided by the simulation could then be processed in the same way as the TPC data was processed. The similarities between the overlapping track pair produced by GLOBAL, and the track in figure 5.11 are striking.

The pad information can be used to reduce this background. We require candidates to have pad widths consistent with a single track, and require them to not have a large number of unidentified pad clusters nearby. Because of the nearby pad hits, it is apparent that the track in figure 5.11 is not a *bona fide* candidate, but really a pair of overlapping tracks which were reconstructed as one. This can be quantified by asking how many pad clusters not associated

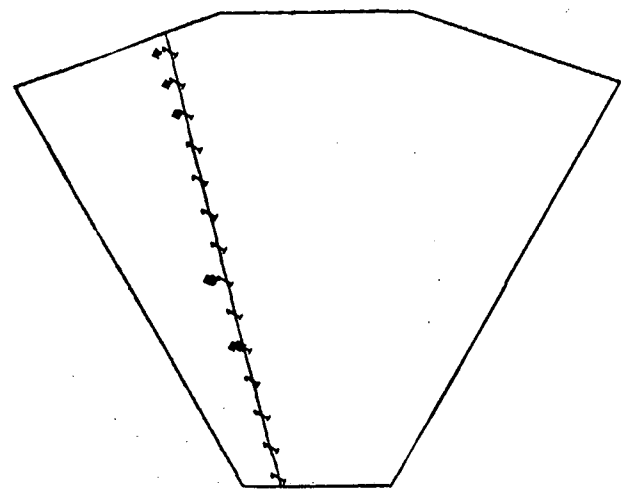

Figure 5.12: Overlapping track pair generated by the detailed detector simulation, GLOBAL [37].

with fitted tracks fall within 3 cm in z and η of a track; this number will be referred to as n_{pad}. The distribution of n_{pad} is shown in figure 5.13. The solid line is the distribution seen for candidate tracks, the dashed line is the distribution seen for normal $Q = 1e$ tracks in the multihadron sample (here the normalization is such that the highest bins in each histogram are made the same height). The tracks in the upper sensitive region have a significantly larger number of nearby pad hits than those found near normal $Q = 1e$ tracks.

In order to reject a large fraction of the overlapping track pairs as candidates, all candidates were required to have fewer than 3 nearby pad hits not associated with a known track (ie. $n_{pad} \leq 3$). This requirement eliminated 66 of the 132 candidate tracks passing the preliminary criteria. From figure 5.13, one can see that this restriction does not reduce significantly the $Q = 1e$ population. As an estimate of the inefficiency incurred by using this restriction, the same requirement was placed on heavily ionizing ($< dE/dx > \geq 20\ keV/cm$) $Q = 1e$ tracks. This reduced the $Q = 1e$ population by 4 %.

Because of the loss of position resolution near the edge of the TPC sectors, it is possible for a track to register wire and pad hits bordering the edge of the sector, and yet not be reconstructed by the pattern recognition program. If another track has approximately the same z coordinates

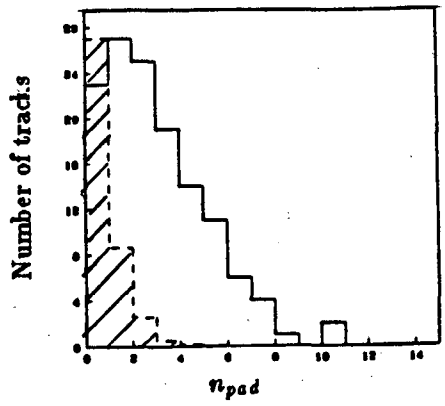

Figure 5.13: Distribution of the number of close pad hits not associated with fitted tracks for all data (under hatched) and for the tracks in the upper sensitive region. The distributions are normalized such that the tallest bins in each distribution have the same height.

as the undetected track on the edge of the sector, the wire clusters from these two will merge, giving a track with twice the $< dE/dx >$ of a $Q = 1e$ particle. An example of this is shown in figure 5.14, with the hits from the undetected track faling along the edge of the sector. In order to eliminate this background, a cut on the number of nearby non-track associated pad hits was made, similar to the one used above on n_{pad}. A candidate was rejected if it had 4 or more pad clusters not associated with an identified track, and located within 3 cm in z of the track. The only substantial difference between these two cuts is that in this case, the restriction on the proximity of the pad clusters in η has been dropped. This cut eliminated 36 (out of 132) candidates. Again, the inefficiency this criterion introduced was estimated by applying the same cut to the heavily ionizing $Q = 1e$ tracks. This cut reduced the efficiency by less than 0.5 %.

Another means of reducing the background caused by overlaping track pairs is the cluster width information. When the clusters from two tracks merge together, the resulting clusters are wider than those found for normal tracks. A reasonable requirement is that all candidates have ionization cluster widths consistent with a single track.

The ionization clusters imaged on three pads provided a way of measuring the width of the ionization clusters. One can fit a Gaussian to these three pad clusters, deriving a width, σ_{pad}, which is typically 3.9 mm for normal tracks. Figure 5.15 shows the distribution of pad widths for three pad clusters from $Q = 1e$ tracks in the multihadron sample. The pad information is

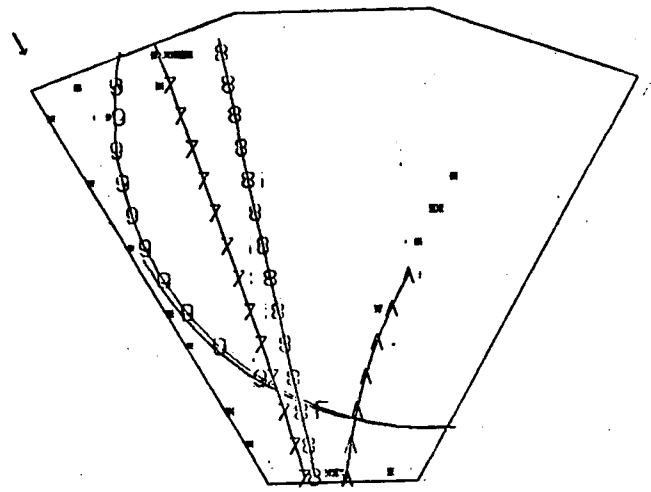

Figure 5.14: Undetected track bordering the sector edge.

unfortunately rather sparse, with 2 to 10 pad clusters with measurable σ_{pad}'s found per track. The distribution of the number, N, of three pad clusters per track is quite broad.

As a measure of the overall width for any given track, one could average the cluster widths, but this is a crude measure, especially with as few as two 3 pad clusters per track. A more efficient way is to use the likelihood measure. From the width distribution shown in figure 5.15, one can make a probability function, $\mathcal{P}(\sigma_{pad})$, representing the probability of finding a width σ_{pad} on a three pad cluster on a single track. From this one can write, for N three pad clusters, the likelihood function, $\mathcal{L}(N, \mathcal{P})$, as:

$$\mathcal{L} \equiv \left(\prod_{i=1}^{N} \mathcal{P}(\sigma_i) \right)^{\frac{1}{N}} \tag{5.7}$$

It is usually more convenient to work with the log of this function, so we define the log-likelihood, L, as:

$$L \equiv ln(\mathcal{L}) = \frac{1}{N} \sum_{i=1}^{N} ln(\mathcal{P}(\sigma_i)) \tag{5.8}$$

Qualitatively, L will be a negative number because one is taking the logarithm of a probability. Tracks with high likelihoods (*ie.* widths consistent with a single track) have values of L close to 0, while tracks with low likelihoods have large negative values of L.

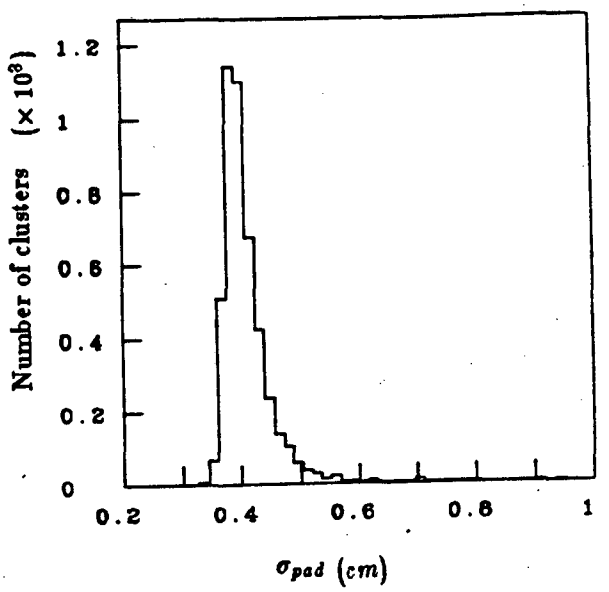

Figure 5.15: Distribution of pad widths found on tracks in the multihadron sample.

It is reasonable to normalize with $1/N$. Suppose the probability of finding a particular width, σ_o is P_o. Suppose further that there are two tracks, one with 2 hits of width σ_o, and one with 10 hits of width σ_o. Since the hits have the same width for both tracks, one would naively expect that the likelihood for these two should be the same; the normalization by $1/N$ guarantees this. A Monte Carlo calculation was made to demonstrate the validity of the $1/N$ normalization. Pad hits were chosen with widths chosen using the distribution $P(\sigma_o)$. A "track" was simulated by getting N from the distribution of N three pad hits per track. From these N three pad hits, a likelihood distribution was generated. The distribution giving N was altered severely to see how the resulting likelihood function varied. As it turned out, the shape of the N distribution had a negligible effect on L. It should also be pointed out that the width distribution, and hence L is independent of the value of $< dE/dx >$ for a track. This is because the width is largely determined by the transverse diffusion of the primary ionization electrons, and not on the actual number of these; the number of three pad solutions, however, does show a mild $< dE/dx >$ dependence, although this doesn't affect the likelihood distribution.

The distribution of L is shown in figure 5.16 for singly ionizing tracks in the multihadron sample. The liklihood distribution for candidate tracks passing the preliminary criteria is shown by the solid line. Of obvious importance is the fact that the tracks in the sensitive region have

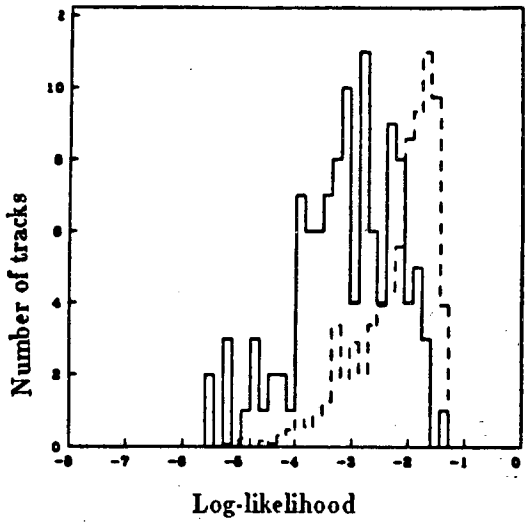

Figure 5.16: Likelihood distribution of normal tracks (dashed line) and for tracks in the sensitive region (solid line).

much lower values of L than the $Q = 1e$ tracks in the multihadron sample. The candidate tracks have a substantially different distribution of L than normal data tracks, indicating that most tracks in the upper search region have pad widths which are not consistent with a single track. The detector simulation, GLOBAL [37] was used to check this. Relativistic $Q = 1e$ track pairs were generated at small angular separations, and were found, not surprisingly, to give rise to single tracks in the search region. The distribution of L (figure 5.17) for single tracks from GLOBAL match well the distribution of L from the $Q = 1e$ tracks. In addition, the distribution of L's from the overlapping GLOBAL tracks also matches the distribution of L from tracks found in the upper search region.

Low values of L were used as a criterion for rejecting overlapping track pairs in the sensitive region. Candidate tracks were required to have values of L greater than or equal to -3.45. This restriction eliminated 52 (out of 132) candidates, representing a reduction of 39 % in the number of tracks in the sensitive region. The same cut placed on heavily ionizing $Q = 1e$ tracks, reduced this control sample by less than 2 %.

The use of the pad width information in scanning events revealed an interesting feature. Overlapping track pairs from the decays of neutral hadrons, and from photon conversions show

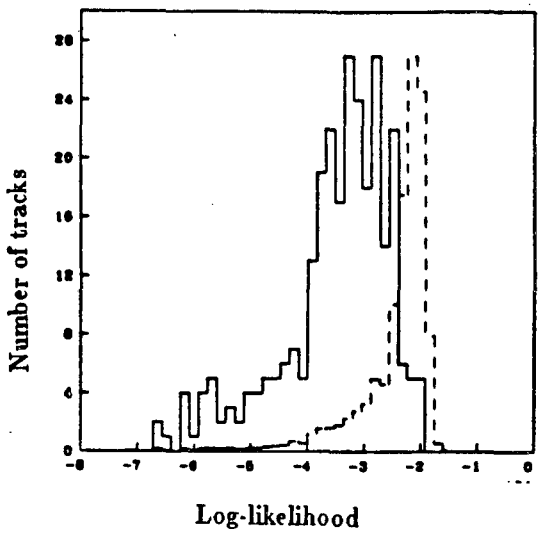

Figure 5.17: Likelihood distribution for single tracks (dashed line), and for overlapping track pairs (solid line) generated by the detector simulation GLOBAL [37].

pad clusters which get wider at pad rows at larger values of ξ. A particularly good example is shown in figure 5.18, with the candidate track indicated by the arrow. This is probably a photon conversion in the TPC inner radius field cage, as evidenced by the absence of a hit in the IDC. Note also the large electromagnetic shower in the HEX calorimeter module. This shower had full beam energy, and is consistent with an e^+e^- pair showering. A plot of the pad cluster widths as a function of ξ is shown in figure 5.19. This is what one might expect from a pair of oppositely charged tracks at very close angular separation. This event was rejected by the likelihood requirements, but illustrates that most candidates had many characteristics indicative of overlapping track pairs besides the quantities used in the formalized restrictions.

If one takes the two track overlap cuts using the pad information in conjunction, 103 (out of 132) of the candidate tracks in the sensitive region were eliminated. The same restrictions in conjunction eliminated only 8 % of the tracks in the control sample of heavily ionizing $Q = 1e$ tracks.

5.5.2. Wire restrictions

So far only pad information has been used to examine the background from overlapping

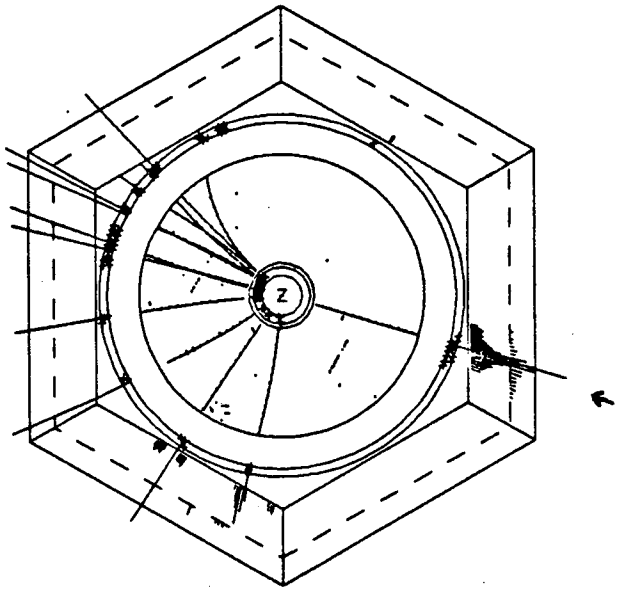

Figure 5.18: Event with track in the upper search region. The arrow indicates the candidate track, actually a conversion pair reconstructed as a single track.

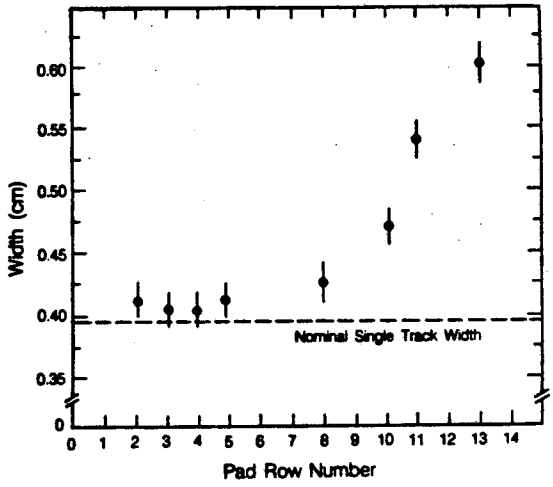

Figure 5.19: The pad width as a function of pad row number of the candidate track shown in figure 5.18.

track pairs. With up to 183 wire clusters possible along a track length, it is possible to sort out overlaps. The wire information was not only useful in eliminating overlapping tracks, but also in eliminating backgrounds due to "soft" process, such as the production of high energy δ rays.

Again, one can use the cluster width information to reduce the background from overlapping track pairs. From fits to the wire clusters, it is possible to get an estimate of the z width. Unlike the pad clusters in η, the z cluster resolution function is really a convolution of a) the arrival time of the ionization, b) the time development of the avalanche and subsequent positive ion migration at the sense wire, and c) the shaping response of the preamplifier-amplifier combination. Only a) is an estimator of the true width of the ionization cluster, the other effects only act to smear out a).

Figure 5.20 shows the distribution of the wire cluster z widths from the $Q = 1e$ sample. The most probable value is $\sim 1.6\ cm$, but there is a relatively long tail at the high end. The long tail arises because of processes such as hard δ ray production which tends to spread out track ionization over relatively large distances. The production of stiff δ rays in fact constituted a subset of the overlapping track pairs. The kinematic limit for δ ray production is $\Delta E \approx 2m_e\beta^2\gamma^2$. For tracks with momenta of 1-15 GeV/c this implies that δ rays with an energy on the order of several hundred MeV can be produced. These δ rays can be so stiff that they can merge with the primary track, producing localized regions with greater than double the ionization for a minimum ionizing track.

Since the wire z cluster measurement is relatively crude, the large number of wire clusters were relied upon to gain in analyzing power. From the distribution in figure 5.20, a wire cluster is termed "wide" if the width is greater than 1.8 cm. Figure 5.21 shows the distribution of the number of wide hits on $Q = 1e$ tracks. Note that the most probable value is non-zero, indicating that the emission of a δ ray on tracks is quite likely. The solid line show the same distribution for tracks passing the preliminary cuts in the sensitive region. One sees that tracks in the sensitive region have many more wide z wire clusters than the control sample. This distribution served as the basis for another restriction on candidate tracks. All candidate tracks were required to have

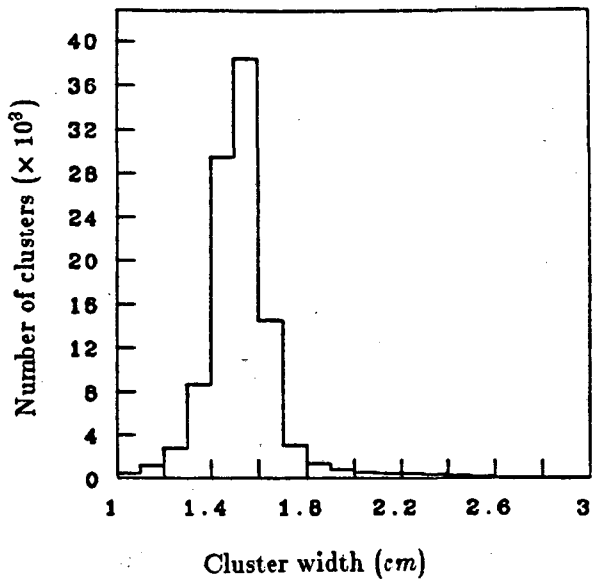

Figure 5.20: Distribution of wire z cluster widths for normal tracks in the data.

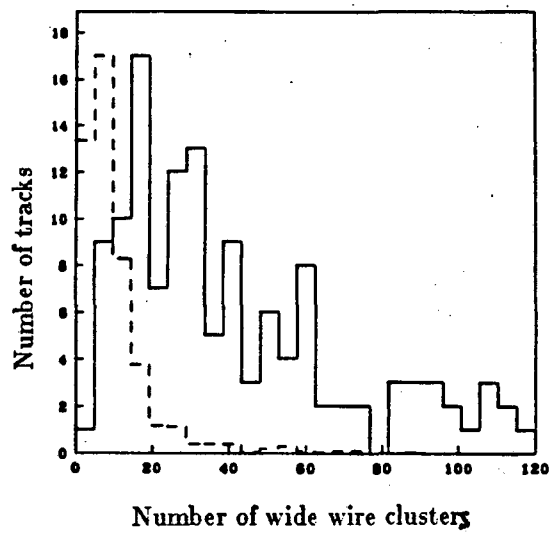

Figure 5.21: Distribution of the number of wide z wire clusters of normal tracks (dashed line) and for tracks found in the sensitive region (solid line).

fewer than 20 wide wire clusters along the track length. This cut eliminated 95 (of 132) tracks in the search region at high $< dE/dx >$, but eliminated only 8 % of the control sample.

A variation of this cut was used to help eliminate tracks with high energy δ rays. The restriction was based on the assumption that this kind of process produces large localized deposits of ionization Put another way: candidate tracks were required to have a statistically uniform distribution of pulse heights and widths along a track length. Figure 5.22 shows a candidate track with some of these characteristics. There seem to be two disturbances along the track length, associated with appears to be secondary particles emitted by the primary particle. A simultaneous plot of ionization vs. wire number and cluster width vs. wire number sheds some light on this. The wire width plot shows that the disturbances are associated with regions of wide z width. As one can see, a region of high ionization begins at the first disturbance and ends at the second disturbance. A possible interpretation of this event is that a photon converted at the first disturbance creating one soft e^+ and one hard e^-. The hard electron apparently merged with the primary track for some of its length, producing a localized region of heavy ionization. Figure 5.23 shows a simultaneous pair of plots of ionization and z width as a function of wire number for another another track from the sensitive region. Note that the large deposition of ionization is localized and correlated in wire number with the wide wireclusters. This track was found with a $< dE/dx >$ close to the lower boundary of the search region, indicating perhaps that the primary track was an electron. Here we come to a case where the meaning of $< dE/dx >$ becomes somewhat fuzzy, because strictly speaking, this sort of process is an energy loss mechanism, which is partly responsible for the long non-Gaussian tails of the $< dE/dx >$ resolution function.

For most of these tracks, if one computed the truncated mean excluding the the wide z clusters, the candidates showing this sort of process would show a $< dE/dx >$ consistent with that for an electron. Tracks were excluded from consideration as candidates if they showed a correlation on many wires between regions of high ionization and large cluster widths. This was quantified as follows: a track was rejected if there were 12 or more wide wire hits with greater than 1.3 times the average ionization for the entire track. This restriction eliminated 39 (of 132) tracks in the sensitive region, while rejecting only 5 % of the control sample of heavily ionizing

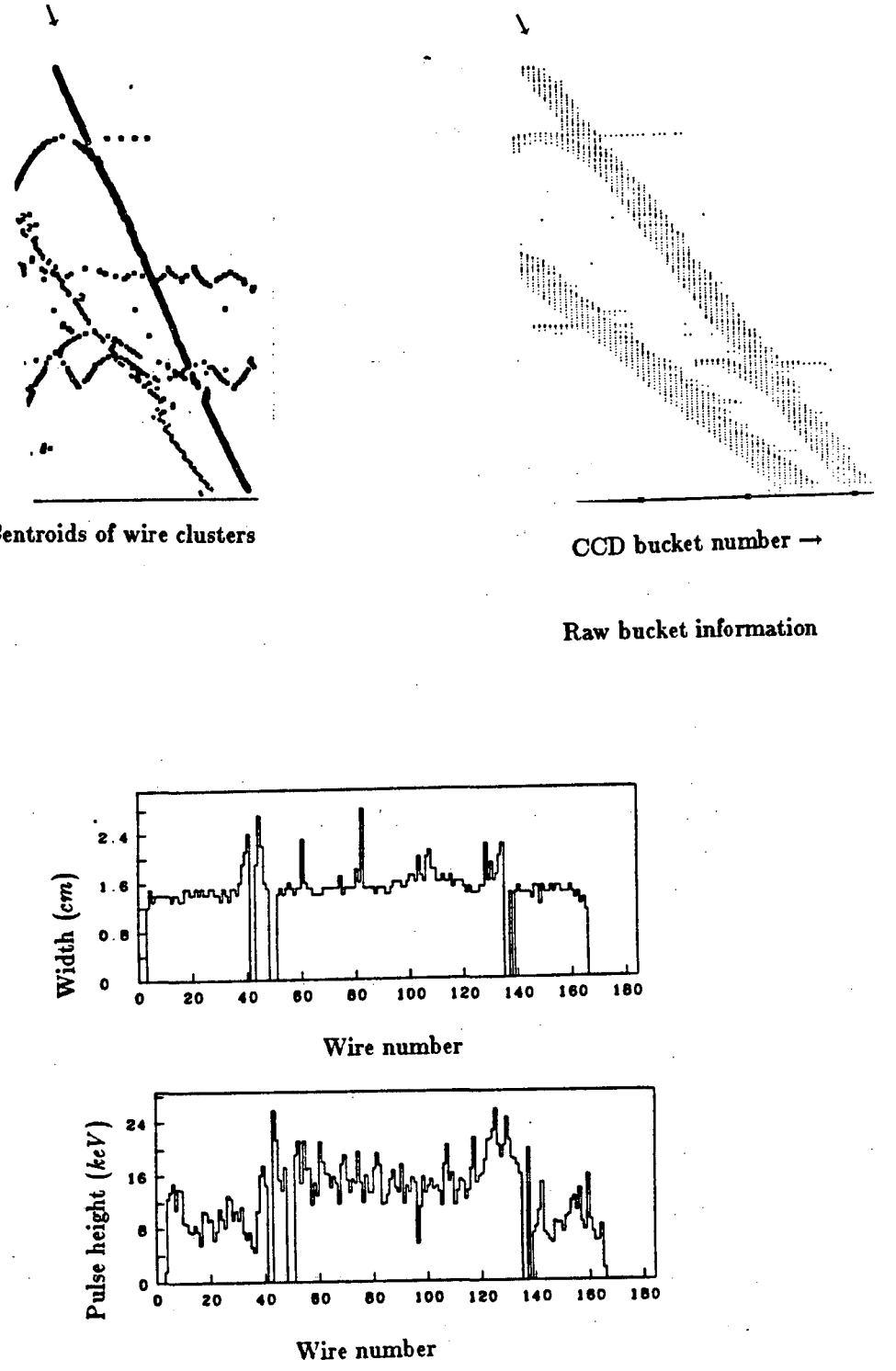

Figure 5.22: A candidate track showing localized production of secondaries. A plot of the centroid of the wire clusters (upper left) shows two tracks associated with the primary (arrow). The raw CCD bucket information (upper right) also shows these secondaries. In a plot of wire cluster width as a function of wire number, the points where the secondaries originate are associated with abnormally wide hits. In a plot of ionization as a function of wire number, the region between the two production points has twice the ionization of a single $Q = 1e$ particle.

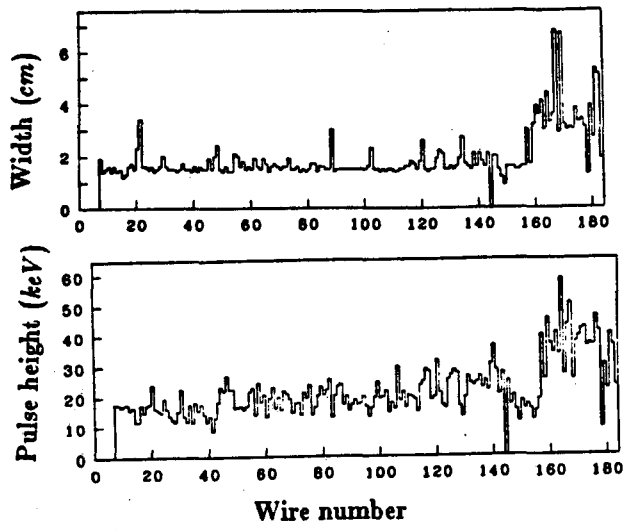

Figure 5.23: A simultaneous plot of wire cluster width and ionization vs wire number for a track in the sensitive region. Note the correlated deposition of energy and wide z width.

$Q = 1e$ tracks.

These cuts reduce the background from overlapping track pairs, particularly in the case of "soft" processes such as δ ray production. As a cross check of the validity of these wire cuts and the hypothesis that they tended to reject tracks with stiff δ rays, the same restrictions were made on a sample of Bhabha electrons. The Bhabha tracks were selected by looking for wide angle back to back electromagnetic showers in the HEX calorimeter, with two tracks pointing to the showers. Bhabha events were used because they were a sample of tracks with a single value of $< dE/dx >$ expected, because they represented an independent, tagged, data sample, and because energetic electrons were the most likely particles to cross over the low $< dE/dx >$ boundary of the upper search region.

Tracks were selected from the Bhabha sample if they had at least 80 good wire clusters and were beam associated in the sense defined earlier. Figure 5.24 shows the $< dE/dx >$ resolution function for these tracks (total sample size=7000 tracks). without the wire restrictions outlined above. Note the long tail extending out to 22 keV/cm. The superimposed curve is the result of

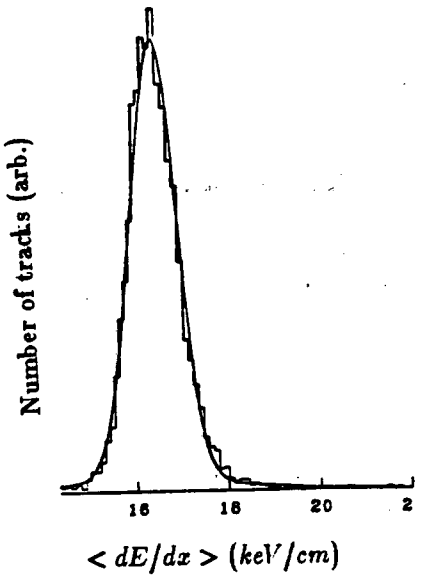

Figure 5.24: $< dE/dx >$ distribution found for wide angle Bhabha electrons with no wire restrictions applied. The curve is the result of a maximum likelihood fit to the function 5.9.

a maximum likelihood fit of the two Gaussian function:

$$P(x) = N_o \left\{ \frac{f}{\sigma_1} exp - \left(\frac{(x-\mu)}{2\sigma_1^2} \right) + \frac{(1-f)}{\sigma_2} exp - \left(\frac{(x-\mu)}{2\sigma_2^2} \right) \right\} \tag{5.9}$$

The second Gaussian is a measure of how long the extra tail is in the $< dE/dx >$ resolution function. For the Bhabha sample without the wire restrictions the maximum likelihood fit gives the following for the parameters in (5.9):

$$\mu = 16.42 \pm 0.006$$

$$\sigma_1 = 0.499 \pm 0.006$$

$$\sigma_2 = 1.9 \pm 0.1$$

$$f = 0.91 \pm 0.01$$

The wire cuts described above were then applied. These significantly reduced the long tail of the resolution function. Figure 5.25 shows this distribution; a comparison to figure 5.24 indeed makes this clear. The best fit parameters for the $< dE/dx >$ distribution for Bhabha's with the wire cuts applied gives:

$$\mu = 16.42 \pm 0.01$$

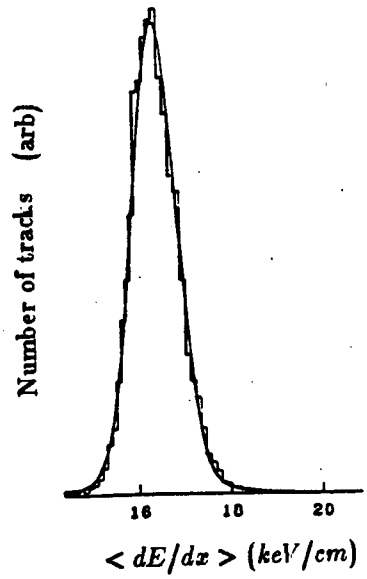

Figure 5.25: $< dE/dx >$ distribution for wide angle Bhabha electrons with the wire restrictions applied, note the reduction of the long tail.

$$\sigma_1 = 0.473 \pm 0.006$$

$$\sigma_2 = 1.3 \pm 0.1$$

$$f = 0.93 \pm 0.01$$

The width of the long range tail is reduced by ~ 30 % by these cuts. Using the approximation for the integral

$$N = \int_{y_0}^{\infty} e^{-x^2}\, dx \tag{5.10}$$

described earlier, one can show that one expects ≈ 20 electrons above the boundary for the $Q = \frac{4}{3}e$ search region before the δ ray cuts, and ~ 1 after these cuts. The elimination of 40 tracks with these cuts is certainly consistent with this if one considers that some of these 40 came from overlapping track pairs. 18 tracks not eliminated by the pad restrictions were eliminated by the wire cuts. A background estimate was also made by fitting the two Gaussian function to the $< dE/dx >$ distribution of pions at minimum ionization. Applying this fit to the electron sample, one expects ~ 1 electron crossing over the boundary of the upper region.

After applying all of the above cuts in conjunction, one candidate track remained in the $Q = \frac{4}{3}e$ region and no candidate tracks remained in the $Q = \frac{2}{3}, \frac{1}{3}e$ search region.

To summarize the restrictions, a track is rejected if it has

1. 3 or more close pad hits not associated with a known track within 3 cm in η and z
2. 4 or more close pad hits not associated with a known track within 3 cm in z.
3. A log-likelihood, L, less than -3.45.
4. 20 or more wide wire z clusters
5. 12 or more wide wire z clusters with ionization at least 1.3 times tha average ionization for the track

The efficiency of these cuts taken in conjunction was 80 % (ie. they eliminate 20 %) for normal $Q = 1e$ tracks.

5.5.3. The remaining candidate.

It is of obvious interest to examine the remaining candidate closely. Figure 5.26 shows the reconstructed track as seen looking in the z direction, it is track number 1. The reconstructed momentum was 1.9 GeV/c with $\delta p/p^2 = 4$ %, and a $< dE/dx >= 21.6$ keV/cm. It has a positive charge. Figure 5.27 shows a comparison of ionization vs. wire number and wire width vs. wire number. These plots do not show any appreciable "clumping" of ionization, in fact the distribution is statistically flat. There are no nearby pad hits indicative of a second unreconstructed track, and the log-likelihood, $L = -2.3$, is consistent with the widths of a single track. There is a hit in the IDC associated with the track, so it is probably not from a conversion in the inner field cage.

If this track were an electron, it would have produced a shower in the HEX calorimeter, but the calorimeter data for this track is consistent with non-showering track. The most likely possibility (of course this is a somewhat subjective conclusion) is that it is a deuteron produced from a secondary interaction in the TPC inner field cage. The evidence consistent with it being a deuteron is threefold. First, it is positively charged, second, it has a $< dE/dx >$ and momentum lying on the ionization curve expected for deuterons. The third piece of evidence is that there

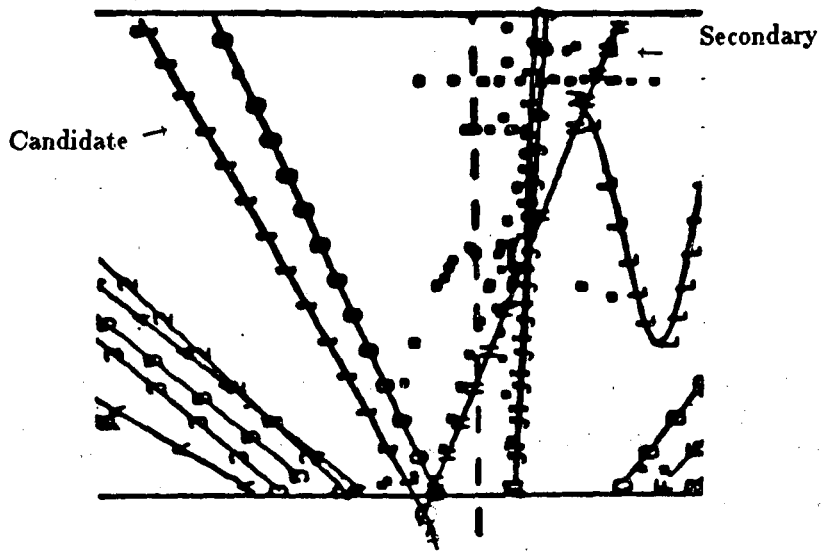

Figure 5.26: Reconstruction of the remaining candidate event. The candidate track is number 1.

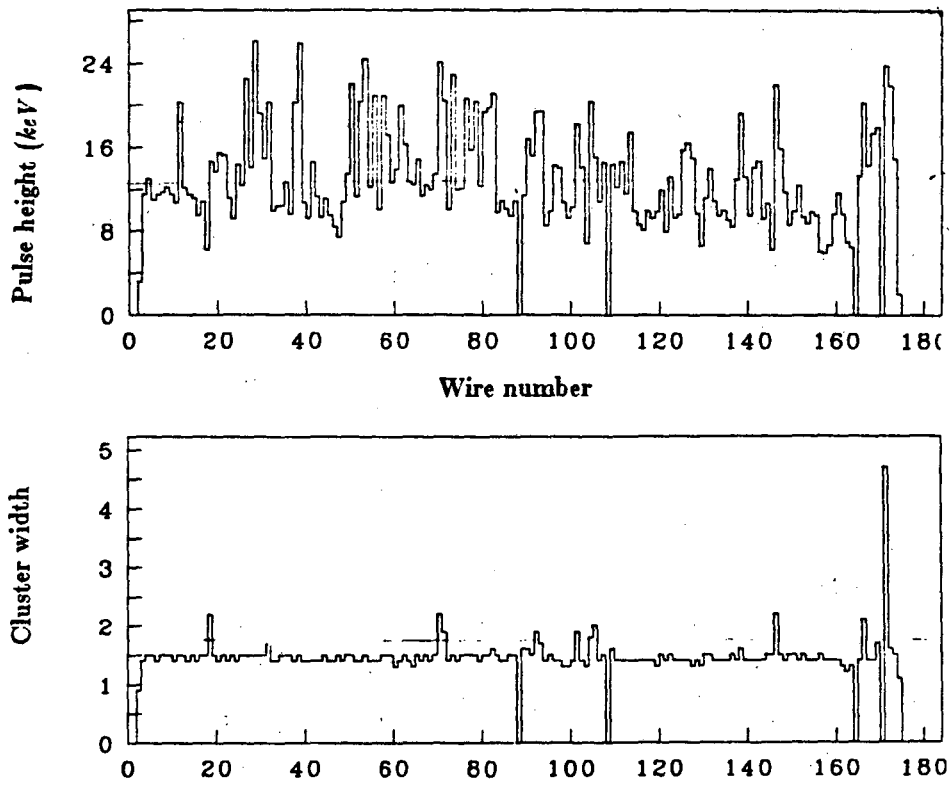

Figure 5.27: Simultaneous plot of ionization and z cluster width vs wire number for the remaining candidate track.

seems to be another track produced in the inner field cage at the same point the candidate track passed through the field cage. This other track is labeled H in figure 5.26, and may indicate that the candidate track was produced in the field cage.

5.6. Background Estimates

There are three potential sources of background in this experiment. It is worthwhile to estimate how much background is expected both before and after applying the restrictions designed to eliminate overlapping track pairs. With one candidate remaining, the 90 % confidence level corresponds to 3.9 events. As will be shown in the following sections, the net background expected from track pair overlap, deuterons and the tails of $Q = 1e$ population is ~ 3 events. From this estimate, we conclude that the remaining candidate is most likely from one of the background sources, and not a fractionally charged particle.

5.6.1. Tails of charge-1e population

The estimate of the background from the $Q = 1e$ population has already been discussed in the previous section, but to summarize, one expects ~ 1 event in the $Q = \frac{4}{3}e$ region from the tails of the electron distribution, and $\sim 1/1000$ events in the upper $Q = \frac{1}{3}, \frac{2}{3}e$ search region, and $1/200$ events in the search region at low $< dE/dx >$.

5.6.2. Deuterons

One of the preliminary cuts on the data sample was designed to reduce the number of deuterons produced in secondary interactions in the detector. This was the cut on the distance of closest approach to the beam-beam crossing. Figure 5.28 illustrates how this works. Consider a primary track interacting in the detector before the TPC active volume. Because of finite production angles, the secondary track when extrapolated will miss the beam-beam crossing point by a substantial amount. Figure 5.29 shows the distribution of the distance of closest approach in r for tracks in the multihadron sample. There is an obvious clustering due to the

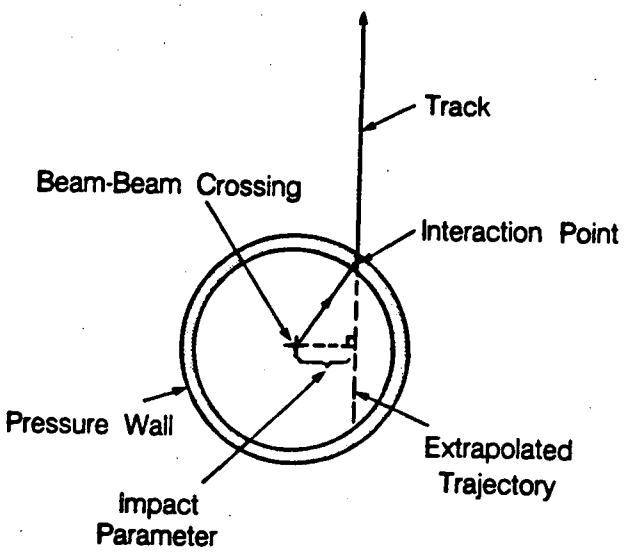

Figure 5.28: Illustration of how secondary interactions in the detector produce tracks with large impact parameters with respect to the beam-beam crossing.

beam associated tracks, and a long tail, due in part to decays in flight, but mostly from secondary interactions in which protons are produced.

One way to estimate the deuteron background is to relax this cut, and see what happens to the sample, keeping all other restriction the same. After removing this cut, there were 15 positively charged tracks passing the rest of the selection criteria, including the cuts against overlapping track pairs. A $< dE/dx >$ vs momentum plot (figure 5.30) for these shows a band falling along the expected ionization curve (solid line) for deuterons. In order to estimate the probability of finding a "forward" scattered deuteron, the distance of closest approach was segmented into bins the same size as the "beam associated" bin; that is, slices in Δr and Δz of 5 and 10 cm. Figure 5.31 shows the population distribution of the 15 tracks in these bins. As one can see, the distribution seems to have some tendency to "peak" in the forward direction, this is not inconsistent with the angular distributions found for deuterons in such processes [54].

In order to estimate the number of deuterons produced in the forward direction, the nearest 3 bins to the beam associated bins were averaged to find $< n >= 2.3$. If we average over all bins in the range where data was found, one finds $< n >= 1$ deuterons expected. If one takes the $\Delta z = 0$ bins, and extrapolates linearly to the central bin, one obtains $< n >= 6$. We conclude

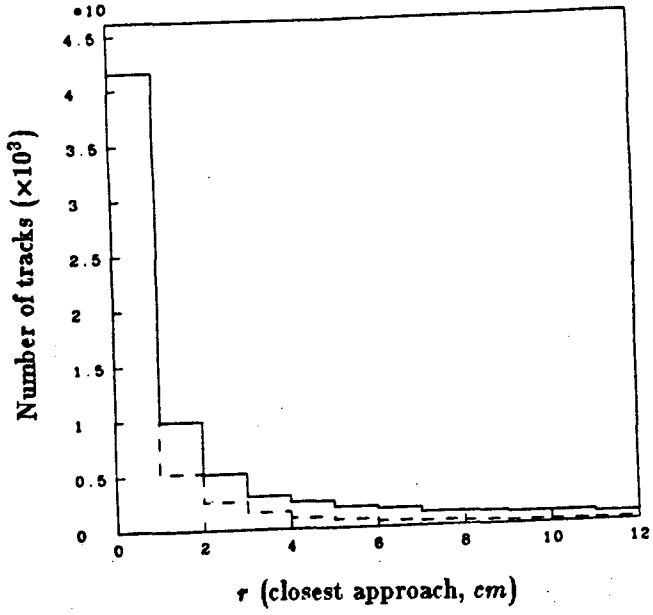

Figure 5.29: Distribution of the distance of closest approach to the beam-beam crossing in r for tracks in the multihadron sample.

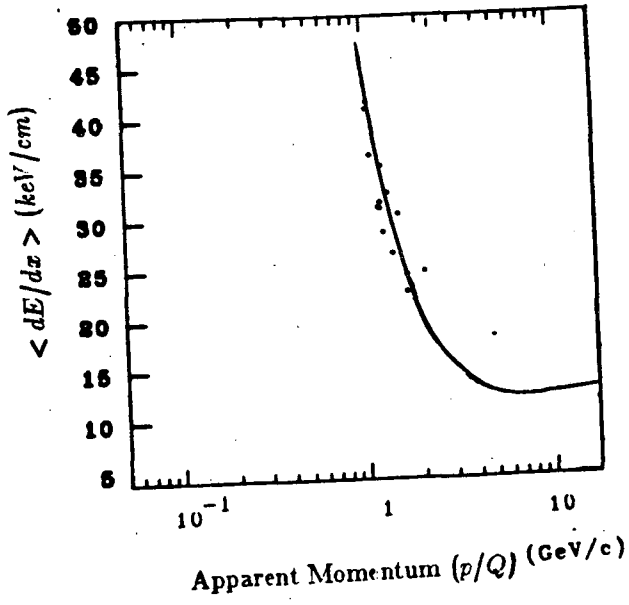

Figure 5.30: $< dE/dx >$ found for tracks passing all cuts, but with the restriction on the impact parameters removed. All tracks have a positive charge, and fall along the line of expected $< dE/dx >$ for deuterons.

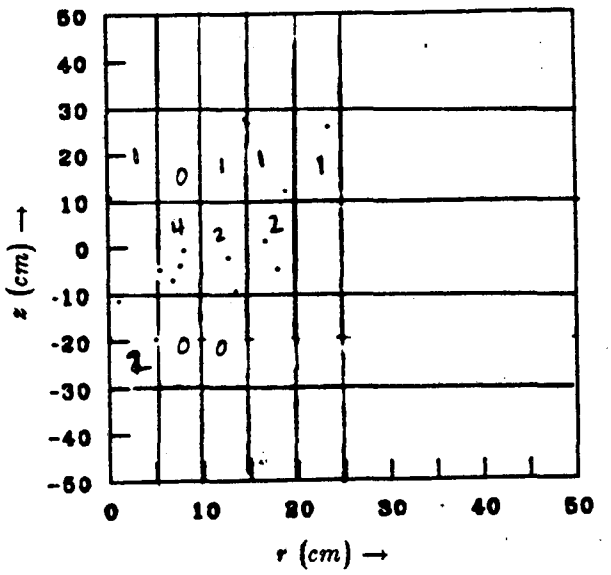

Figure 5.31: Distribution of the distance of closest approach for deuteron candidates from the data sample.

that the one candidate remaining is consistent with the estimate of the background arising from deuteron production. $< n >= 2.3$ will be taken to be the expected background here.

5.6.3. Overlapping track pairs

This background is more difficult to estimate, because the data do not provide a redundant way of testing the background estimates, as was the case above. One must resort to a Monte Carlo simulation to estimate the remaining background from this source. The following approach is used. The detailed detector simulation GLOBAL [37] is used to determine the track pair resolution function for the TPC. Since GLOBAL is very slow (1 hadronic event takes 3 to 5 CPU minutes) it is impractical to use for the generation of a large number of multihadron events. Instead, the resolution function derived by generating track pairs with small angular separations in GLOBAL was used in the fast Monte Carlo, TPCLUND, to simulate the typical separations encountered in multihadron events.

As a cross check the data itself gave some information. If one plots the angular separation of reconstructed track pairs in the TPC, one sees a deficit at $\Delta\theta$ and $\Delta\phi$ approximately equal to 0. By estimating how many tracks are missing in this region, one gets some estimate of the

number of overlapping track pairs in the data, which can be checked against the Monte Carlo predictions.

5.6.3.1. Track pair resolution function

In general, the track pair resolution (or confusion) function is a function of the angular separation in both the polar and azimuthal angles, $\Delta\theta$, and $\Delta\phi$, of the momenta of the tracks, p_1, p_2, and whether they have the same or opposite charges. For completeness, 2 functions will be sought, the first,

$$\mathcal{P}(\Delta\theta,\ \Delta\phi,\ p_1,\ p_2,\ Q_1,\ Q_2)$$

represents the probability of finding a track pair overlapping (ie. reconstructed as one) and in the sensitive region. The second function,

$$\mathcal{P}'(\Delta\theta,\ \Delta\phi,\ p_1,\ p_2,\ Q_1,\ Q_2)$$

is the probability of finding an overlapping track pair reconstructed as a single track, falling in the sensitive region, and passing all of the the two track overlap restrictions.

To estimate these functions, track pairs were generated in GLOBAL. In each run, 2000 pairs of tracks with fixed momenta and charges were generated, populating the $\Delta\theta$, $\Delta\phi$ region uniformly in bins 5×5 *mrad* with 10 pairs generated per bin. Figure 5.32 shows a plot of the typical coverage. The data generated in this way were then run through the TPC track reconstruction programs. The analyzed data were then subjected to the criteria and restrictions described in this chapter. Figure 5.32 shows the distribution of track pairs from such a run which were reconstructed as a single track and found in the sensitive region. Also shown in figure 5.32 is the distribution of track pairs from the same run passing all the restrictions. The obvious effect is that the restrictions do reduce significantly the angular range of the pairs which pass all the restrictions, as one might expect. The distribution is typically a Gaussian for both $\mathcal{P}$ and $\mathcal{P}'$ in $\Delta\theta$ and $\Delta\phi$. Resolutions were typically $\sigma = 12.5\ mrad$ for $\mathcal{P}$ and $\sigma = 4\ mrad$ for $\mathcal{P}'$.

The centroid of the confusion region shifts depending on the charges and momenta of the pairs. This is because for some choices of these parameters $\Delta\phi = 0$ is not the most likely angular

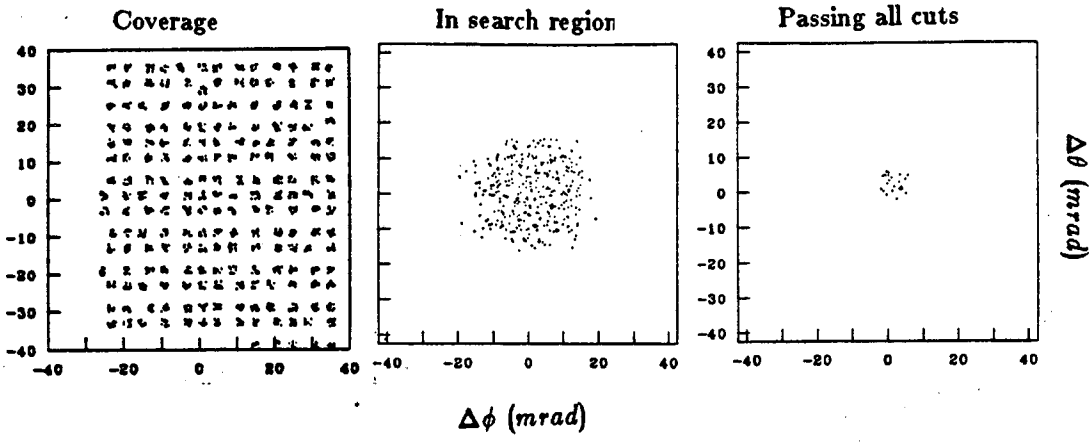

Figure 5.32: Distribution of the angular coverage (in *mrad*), the population in the sensitive region, and the population passing all restrictions of the track pairs generated in GLOBAL and run through the full analysis chain.

separation. As shown in figure 5.6.3.1, for a non-zero $\Delta\phi$, there will be more overlap (ie. more pad clusters merged) than for $\Delta\phi = 0$. By symmetry there should be no shift in the centroid in $\Delta\theta$, and GLOBAL confirms this.

A good parameterization for the centroid, $\Delta\phi_o$ of the distribution in ϕ is given by:

$$\Delta\phi_o \approx 1.0(p_1 - p_2)^2 \qquad mrad \tag{5.11}$$

for like sign track pairs withe p_1 and p_2 measured in GeV/c, and

$$\Delta\phi_o \approx \frac{200}{(p_1 + p_2)} \qquad mrad \tag{5.12}$$

for unlike sign track pairs.

The momenta were divided into 9 bins, 3 in p_1, and 3 in p_2, with the range being $0-2$ GeV/c, $2-5$ GeV/c, and $5-15$ GeV/c. The stability of the results were checked by moving the bin definitions by 1 GeV/c. The probability of a low momentum track pair being found as a candidate is lower than that for a high momentum track pair. The following matrices give the probability for each momentum bin:

$$P_o'(p_1, p_2) \approx \begin{pmatrix} 0 & 0 & 0 \\ 0 & 0.5 & 1.0 \\ 0 & 1.0 & 1.0 \end{pmatrix} \tag{5.13}$$

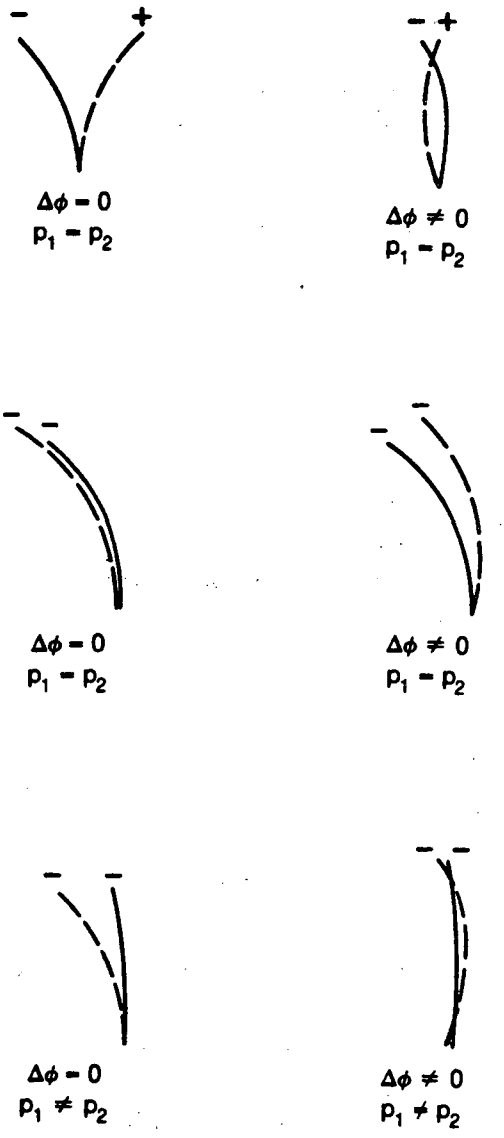

Figure 5.33: Illustration of how the $\Delta\phi$ of maximum track confusion shifts with different charged pairs and with different momenta.

$$\mathcal{P}_o(p_1,p_2) \approx \begin{pmatrix} 0.1 & 0.5 & 0.5 \\ 0.5 & 1.0 & 1.0 \\ 0.5 & 1.0 & 1.0 \end{pmatrix} \tag{5.14}$$

As an example, if a pair of tracks both have momenta between 2 and 5 GeV/c, then if they fall in the $\Delta\theta$ $\Delta\phi$ region of overlap, they have a 50 % chance of being reconstructed as a single track and found in the sensitive region. With these parameterizations defined, the overlap probability function can be approximated as:

$$\mathcal{P} = \mathcal{P}_o exp - \left\{ \frac{(\Delta\phi - \Delta\phi_o)^2}{2\sigma^2} \right\} exp - \left\{ \frac{(\Delta\theta)^2}{2\sigma^2} \right\} \tag{5.15}$$

These overlap probabilities were then fed into the TPCLUND generator. With high statistics, the expected number of overlaps in the sensitive region expected is 150 $\pm$40 track pairs where the error is an estimate of the systematic uncertainty in $\mathcal{P}$. This uncertainty was derived from the agreement between the above parameterizations and the results of the Monte Carlo GLOBAL. The number of overlapping track pairs passing all cuts is estimated to be $0.6\ ^{+3}_{-0.5}$. Again, the errors were estimated from the comparisons of the parameterization with GLOBAL.

As a cross check of this estimate, one can use the data to see whether the estimated deficit at $\Delta\theta$, $\Delta\phi \approx 0$ is consistent with expectations. Figure 5.6.3.1 shows $\Delta\phi$ of track pairs from the multihadron sample, there is clearly a deficit at $\Delta\phi = 0\ \pm 40\ mrad$. The dotted line is the expected distribution from multihadron tracks assuming a detector with infinitely fine resolution. From the difference of these two, one can estimate that $\sim$ 250 overlaps occur. The TPCLUND Monte Carlo predicts that $\approx$ 50 % of these will be found in the sensitive region, giving $\sim$ 125 overlaps in the sensitive region before the criteria used to eliminate overlapping track pairs are applied. This agrees reasonably with what is seen in the data.

5.6.4. Summary of background studies

To summarize the results of the background studies, we expect $\sim$ 3 events in the high $< dE/dx >$ region for $Q = \frac{4}{3}e$ particles, $\sim$ 2 events in the high $< dE/dx >$ region for $Q = \frac{2}{3}, \frac{1}{3}e$ particles, and $\sim$ 1/200 events in the region at low $< dE/dx >$. The presence of one candidate in the $Q = \frac{4}{3}e$ region is consistent with these results. This level of background also implies that

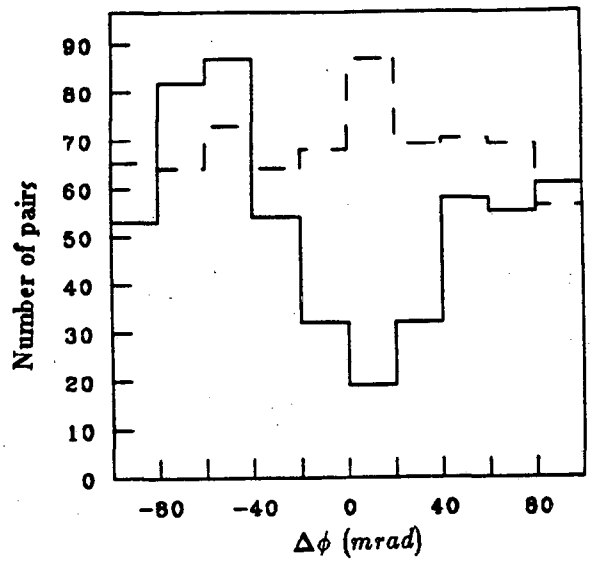

Figure 5.34: $\Delta\phi$ distribution ($mrad$) for tracks in the multihadron sample with small $\Delta\theta$ separations. The dashed line is the prediction from the TPCLUND generator without any track pair confusion. The difference between the two is due to track pair confusion in the data.

in the absence of any improvements (eg. higher magnetic field to separate overlapping track pairs), it would not be worthwhile to extend the measurement in the high $< dE/dx >$ region by increasing the statistics, but it would be reasonable to do so in the region at low $< dE/dx >$.

Chapter 6.

Results and Conclusions

To summarize the results of the previous chapter, in the search regions for $Q = \frac{2}{3}, \frac{1}{3}e$, there are no tracks passing all the selection criteria, and in the search region for $Q = \frac{4}{3}e$ particles, one track has passed all the criteria, but this is consistent with a background deuteron. With this result it is possible to set upper limits on the inclusive production of these particles.

Knowing the detection efficiency, ϵ, the integrated luminosity, $\int \mathcal{L}\, dt$, and the cross section, σ, for some process, then the expected yield of events , n_{ev}, for this process is given by:

$$n_{ev} = \epsilon \int \mathcal{L}\, dt\sigma \tag{6.1}$$

With no events seen above the expected background , it is possible to set an upper limit on n_{ev} at some confidence level. One can then translate this into an upper limit on σ. Upper limits corresponding to the 90 % confidence level will be quoted here. Assuming n_{ev} to be a Poisson distributed variable, the 90 % confidence level corresponds to $n_{ev} = 2.3$ in the case of no events seen, and $n_{ev} = 3.9$ in the case of one event seen (and consistent with background). To illustrate the meaning of the 90 % confidence level in the case of one event seen, if there is a Poisson distribution with a mean of $n_{ev} = 3.9$, then there is only a 10 % chance of observing one or zero events.

It should be noted that even though one is requiring a single fractionally charged particle in the final state (*ie.* $e^+e^- \rightarrow QX$), limits will be quoted on the reaction $e^+e^- \rightarrow Q\overline{Q}X$, where $Q\overline{Q}$ are a pair of fractionally charged particles with opposite signs of charge. There are two reasons for quoting limits on the reaction $e^+e^- \rightarrow Q\overline{Q}X$, rather than on $e^+e^- \rightarrow QX$. The

first is charge conservation. If a fractionally charged particle is produced , somewhere else a fractionally charged particle must exist to compensate the net charge. The second reason is to allow direct comparison to the results of other searches; other experiments quote limits in terms of the reaction $e^+e^- \rightarrow Q\overline{Q}X$ [4], [6],[5]. Also to allow comparison to other experiments, rather than quoting a limit on $\sigma(e^+e^- \rightarrow Q\overline{Q}X)$, a limit on the ratio of σ to the dimuon production cross section, $\sigma(e^+e^- \rightarrow \mu^+\mu^-)$ will be quoted. Here, R_{incl} is defined to be:

$$R_{incl} \equiv \frac{\sigma(e^+e^- \rightarrow Q\overline{Q}X)}{\sigma(e^+e^- \rightarrow \mu^+\mu^-)} \tag{6.2}$$

Quoting an upper limit on R_{incl} has the advantage that the $1/q^2$ dependence of the point-like cross section is factored out, allowing one to make a comparison between experiments carried out at different center of mass energies.

An upper limit on R_{incl} is derived from the expression:

$$R_{incl} = \frac{n_{ev}}{\epsilon \int \mathcal{L}\, dt\, \sigma(e^+e^- \rightarrow \mu^+\mu^-)} \tag{6.3}$$

All the quantities on the right hand side of (7.3) are known except for the efficiency, which can be estimated (see below). The integrated luminosity is known with reasonable accuracy ($77 \pm 6\ nb^{-1}$). The value of n_{ev} is chosen to correspond to the 90 % confidence level upper limit on R_{incl}. At the PEP center of mass energy, 29 GeV, the dimuon cross section is , to first order in QED, $4\pi\alpha^2/3\sqrt{q^2} = .103\ nb$.

6.1. Efficiency Calculation

Any model dependence in the limits on R_{incl} enters through ϵ. First, one must know how the fractionally charged particles should be distributed along the $< dE/dx >$ curves. This is because the search regions in $< dE/dx >$ and apparent momentum do not cover the entire range of $< dE/dx >$ for these particles. For example, the search has little efficiency for $Q = \frac{1}{3}e$ particles at minimum ionization. ϵ will also be a function of the details of the detector, and on how the selection criteria were defined. In general it is impossible to find an analytic expression

for ϵ because of the complexity of the detector, however, ϵ can be calculated with the use of a computer simulation.

The population density along the $< dE/dx >$ curves will be a function of the expected momentum distribution, dN/dp, of these particles. Since we do not know dN/dp *a priori* , one must either take an educated guess for its form, or try quite different forms to display the model dependence of the results. Accordingly, two distributions with substantially different momentum spectra were chosen as inputs:

$$I : \qquad \frac{dN}{dp} \propto \frac{p^2}{E} \tag{6.4}$$

and

$$II : \qquad \frac{dN}{dp} \propto \frac{p^2}{E} e^{-3.5E} \tag{6.5}$$

where E is measured in GeV. The first distribution above, representing a constant matrix element and phase space, is similar to the momentum spectra seen for heavy hadrons, such as D and B mesons produced in e^+e^- annihilation, whereas the second distribution , representing the so called thermodynamic model , is similar to the momentum spectra seen for light hadrons, like pions or protons.

As seen in chapter 2, there are reasonable grounds to expect that if free quarks *are* seen, they will have a large mass $\geq 1\ GeV/c^2$. On the basis of kinematics arguments [56], [57], and simply from comparison to the behavior of heavy hadrons, there are good grounds to take distribution I as representative for free quarks or diquarks with masses greater than $2\ GeV/c^2$. Distribution II was chosen as an alternative model, not only because it occurs in nature, but also because it has a substantially different spectrum than I, with a large population at low momenta.

Multihadron events generated by the LUND [12] Monte Carlo were used as a starting point for the efficiency calculation. The LUND generator reproduces well the gross features of multihadron events at PEP energies, including event multiplicities, momentum spectra, jet opening angles, *etc.* [37]. Two oppositely charged pions from these events were chosen at random, and replaced by a pair of free quarks or diquarks with opposite charges. The fractionally charged particles were given momenta chosen from one of the two distributions above. Because the total

energy in the event is not conserved by such a procedure, the overall energy of the remaining particles in the event is scaled to produce an energy of 29 GeV for the entire event. It should be noted that many other searches find the detection efficiency for the process $e^+e^- \rightarrow Q\overline{Q}X$ by calculating the detection efficiency for the process: $e^+e^- \rightarrow QX$, and multiplying this efficiency by 2. In the limit of very low efficiency, this is justified, but in general, for detectors with high solid angle acceptance like the TPC, this approximation is inaccurate.

The events generated in the above procedure are then used as input to a detector simulation, TPCLUND [55]. The TPCLUND simulation is detailed enough to reproduce faithfully most of the features of the TPC data, but does not take up a lot of computer time, making it practical for the calculation of detection efficiencies. In particular, charge dependent effects, such as energy loss, apparent momentum, multiple scattering and bremsstrahlung are included in the detector simulation. The simulation takes particle four vectors, masses, and charges as input, and returns tracking fits to the momentum and $< dE/dx >$, including the effects of finite detector resolution. In addition to these, track variables, such as momentum errors, the number of wires and pads found on a track, and the distance of closest approach to the beam-beam crossing point were returned. The distributions of these quantities are shown in chapter 5, along with the same distributions from the multihadron data.

The resulting events from TPCLUND were first subjected to the multihadron selection criteria (efficiency $\approx 80\,\%$). In the events satisfying these criteria, all tracks were subjected to the preliminary cuts described in chapter 5. These cuts included the number of wires on a track, the momentum error for tracks in the search region at high $< dE/dx >$, the sector boundary restriction, and the restriction on the distance of closest approach to the beam-beam crossing point. One feature TPCLUND could not replicate, because of the limitations of available computer time, was the detailed behavior of the pad and wire clusters, such as widths, and the presence of nearby hits. Since this information was used to eliminate overlapping track pairs in the search region at high $< dE/dx >$, it was necessary to simulate the inefficiency ($\sim 20\,\%$) these criteria introduced. To do this, an *ad hoc* inefficiency 20 % was introduced for all candidate tracks in the search region at high $< dE/dx >$. The results, however, do not strongly depend on this

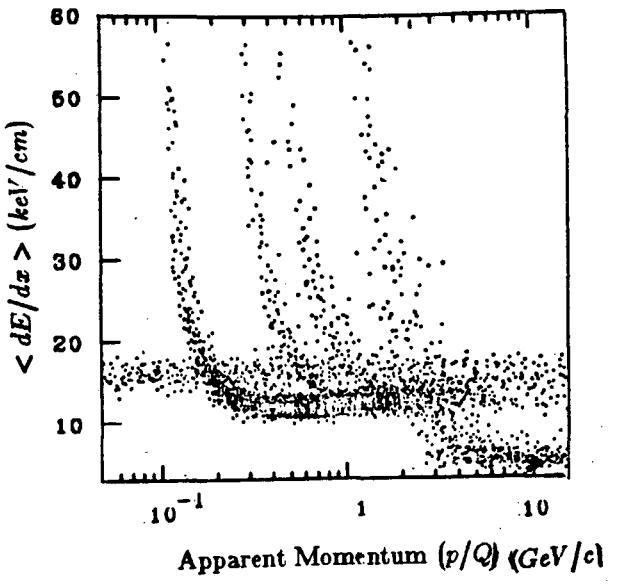

Figure 6.1: Scatter plot of $< dE/dx >$ vs apparent momentum of TPCLUND generated multihadron events containing free $Q = \frac{2}{3}e$ particles with a mass of 3 GeV/c^2. The band resulting from the $Q = \frac{2}{3}e$ particles is clearly visible.

inefficiency .

The tracks satisfying all of these criteria, and found in the search regions detailed in the previous chapter were then scanned to see if they were the free quarks and diquarks initially produced. If at least one candidate track was found in an event, the event was counted. Figure 7.1 shows a scatter plot of $< dE/dx >$ versus apparent momentum for the generated multihadron events with $Q = \frac{2}{3}e$ particles introduced in the above manner. The band of these particles is clearly visible.

It should be noted that in the event simulation, the fractionally charged particles were assumed to have nuclear cross sections no larger than typical hadronic cross sections. Some models, DeRújula, Giles and Jaffe's [16] in particular, estimate that free colored objects could have larger nuclear cross sections than hadrons. From DGJ's scaling law presented in chapter 2, for example, one finds that a 10 GeV/c^2 free quark will have an interaction cross section about 2.5 times that for protons. Since there is about 6 % of a nuclear interaction length for protons between the beam-beam crossing and the TPC active volume, one expects from this scaling that $\sim$ 20 % of 10 GeV/c^2 quarks will not reach the TPC.

Mass (GeV/c^2)	Efficiency %	
	I	II
1	-	15.2
2	-	25.3
3	-	31.4
5	3.0	27.3
8	8.2	16.3
10	20.2	13.8
12	57.0	10.7
13	27.1	7.3

Table 6.1: Table of efficiencies for $Q = \frac{1}{3}e$ particles. The efficiencies quoted are for the momentum spectra I: $dN/dp \propto p^2/E$, and II: $dN/dp \propto (p^2/E)exp-(3.5E)$, with E measured in GeV. When the efficiency was found below 3 %, these were not reported.

The detection efficiency was taken from the ratio of the number of events with a fractionally charged particle detected to the total number of events produced. That is,

$$\epsilon \equiv \frac{Number\ of\ events\ with\ a\ free\ quark\ or\ diquark\ detected}{Number\ of\ events\ with\ a\ pair\ of\ free\ quarks\ or\ diquarks\ produced} \tag{6.6}$$

The highest efficiency found was $\sim$ 70 %, for light, high momentum charge-$\frac{2}{3}e$ particles.

Tables 7.1, 7.1, and 7.1 show the calculated efficiencies as a function of mass and choice of dN/dp for $Q = \frac{1}{3}e$, $\frac{2}{3}e$, and $\frac{4}{3}e$ particles respectively. From these efficiencies, it is possible to draw the 90 % confidence level upper limits on R_{incl} from equation (7.3). These are shown in figures 7.2, 7.3, and 7.4 for $Q = \frac{1}{3}e, \frac{2}{3}e$, and $\frac{4}{3}e$ particles, along with the results from other e^+e^- searches by the Mark II [4], the PEP-14 [5], and the JADE [6] , [7] collaborations. For the momentum hypothesis II for $Q = \frac{4}{3}e$ particles, it is seen that the efficiency is quite low. This is because for such a "soft" distribution, the ionization for these particles is so high as to saturate the electronics, and not appear in the search regions in $< dE/dx >$ and apparent momentum. The localized regions of low efficiency seen on the $Q = \frac{2}{3}e$ limit curves are due to the splitting of the effective search region in $< dE/dx >$ and apparent momentum into two pieces because of the charge-1e background. For these momentum spectra, there are free quark (or diquark) masses for which the majority of the population will fall between these regions, and low efficiency is found.

Mass (GeV/c^2)	Efficiency %	
	I	II
1	71.4	27.8
2	71.4	9.7
3	71.1	11.0
4	70.9	13.7
5	70.2	14.3
6	65.8	13.2
7	57.4	12.8
8	42.9	10.1
9	18.9	9.5
10	9.8	8.3
11	9.8	7.2
12	17.1	6.4
13	29.5	3.4

Table 6.2: Table of efficiencies for $Q = \frac{2}{3}e$ particles. The efficiencies are reported for the two momentum distributions I and II are described in the text.

Mass (GeV/c^2)	Efficiency %	
	I	II
0.5	56.0	-
1	55.9	-
2	55.2	7.2
3	54.6	4.1
4	53.5	-
5	51.5	-
6	50.8	-
7	46.9	-
8	41.5	-
9	32.9	-
10	16.5	-
10.5	5.4	-

Table 6.3: Table of efficiencies for $Q = \frac{4}{3}e$ particles. The efficiencies are reported for momentum distributions I and II described in the text. If the efficiency was found to be less than 3 %, the result was not reported.

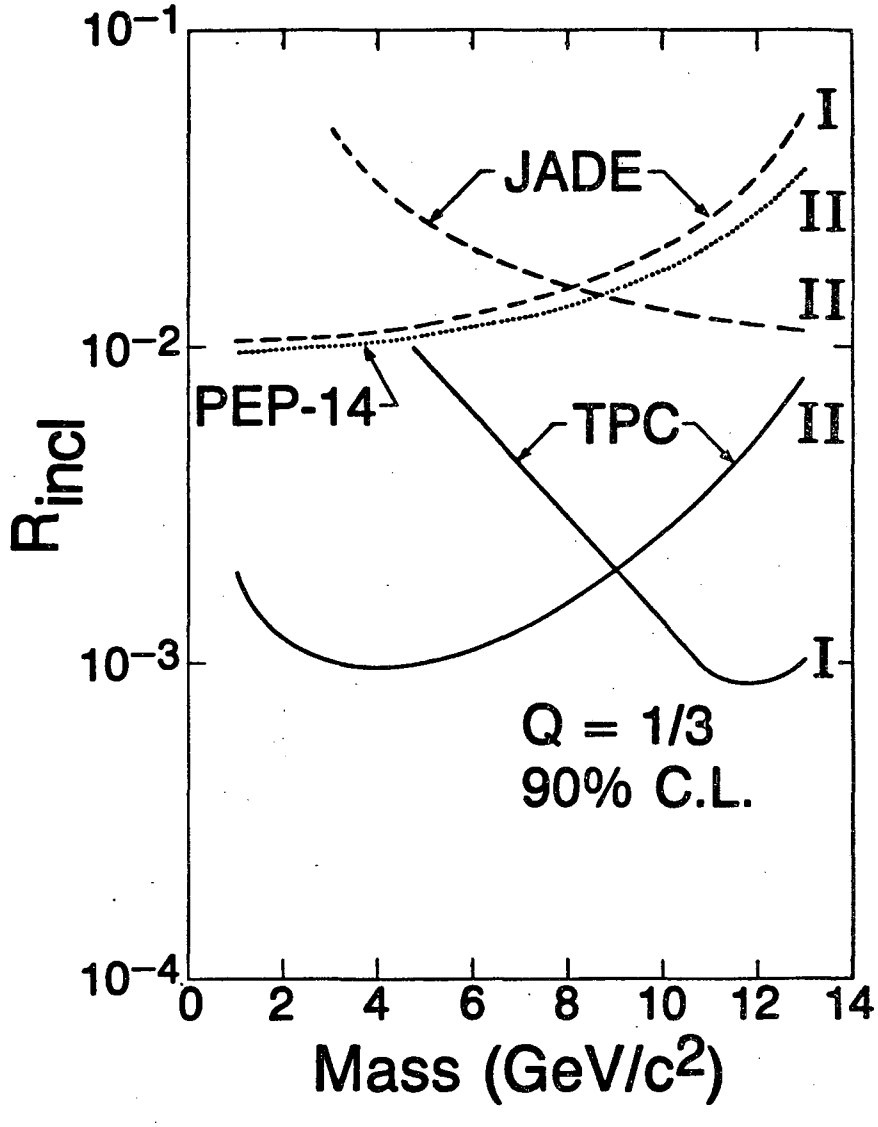

Figure 6.2: 90 % confidence level upper limits on R_{incl} for the production of $Q = \frac{1}{3}e$ particles. The roman numerals refer to the momentum distributions defined in the text. Also shown are upper limits reported by the PEP-14 [5] and JADE [6] collaborations.

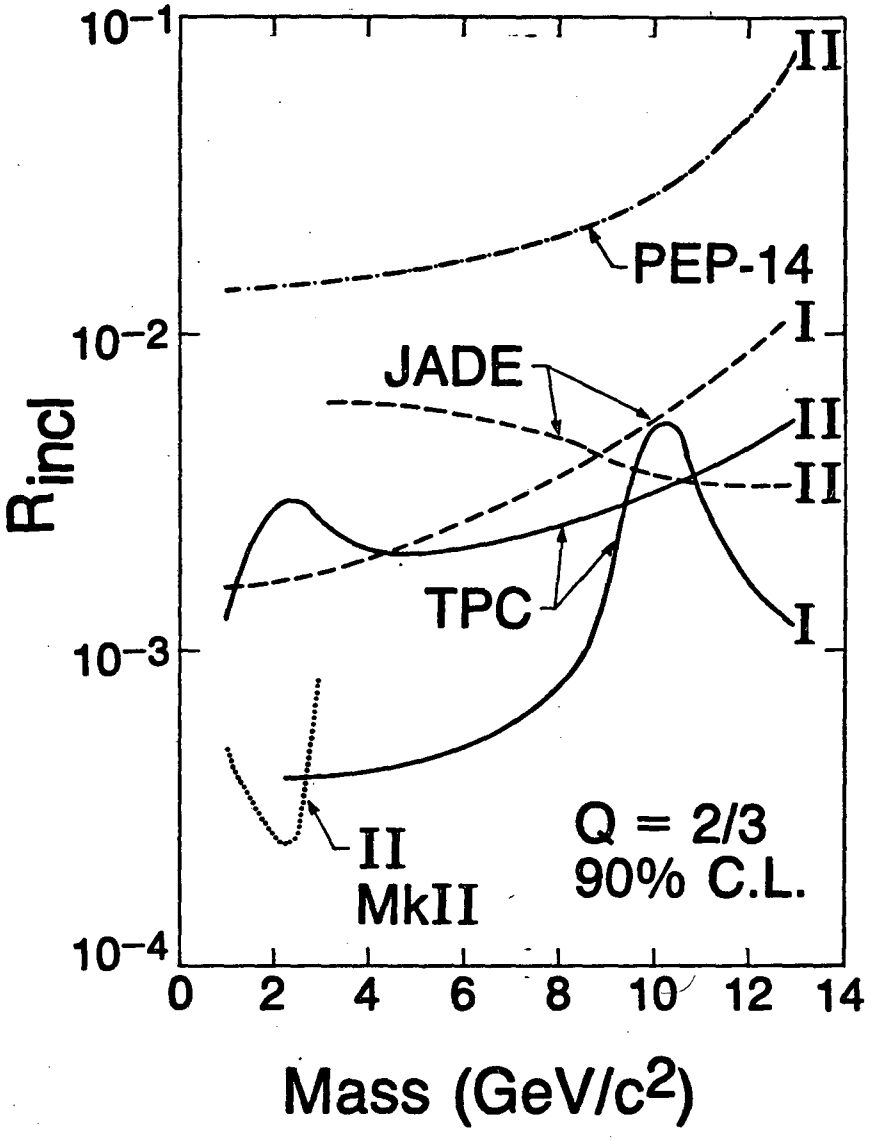

Figure 6.3: 90 % confidence level upper limits on R_{incl} for the production of $Q = \frac{2}{3}e$ particles. The roman numerals refer to the momentum distributions defined in the text. The detailed structure seen is the result of inefficiencies created where the $< dE/dx >$ curves for $Q = \frac{2}{3}e$ particles cross the charge-1e population. Also shown are upper limits reported by the Mark II (for $Q = -\frac{2}{3}e$ only) [4], the PEP-14 [5], and the JADE [7] collaborations.

These limits represent a substantial improvement over the previous searches over much of the mass range for which the experiment was sensitive. Except for distribution II for $Q = \frac{4}{3}e$ particles, these limits are well below 10^{-2} for R_{incl}, over almost the entire mass range. In most cases the limits are at or below the 10^{-3} level.

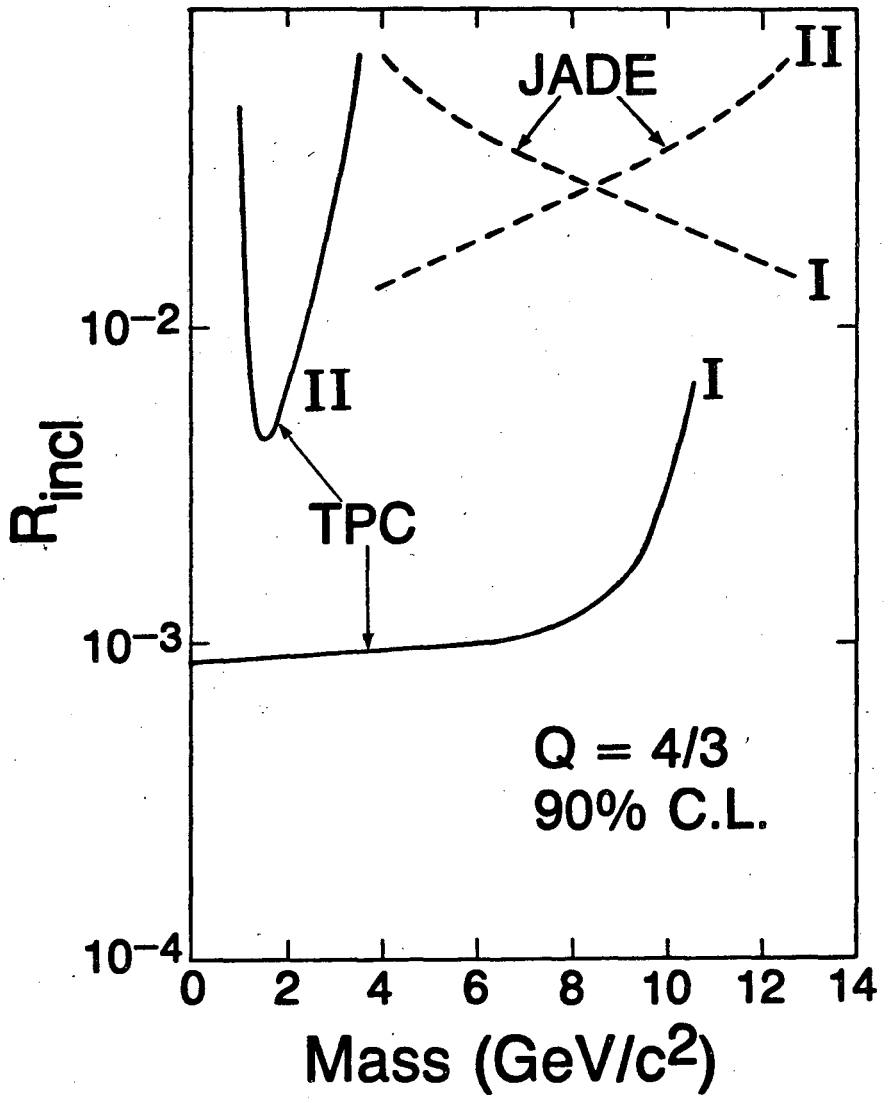

Figure 6.4: 90 % confidence level upper limits on the production of $Q = \frac{4}{3}e$ particles. The roman numerals refer to momentum distributions defined in the text. Also shown are the upper limits reported by the JADE collaboration [6].

Appendix A.

Errors in apparent momentum

Candidate particles in the search region at high $< dE/dx >$ and apparent momentum were required to have momentum errors, $\delta p/p$ less than or equal to 0.1 p (c/GeV). One possible concern is that the momentum errors reported for fractionally charged particles might be substantially different than those reported for charge-1e particles. Although the detector simulation TPCLUND doesn't show any strong bias in the reported momentum errors as a function of charge, it is worthwhile to verify this result. Here it will be shown that as long as all tracks are assumed to have $Q = 1e$, and apparent momentum is used, then the reported momentum errors will be the same for charge-1e and fractionally charged species.

For now, assume we have a detector which can always make a correct charge assignment. The momentum assigned to a track is found from its curvature, C, in a magnetic field, as:

$$p = \frac{\kappa Q}{C} \tag{A.1}$$

where

Q is the charge of the particle

C is the curvature

κ is a constant which includes the magnetic field and dip angle effects (here we will keep the dip angle fixed)

With a 4 kG field, $\kappa \approx 1.2 \times 10^{-3}$ $GeV\ cm^{-1}\ e^{-1}$. For an error in the measured curvature, δC, the resulting error in momentum δp can be found from:

$$\delta p = \delta C \left| \frac{\partial p}{\partial C} \right| \tag{A.2}$$

where

$$\left|\frac{\partial p}{\partial C}\right| = \frac{p^2}{\kappa Q} \tag{A.3}$$

There are two contributions to δC. The first contribution arises because of finite detector resolution, and is, to a good approximation [58]:

$$\delta C_{res} = \frac{\epsilon}{L^2}\sqrt{\frac{720}{N+5}} \equiv a_1 \tag{A.4}$$

where

N are the number of points used in fitting the track (for the TPC, $N \sim 10$)

L is the length of the projection of the track onto the bending plane (for the TPC, $L \sim 80\ cm$)

ϵ is the measurement error for each point (for the TPC, $\epsilon \sim 180\ \mu m$)

The constant a_1 has been introduced for ease of notation; it is important to note that a_1 is purely geometrical and has no dependence on either charge or momentum. Using equation (A.4), for the TPC, one finds $a_1 \approx 2 \times 10^{-5}\ \ cm^{-1}$. The second contribution to δC results from multiple scattering, which dominates at low momenta. Multiple scattering gives rise to a curvature error as [58]:

$$\delta C_{MS} \approx \frac{0.02\,(GeV)\,Q}{L p \beta}\sqrt{\frac{L}{L_R}} \equiv \frac{a_2 Q}{p\beta} \tag{A.5}$$

where

L_R is the radiation length in the scattering medium (for the TPC, $L_R \approx 1114\ cm$)

β is the kinematic variable v/c

The constant a_2 has been defined for ease of notation, and has no charge or momentum dependence. For the TPC, $a_2 \approx 6.7 \times 10^{-5}\ \ GeV\ cm^{-1}e^{-1}$.

Since the curvature errors from both sources should be independent, we can add these in quadrature to find the net curvature error:

$$\delta C = \sqrt{(\delta C_{res})^2 + (\delta C_{MS})^2} \tag{A.6}$$

or

$$\delta C = \sqrt{(a_1)^2 + \left(\frac{a_2 Q}{p\beta}\right)^2} \tag{A.7}$$

We can now find the momentum error from (A.2) , (A.3), and (A.7) as:

$$\frac{\delta p}{p} = \frac{1}{\kappa}\sqrt{\left(\frac{a_1 p}{Q}\right)^2 + \left(\frac{a_2}{\beta}\right)^2} \tag{A.8}$$

The above expression is correct if we have a detector which "knows" what the charge of each particle is. In reality, of course, our detector measures the *apparent* momentum (or rigidity), $p' \equiv p/Q$. By substituting the apparent momentum, the error, $\delta p'/p'$ becomes:

$$\frac{\delta p'}{p'} = \frac{1}{\kappa}\sqrt{(a_1 p')^2 + \left(\frac{a_2}{\beta}\right)^2} \tag{A.9}$$

This is the quantity reported by the track reconstruction programs. In the limit that $\beta \approx 1$, the (apparent) momentum error has no charge dependence and will be the same for charge-1e and fractionally charged species.

This behavior can be understood qualitatively as follows. Consider first the resolution dominated region. The smaller the charge on a particle, the less curvature it shows in a magnetic field, and hence the momentum assignment becomes poorer. When apparent momentum rather than momentum is measured, however, the reconstruction program assumes that the track has a momentum much larger than it really possesses, and reports an error consistent with a high momentum track. These two effects cancel, resulting in a reported momentum error which is independent of charge. In the multiple scattering dominated region, as the charge decreases, so does the net scatter of points about its trajectory. This is offset, however, by the the smaller curvature (or sagitta).

As a check of this, the TPCLUND simulation was used to test the charge dependence of the reported momentum errors. The charge dependence of multiple scattering and track curvature were included in the simulation. These effects only entered into the simulation of the trajectories in the detector. The part of the simulation which reconstructed momentum, assigned errors, *etc.* was blind to the charge of the particle, and assumed it was 1e. The results of this simulation confirmed the above conclusions. This can be seen in plots of $\delta p'/p'^2$ as a function of p' for

particles with different charges, as in figure A.1. At high momentum $\delta p'/p'^2$ is a constant and shows no signifigant charge dependence. In these plots, there is some difference in the low momentum dependence of $\delta p'/p'^2$ as a function of charge. This arises through the $1/\beta$ dependence of the curvature error: at a given value of p', the corresponding values of β will differ for particles with the same mass but different charge. This effect is only important at low momentum, where there is a cut-off in the search region, and will not affect the acceptance much.

With the constants a_1, a_2, and κ defined above, equation (A.9) gives in the limit that $\beta \approx 1$:

$$\frac{\delta p'}{p'} \approx \sqrt{(0.06)^2 + (0.02\,p')^2} \qquad (A.10)$$

where p is measured in GeV/c. In reality, the measured momentum errors are (*cf* chapter 3):

$$\frac{\delta p'}{p'} \approx \sqrt{(0.06)^2 + (0.037\,p')^2} \qquad (A.11)$$

The difference between these two expressions arises largely because distortions reduce the effective path length over which reliable fits can be made.

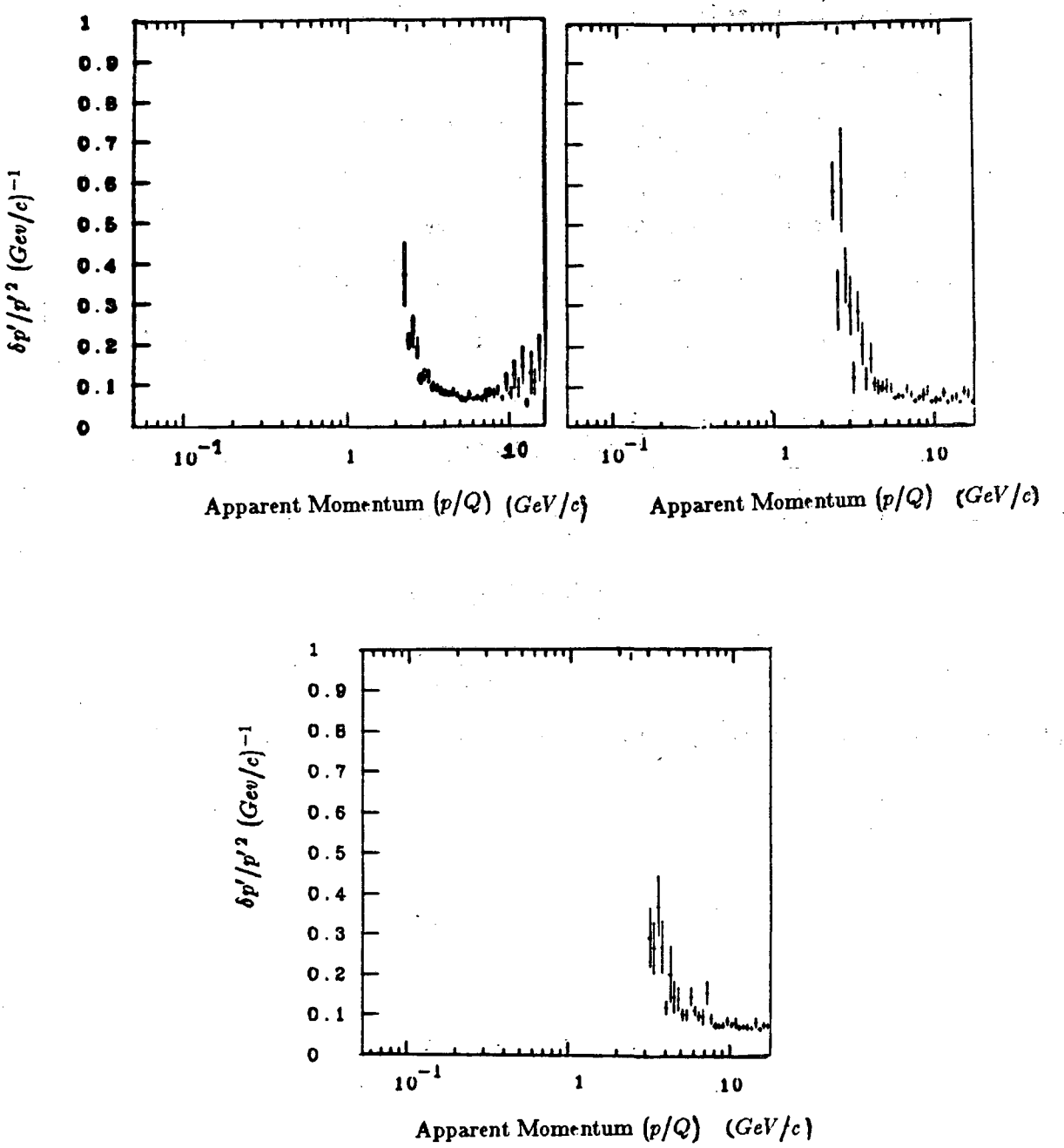

Figure A.1: Plots of assigned momentum errors, $\delta p'/p'^2$ as a function of momentum for fractionally charged particles ($Q = \frac{1}{3}e, \frac{2}{3}$, and $\frac{4}{3}e$). All have a mass of 5 GeV/c^2. Note that the errors are approximately independent of charge, except at low velocities.

Appendix B.

Variations in the Boundaries of the Search Regions

Without a source of fractionally charged particles to calibrate the detector $< dE/dx >$ response as a function of charge, one might worry that there are unknown systematic effects which could reduce the detection efficiency. Possible effects may enter through the scaling of $< dE/dx >$ and $< dE/dx >$ resolution with charge. As seen in chapter 4, there is ~ 2 % deviation from the idealized Q^2 dependence of $< dE/dx >$ on charge because of the effect of the changing shape of the Landau distribution with charge. Because the number of primary electrons produced by $Q = \frac{1}{3}e$, and $\frac{2}{3}e$ particles is smaller than for $Q = 1e$ particles, one expects the $< dE/dx >$ resolution for these particles to drop to $\sim 4\%$ in the search region at low $< dE/dx >$. In both of these cases, we have made assumptions about the behavior of fractionally charged particles in the simulation, but what if these extrapolations are incorrect? As a figure of merit, the residual uncertainties in how these quantities will scale with charge is $\sim 2 - 3$ %.

One way of testing how critically the results depend on these assumptions is to vary the boundaries of the search regions, and see how the efficiencies change. If the boundaries can be varied by 10 % or more without a radical loss of efficiency, then the limits presented will not strongly depend on small deviations from the assumed scaling. Small deviations from the assumed scaling will affect the derived efficiencies the most for relativistic particles. This is because the $< dE/dx >$ for these particles is changing very slowly with momentum, and thus a shift in the $< dE/dx >$ scaling (or in the boundaries) might put a substantial population of these particles on the other side of a boundary. In particular, this applies to both $Q = \frac{2}{3}e$ and

$\frac{4}{3}e$ particles with stiff momentum distributions.

In the search region at low $< dE/dx >$, the lower boundary was shifted from 4 keV/cm to $5keV/cm$. Using the momentum distribution I,

$$\frac{dN}{dp} = \frac{p^2}{E} \tag{B.1}$$

the efficiency for finding $Q = \frac{2}{3}e$ tracks dropped by 2 %. If the upper boundary of this search region is changed from 8 keV/cm to 7 keV/cm, the efficiency drops by 3 %. In the case of $Q = \frac{2}{3}e$ particles produced with the thermodynamic momentum distribution,

$$\frac{dN}{dp} = \frac{p^2}{E}e^{-3.5E} \tag{B.2}$$

(E measured in GeV) the efficiency remains the same to within 1 %. In the search region at high $< dE/dx >$, the lower boundary was shifted from 1.2 to 1.4 times the $< dE/dx >$ expected for electrons. The result of this shift is to reduce the efficiency for $Q = \frac{4}{3}e$ particles by ~ 10 %. A large drop (~ 50 %) in the efficiency for $Q = \frac{4}{3}e$ particles, however, will occur if the boundary is moved to $1.5 \times < dE/dx >_e$. This is because the value of minimum ionization for $Q = \frac{4}{3}e$ particles lies between 1.4 and $1.5 \times < dE/dx >_e$.

As can be seen small variations of the boundaries near minimum ionization for $Q = \frac{2}{3}e$ and $\frac{4}{3}e$ particles will not radically reduce the detection efficiencies.

REFERENCES

[1] L. W. Jones, Rev. Mod. Phys., **49** , 717 (1980).

[2] G. Susinno, in *Proceedings of the International Conference on Physics in Collision: High-Energy ee/ep/pp Interactions, Blackburg, Virginia, 1981* , Vol. I, edited by W. P. Trower and G. P. Bellini, New York, Plenum Press (1982) p. 33.

[3] M. Banner *et al.* (UA2 Collaboration), Phys. Lett., **121B** , 187 (1983).

[4] J. M Weiss, *et al.* (Mark II Collaboration), Phys. Lett., **101B** , 439 (1981).

[5] M. C. Ross, *et al.* (PEP-14 Collaboration), Phys. Lett., **118B** , 199 (1982).

[6] W. Bartel, *et al.* (JADE Collaboration), Z. Physik, **C6** , 295 (1980).

[7] J. Bürger, in *Proceedings of the International Symposium on Lepton and Photon Interactions, Bonn, 1981* , edited by W. Pfeil (Physikalisches Institut, Universität Bonn, Bonn, 1981), p. 115.

[8] J. J. de Swart, Phys. Rev. Lett., **18** , 618 (1967).

[9] R. Slansky, T. Goldman, and G. L. Shaw, Phys. Rev. Lett., **47** , 887 (1981).

[10] see, for example, D. B. Lichtenberg, *Unitary Symmetry and Elementary Particles* , 2nd ed., New York, Acad. Press (1978).

[11] A. Chodos, *et al.* , Phys. Rev. D , **9** , 3471 (1974).

[12] B. Andersson and G. Gustafson, Z. Physik, **C3** , 223 (1980).

[13] T. D. Lee, in *A Festschrift for Maurice Goldhaber* , Trans. New York Acad. Sci., Ser. II, **40** , 111 (1980).

[14] J. D. Jackson, *Classical Electrodynamics* , 2nd ed., New York, Wiley (1975).

[15] T. D. Lee, Phys. Rev. D, **19** , 1802 (1979).

[16] A. DeRújula, R. C. Giles, and R. L. Jaffe Phys. Rev. D, **17** , 285 (1978).

[17] H. J. Lipkin, Phys. Lett., **45B** , 267 (1973).

[18] G. Barbielini, *et al.* , Lett. al Nuovo Cim., **6** , 557 (1973).

[19] D. Bjorken, in *Proceedings of the International Conference on High-Energy Physics, Geneva, 1979* , CERN-PUB RD-421 (1979), p. 245.

[20] H. Aihara, *et al.* (PEP-4 Collaboration), IEEE Trans. Nucl. Sci., **NS30** , 153 (1983).

[21] P. Oddone, and J. Sens, TPC-LBL-81-51 (1981).

[22] H. Aihara, *et al.* (PEP-4 Collaboration), IEEE Trans. Nucl. Sci., **NS30** , 153 (1983).

[23] H. Aihara, *et al.* (PEP-4 Collaboration), IEEE Trans. Nucl. Sci., **NS30** , 67 (1983).

[24] J. Marx, and D. Nygren, Physics Today, **31** , No. 10 (1978).

[25] R. Madaras, and P. Oddone, Physics Today, **37** , No. 8 (1984).

[26] J. Marx, in *Proceedings of the Summer Institute on Particle Physics, Stanford, 1980* , edited by A. Mosher, SLAC Report No. 239 (1981), p. 215.

[27] D. Nygren, TPC Report No. TPC-LBL-81-41, 1981; J. Marx, TPC Report No. TPC-LBL-81-41, 1982; W. Hofmann, presented at TPC data analysis meeting No. 13 , 1982 (unpublished).

[28] P. Martin, TPC Report No. TPC-LBL-78-50, 1978.

[29] H. Hilke, TPC Report No. TPC-LBL-78-50, 1978.

[30] R. Fuzesy, *et al.* , Nucl. Instr. and Meth., **223** , 40 (1984).

[31] D. A. Landis, *et al.* , IEEE Trans. Nucl. Sci., **NS29** , No. 1 , 573 (1982).

[32] R. C. Jared, *et al.* , IEEE Trans. Nucl. Sci., **NS29** , No. 1, 282 (1982).

[33] H. Aihara, *et al.* , (PEP-4 Collaboration) IEEE Trans. Nucl. Sci., **NS30** , 162 (1983).

[34] B. Gabioud, and R. van Tyen, presented at TPC data analysis meeting No. 20, 1982 (unpublished).

[35] G. Lynch, TPC Report No. TPC-LBL-82-3, 1980.

[36] H. Aihara, *et al.* (PEP-4 Collaboration) , IEEE Trans. Nucl. Sci., **NS30** , 76 (1983).

[37] N. Hadley, Ph.D. thesis, Univ. Calif., Berkeley, 1983.

[38] W. Gorn, and C. Lindsey (private communication).

[39] M. Ronan (private communication).

[40] M. Ronan, *et al.* , IEEE Trans. Nucl. Sci., **NS29** , No. 1, 427 (1982).

[41] C. Buchanan, TPC Report No. TPC-UCLA-83-2 (1983).

[42] M. Garnjost (private communication).

[43] N. Toge and H. Yamamoto, TPC Report No. TPC-UT-84-2 (1984).

[44] E. Fermi, Phys. Rev., **57** , 485 (1940).

[45] D. Ritson, in *Proceedings of the Summer Institute on Particle Physics, Stanford, 1980*, edited by A. Mosher, SLAC Report No. 239 (1981), p. 177.

[46] G. Lynch, TPC Report No. TPC-LBL-81-6, 1981.

[47] W. Allison and J. Cobb, Annu. Rev. Nucl. Sci. , **30** , 253 (1980).

[48] L. Landau, J. Phys. U.S.S.R., **8** , 201 (1944).

[49] A. H. Walenta, *et al.* , Nucl. Instr. and Meth., **161** , 45 (1979).

[50] J. Huth, TPC Report No. TPC-LBL-82-78, 1982.

[51] H. Frehse, *et al.* , Nucl. Instr. and Meth., **156** , 87 (1978).

[52] M. Shapiro, Talk presented at TPC analysis meeting No. 61, 9, Sept. 1983 (unpublished).

[53] N. Hadley, TPC Report No. TPC-LBL-83-20, 1983.

[54] M. E. Law, *et al.* , *A Compilation of Data on Inclusive Reactions* (LBL-80), 1980.

[55] W. Hofmann, TPC Report No. TPC-LBL-83-2, 1983.

[56] M. Suzuki, Phys. Lett., **71B** , 139 (1977).

[57] J. D. Bjorken, Phys. Rev. D, **17** , 171 (1978).

[58] R. Gluckstern, Nucl. Instr. and Meth., **24** , 381 (1963).

This report was done with support from the Department of Energy. Any conclusions or opinions expressed in this report represent solely those of the author(s) and not necessarily those of The Regents of the University of California, the Lawrence Berkeley Laboratory or the Department of Energy.

Reference to a company or product name does not imply approval or recommendation of the product by the University of California or the U.S. Department of Energy to the exclusion of others that may be suitable.

TECHNICAL INFORMATION DEPARTMENT
LAWRENCE BERKELEY LABORATORY
UNIVERSITY OF CALIFORNIA
BERKELEY, CALIFORNIA 94720